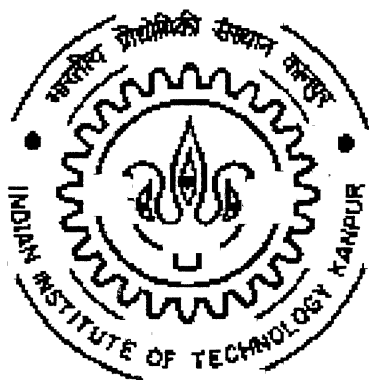# HYDROGEN ATTACK ON CARBON-ALLOYED IRON ALUMINIDE Fe-28Al-2C

by

TAPAS LAHA

DEPARTMENT OF MATERIALS AND METALLURGICAL ENGINEERING

INDIAN INSTITUTE OF TECHNOLOGY, KANPUR INDIA 208016

DECEMBER 2002

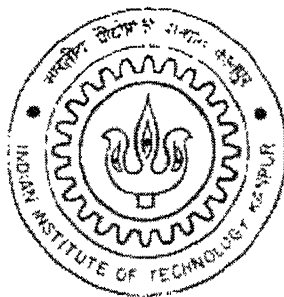# HYDROGEN ATTACK ON CARBON-ALLOYED IRON ALUMINIDE Fe-28Al-2C

A Thesis Submitted

In Partial Fulfillment of the Requirements
For the Degree of

MASTER OF TECHNOLOGY
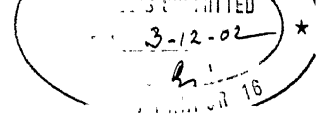
by

TAPAS LAHA
(YO20611)

to the

DEPARTMENT OF MATERIALS AND METALLURGICAL ENGINEERING

INDIAN INSTITUTE OF TECHNOLOGY, KANPUR
INDIA 208016

DECEMBER 2002

CERTIFICATE

This is to certify that the work contained in the thesis entitled "**HYDROGEN ATTACK ON CARBON-ALLOYED IRON ALUMINIDE ALLOY Fe-28Al-2C**" by **Tapas Laha (Roll No. Y020611)** has been carried out under our supervision and to the best of our knowledge this work has not been submitted elsewhere for a degree.

R. Balasubramaniam, Professor

Department of Materials and Metallurgical Engineering

Indian Institute of Technology, Kanpur

India 208016

Date: 02 December 2002
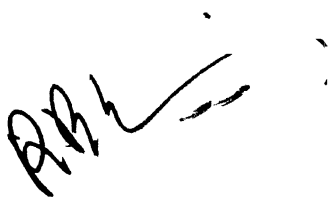
CERTIFICATE

This is to certify that the work contained in the thesis entitled "**HYDROGEN ATTACK ON CARBON-ALLOYED IRON ALUMINIDE Fe-28Al-2C**" by **Tapas Laha (Roll No. Y020611)** has been carried out under our supervision and to the best of our knowledge this work has not been submitted elsewhere for a degree.

R. Balasubramaniam

Professor

Materials and Metallurgical Engineering

Indian Institute of Technology, Kanpur

India 208016

A. Tewari

Assistant Professor

Materials and Metallurgical Engineering

Indian Institute of Technology, Kanpur

India 208016

Date: 02 December 2002

ACKNOWLEDGMENTS

CONTENTS

ABSTRACT

The high temperature hydrogen attack in carbon-alloyed iron aluminide alloy Fe-28.1Al-2.1C (Fe-16.2%Al-0.54%C in wt%) has been addressed. This alloy was obtained from Defence Metallurgical Research Laboratory, Hyderabad. India. The alloy was processed by arc induction melting and eletro-slag remelting.

Hydrogen attack in the carbon-alloyed iron aluminide was studied by exposing well-polished samples to hydrogen gas (1 atmosphere) at different high temperatures for different times (i.e. at 700°C for 10h and 48 h, and at 900°C for 144h, 336h and 720 h). The characteristics of HA were evaluated by two-dimensional microstructural analysis, mechanical testing (microhardness testing) and electrochemical characterization carried out on the rolling plane of the as-received alloy as well as of the hydrogen treated samples.

The alloy exhibited a two-phase structure; recrystallized matrix-grain and precipitated carbide. Two different types of morphology of the carbides were observed in two dimension; circular and needle-shaped. The needle-shaped carbides were having large exploded surface area per unit volume in spite of having a very low volume fraction. The bulky carbides as well as the needle shaped carbides avoid sharing surface with each other. Hydrogen and carbon diffused much more easily through the interfaces between the bulky carbides and matrix during the hydrogen treatment as the edge length between bulky carbides and matrix is approximately two times more than that between three grains of matrix or between needle-shaped carbides and matrix. Moreover, the bulky carbide is 3.5 times more likely to occur on a grain triple point and two times more likely to occur between two grains as compared to inside a grain. This must be related to the sympathetic nucleation of the carbides at heterogeneities and also to the easy diffusion of carbon through grain boundaries, during the formation of these carbides. The composition of the bulky carbides and needle-shaped carbides were approximated as 64.17Fe-19.81Al-18.35C and 62.40Fe-19.87Al-17.73C, respectively from the EMPA results. The stoichiometric formula of the matrix phase and bulky carbide was determined as Fe_3Al and $Fe_{4-y}Al_yC_x$, where y varies from 0.91 to 1.19 and x varies from 0.90 to 1.02. Similarly the formula of the needle-shaped carbides was estimated as $Fe_{4-y}Al_yC_x$, where y varies from 0.99 to 1.12 and x varies from 0.82 to 0.96.

The thermodynamic feasibility of methane formation in Fe-16.2Al-0.54C at 700°C and at 900°C was theoretically justified. The kinetics of hydrogen diffusion into the material was evaluated theoretically to understand the depth of hydrogen attack in the alloy.

Electrochemical polarization studies indicated that the as-received alloy as well as the hydrogen treated samples exhibited active-passive behavior in acidic solution (0.1 N to 1.0 N H_2SO_4). The anodic polarization curves of the alloy exhibited a secondary anodic peak in the range of –45 mV to –92 mV, with respect to Ag-AgCl standard electrode, before reaching the broad passive zone of constant passive current density. As the normality of the H_2SO_4 was increased from 0.1 N to 1.0 N the corrosion rate increased continuously and systematically. The critical current density for the second anodic peak did not display a general trend of increase with increase in normality of H_2SO_4. Whereas, the increasing critical current density for the second anodic peak can be understood by the larger amount of hydrogen available for oxidation in solutions of lower pH. In the passive region, the passive current density was constant in solutions of different normalities, thereby proving the similar nature of the passive film on the surface of the alloy as a function of potential

The hydrogen dissolved during the treatment did not play any role on the secondary anodic peak. The increase in the passivation ranges and passivation current density values of hydrogen treated samples with increasing treatment temperature and time could not be attributed to the surface roughness induced by the high temperature hydrogen treatment. The change in surface property was confirmed by the change in hardness of the carbides and matrix. The decrease in hardness of the matrix could probably be due to the decurburization from matrix. The carbon could have either diffused to the bulky carbide precipitates or reacted with the ambient environment. The lower matrix hardness also indicates compositional changes.

LIST OF FIGURES

LIST OF TABLES

CHAPTER 1

INTRODUCTION

The motif of the present study is to investigate different aspects of high temperature hydrogen attack in carbon alloyed iron aluminides. This chapter introduces the subject of intermetallics, with emphasis on iron aluminides. The technical importance of these materials has motivated investigation into several aspects concerning these materials and towards better understanding of its properties. The chapter concludes with the objective of the present study and the plan of work.

1.1. Intermetallics

There is an increasing interest in the development of materials based on intermetallic phases. Ordered intermetallics constitute an unique class of advanced materials that form long range-ordered crystal structures below a critical temperature termed as the critical ordering temperature (Tc) [1]. They usually exist in relatively narrow compositional ranges around simple stoichiometric ratios (similar to inorganic compounds). The need to develop materials possessing high specific strength, for structural applications, at elevated temperatures has motivated research in the area of ordered intermetallics.

Intermetallic aluminides possess many interesting features that project them as candidate materials for high temperature structural applications [2]. They contain enough aluminum to form, in oxidizing environments, thin films of aluminum oxides that are often compact and protective. They are characterized by low densities, relatively high melting points and good mechanical properties at elevated temperatures. The aluminides that have attracted attention as potential candidates for high temperature applications include titanium, nickel and iron aluminides and hence have undergone extensive development in the recent past, primarily for high temperature applications. Research on these materials are being carried out extensively by effecting modifications on the existing systems (either by alloying or by modifications in the processing steps) in order

to optimize their properties. Iron aluminides, being the theme of the present thesis, would be addressed specifically here.

1.2. Iron Aluminides

Important iron aluminides are ordered intermetallics centered on the compositions Fe_3Al and FeAl. These aluminides possess attractive properties for application at elevated temperatures and severe environments over conventional structural materials like nickel-base superalloys. Specific advantages include excellent sulphidation resistance, oxidation resistance, lower density (5400-6700 kg/m^3) which is 30% of that of commercially available high temperature materials, good wear resistance, cavitation erosion resistance potentially lower cost and reduced consumption of strategic elements such as chromium [3]. One of the key factors in increasing the maximum use temperature is enhanced oxidation resistance. Once the desired crystal structure and subsequent mechanical properties have been achieved, then focus should be on high temperature oxidation and room temperature corrosion resistance. Therefore, understanding the thermodynamics and kinetics of high temperature interactions in these materials is of utmost importance.

1.3. Carbon-Alloyed Iron Aluminides

Though iron aluminides exhibit poor room temperature ductility and low fracture toughness, significant improvement in this respect can be achieved by alloying additions and process control. Most of the available literatures deal with iron aluminide compositions with very low (<0.01 wt %) carbon contents because carbon causes significant reduction in ductility [4]. Baligidad *et al* reported that addition of carbon in the range of 0.14 to 1.1 wt % significantly increase in strengthening due to the precipitation of perovskite based $Fe_3AlC_{0.5}$ phase and the formation of a duplex Fe_3Al-$Fe_{4-y}Al_yC_x$ structure [5-7]. These alloys also exhibited relatively higher room temperature ductility, which was attributed to irreversible trapping of hydrogen at carbide-matrix interface [8]. Moreover, the carbon-alloyed iron aluminides are stronger and this increase in room temperature yield strength and hardness was attributed to solid solution strengthening by the interstitial carbon in the matrix as well as precipitation strengthening due to the presence of perovskite based $Fe_{4-y}Al_yC_x$ precipitates [6,7]. Alloys with high

carbon content (0.074 to 0.27 wt %) exhibit excellent machinibility due to the uniform presence of plate like $Fe_3AlC_{0.5}$ precipitates, which facilitate the formation of small and uniform size chips during machining [6]. Moreover, the Fe-Al (Al>16 wt %) alloys with higher carbon content (~1%) are more resistant to oxidation and decurburization. A better oxidation resistance appears to lead to resistance to decurburization in these alloys [9].

1.4   Objectives

The present study is specifically concerned with the high temperature hydrogen attack of carbon-alloyed iron aluminides. Presence of carbon in the range of 0.14 wt % to 1.1 wt % in iron aluminide alloys increases its strength considerably, the room temperature ductility, machinibility and the resistance to oxidation and decurburization. However, when such type of alloys are used in high temperature applications in hydrogen containing atmospheres, carbon or carbide in the material reacts with diffusing hydrogen forming methane bubbles and this bubbles act as defects in the alloy structure and cause failure at stresses lower than the fracture stress. The following aspects are to be investigated in the present study on hydrogen attack in carbon-alloyed iron aluminides.

1. Understanding microstructural changes in carbon-alloyed iron aluminides due to hydrogen attack.by image analysis and by comparing hardness of carbides and matrix, after and prior to the hydrogen treatment.

2. To evaluate a quick potentiodynamic polarization method to follow dissolved hydrogen in the alloys.

3. Analysis of attack utilizing theories of thermodynamics and characterization.

1.5   Plan of work

The work has been planed to proceed according to the following sequence:

1. Procurement of carbon alloyed iron from Defense Metallurgical Research Laboratory, Hyderabad, India.

2. Preparation of as received samples for stereological characterization and microhardness testing.

3. Design and installation of experimental set-up for treating the samples to hydrogen gas at higher temperature (up to 900 °C).

4. Preparation and exposure of samples for hydrogen treatment.

5. Potentiodynamic behaviour study of the as-received sample in H_2SO_4 solution of different normality and of the hydrogen treated samples at 0.5 N H_2SO_4 solution.

6. Stereological characterization and microhardness testing of the hydrogen-treated samples

7. SEM study of hydrogen treated–samples.

The present research aims to understand some aspects of hydrogen attack in carbon-alloyed iron aluminides. Chapter 2 deals with the review of the literature. Experimental procedures are discussed in Chapter 3. Chapter 4 presents the results and discussion. The conclusion and suggestions for further work are listed in Chapter 5, followed by bibliography.

CHAPTER 2

LITERATURE REVIEW

The phase diagram and structure of iron aluminides would be briefly reviewed in the beginning of the chapter. The room temperature mechanical properties of iron aluminides would be addressed. Hydrogen entry mechanism into metals and materials, different types of hydrogen damage and different aspects of hydrogen attack are discussed. The application of stereology to characterize metals and will also be addressed. Finally, the chapter ends with a brief survey of room temperature aqueous corrosion behavior of iron aluminides.

2.1. Phase diagram and structures

2.1.1. Iron aluminides

Ordered iron aluminides exist in relatively narrow compositional ranges around simple stoichiometric ratios. The phase diagram of Fe-Al system is shown in Figure 2.1. Iron aluminides based on Fe_3Al and FeAl can exist in two crystal allotropic modifications. These structures (DO_3 and B2) are both ordered BCC structures and these are presented in Figure 2.2. Fe_3Al can exist both B2 and DO_3 ordered structure (depending upon the temperature) while FeAl can exist only in the B2 ordered form. Table 2.1 presents some typical room temperature properties and critical ordering temperatures for different allotropic modifications of iron aluminides [3]. The room temperature strength and room temperature ductility of iron aluminides are low (Table 2.1).
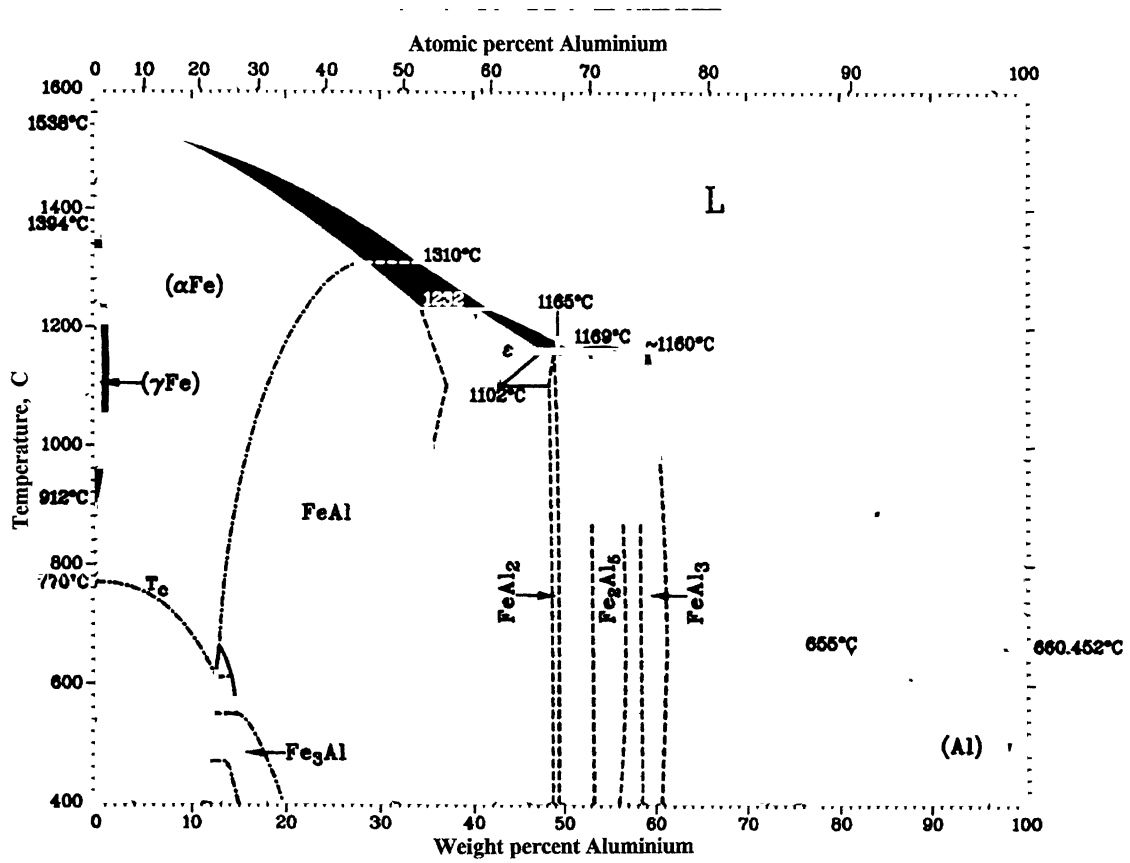
Figure 2.1   The Fe-Al phase diagram
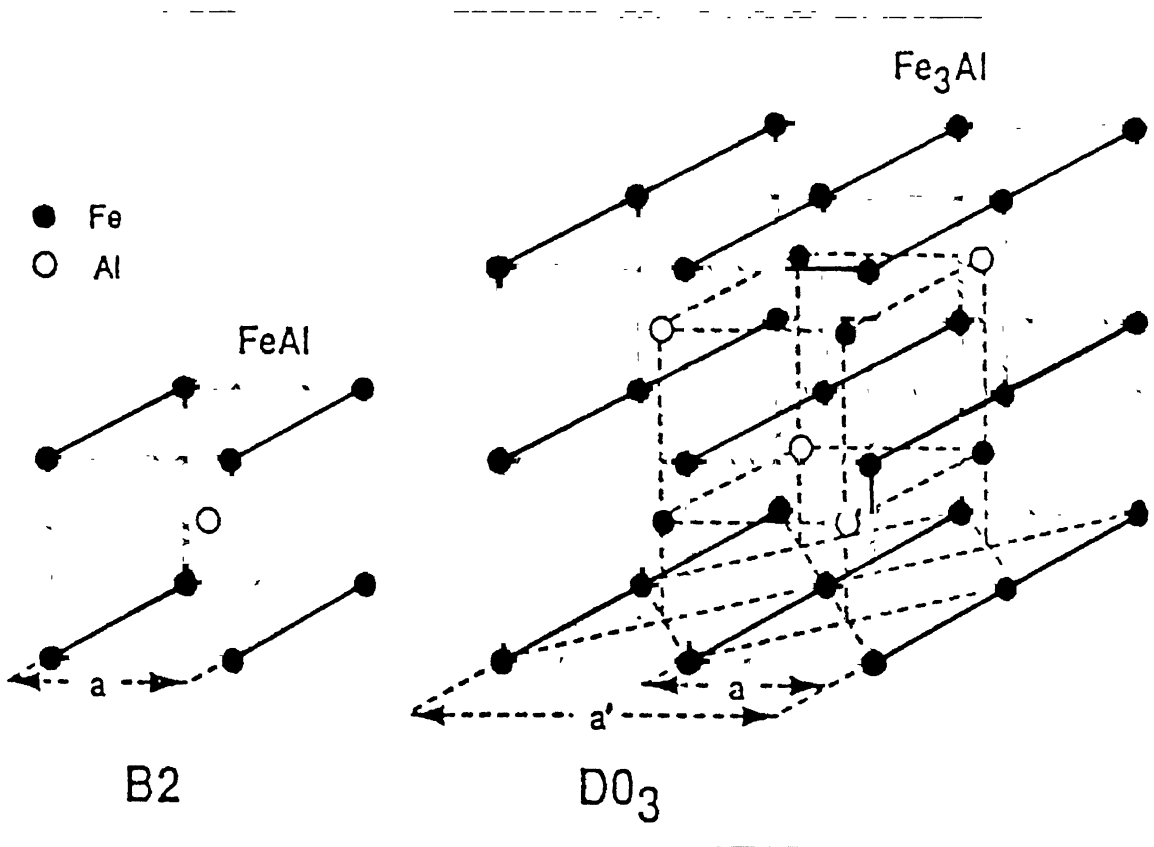
Figure 2.2   The DO3 and B2 ordered crystal structure of iron aluminides

Table 2.1   Typical room temperature properties of iron aluminide [3]

Alloy	Crystal structure	Ordering temp.	Melting point	Density (gm/cc)	Y.S. (Mpa)	Elongation (%)
Fe_3Al	DO_3	540°C	1540°C	6.72	300	3.7
Fe_3Al	B2	760°C	1540°C	6.72	380	4.1
FeAl	B2	1250°C	1250°C	5.56	360	2.2

2.1.2. Phase equilibria in the Fe-Al-C system

The phase equilibria of Fe-Al-C system were determined from electron microprobe analysis (EPMA) of quenched samples. There are four phases of primary crystallization viz. κ, α, γ and graphite [2, 10]. The extent of the field of primary crystallization of κ shown is tentative in Figure 2.3. Figure 2.4 and figure 2.5 shows the Fe-Al-C isotherms at 25°C and 1000 °C respectively. Al increases the temperature of the graphitic eutectic reaction, as Al is a graphitic stabilizer [11]. At low carbon contents the BCC (α) phase exists in the disordered state A2 as well as in the long range ordered states of type B2 and DO_3. At higher carbon contents the FCC (γ) solid solution is stable and a ternary intermetallic phase, denoted by κ-phase, exists which is based on the perovskite structure [2, 10,11].

The κ phase

κ phase can be considered as an ordered FCC arrangement of type Ll_2, with carbon atom in the octahedral interstices rather than regarding it as carbide. A perfect atomic arrangement of this type would be correspond to the formula Fe_3AlC. In fact, the stoichiometry has never been observed. Recently the formula $Fe_{4-y}Al_yC_x$ was suggested for the κ phase by Palm *et.al.*, where x may vary between 0.8 to 1.2 and y between 0.42 and 0.71 [10]. While, Baligidad *et.al.* [50] suggested the formula of the carbide as $Fe_3AlC_{0.5}$. The phase diagram and in particular the existence domain of this phase are not well known. It is difficult to determine the exact composition of κ phase. The solubility of carbon in iron aluminide melts decreases with increasing temperature leading to the

precipitation of primary graphite. At the ideal composition of the κ-phase Fe₃AlC, the precipitation of graphite starts already at 2150°C, while the κ-phase might form at 1400⁰C. Even by rapid quenching it is not possible to avoid graphite precipitation. Therefore, single-phase material of the κ phase can not be obtained directly from the melt. The homogeneity range of κ phase is markedly shifted to higher carbon concentration with decreasing temperature. Upon quenching the alloy may thus hit and penetrate into two-phase field α+κ. Therefore, at compositions where single-phase material of the κ phase would be expected, in fact three phases may be observed, the κ phase plus primary graphite and ferrite [10,11].

The α solid solution

There is a noticeable solubility for carbon in the BCC (α) solid solution of up to 1.5 at wt % carbon. With increasing Al content the transition temperature of A2/B2 transformation increases with respect to the carbon-free crystals from about 40°C at 25 at % Al, to up to 100°C at 35 at % Al. This means that by the introduction of carbon the ordered B2 structure is stabilized with respect to the disordered A2 structure; because the B2 structure offers the favorable surroundings of six iron atoms for carbon [10, 11].

The γ solid solution

The extension of the stability range of the γ phase varies considerably as a function of temperature. With increasing temperature the aluminium content increases from 7.5 at % at 800°C to 24 at % at 1315°C while the solubility for carbon is about constant. During cooling to room temperature the γ phase undergoes a martensitic transformation. The temperature for this transformation is yet to be determined. The hardness of the martensite is considerably higher than that of the κ-phase [10].

Little is known about the Al-C system. The solubility of C in both liquid and solid Al is very limited (0.32 wt.% at 1227°C, decreasing to 0.10 wt.% at 830°C and extrapolating to 0.07 wt.% at 660°C. The only known compound of the system is Al₄C₃ [11,12].
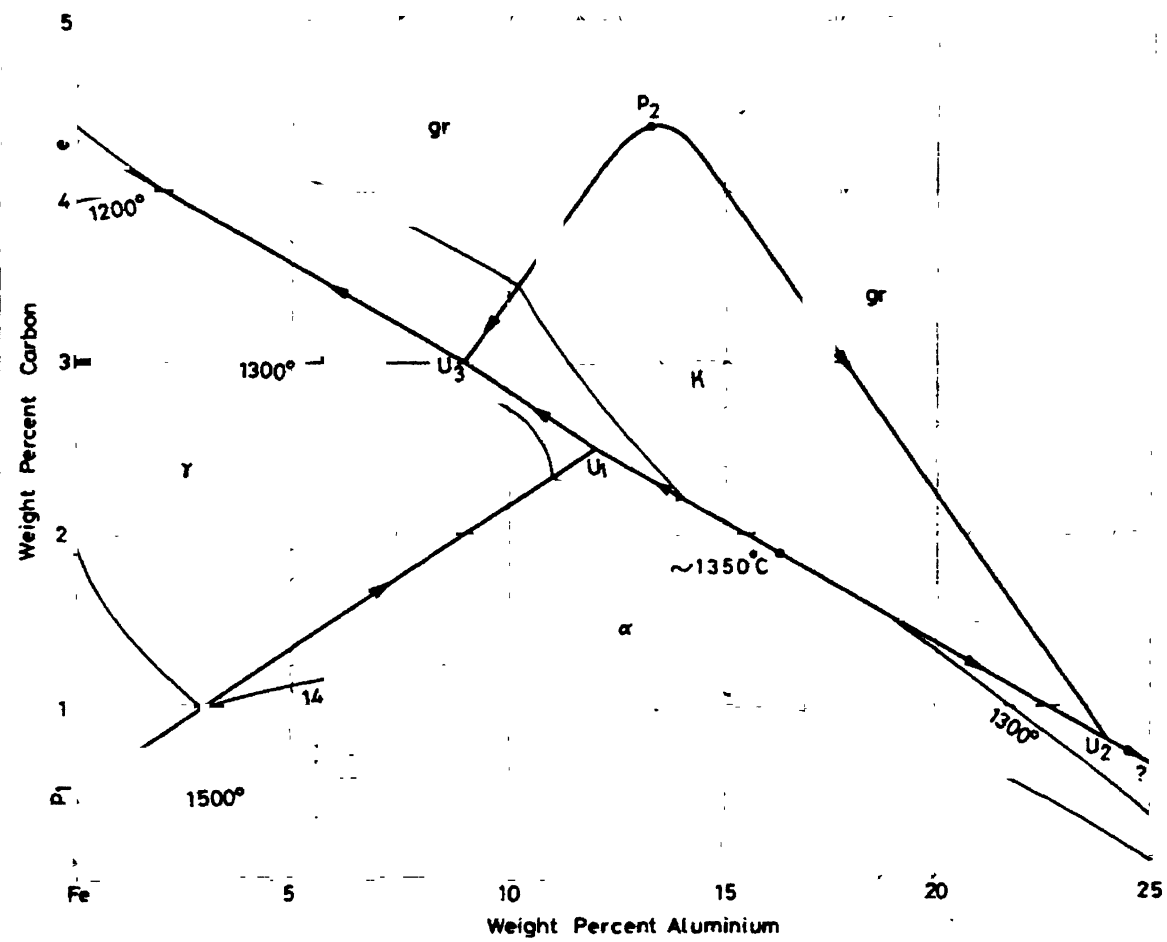
Figure 2.3   Al-C-Fe liquidus in weight percent
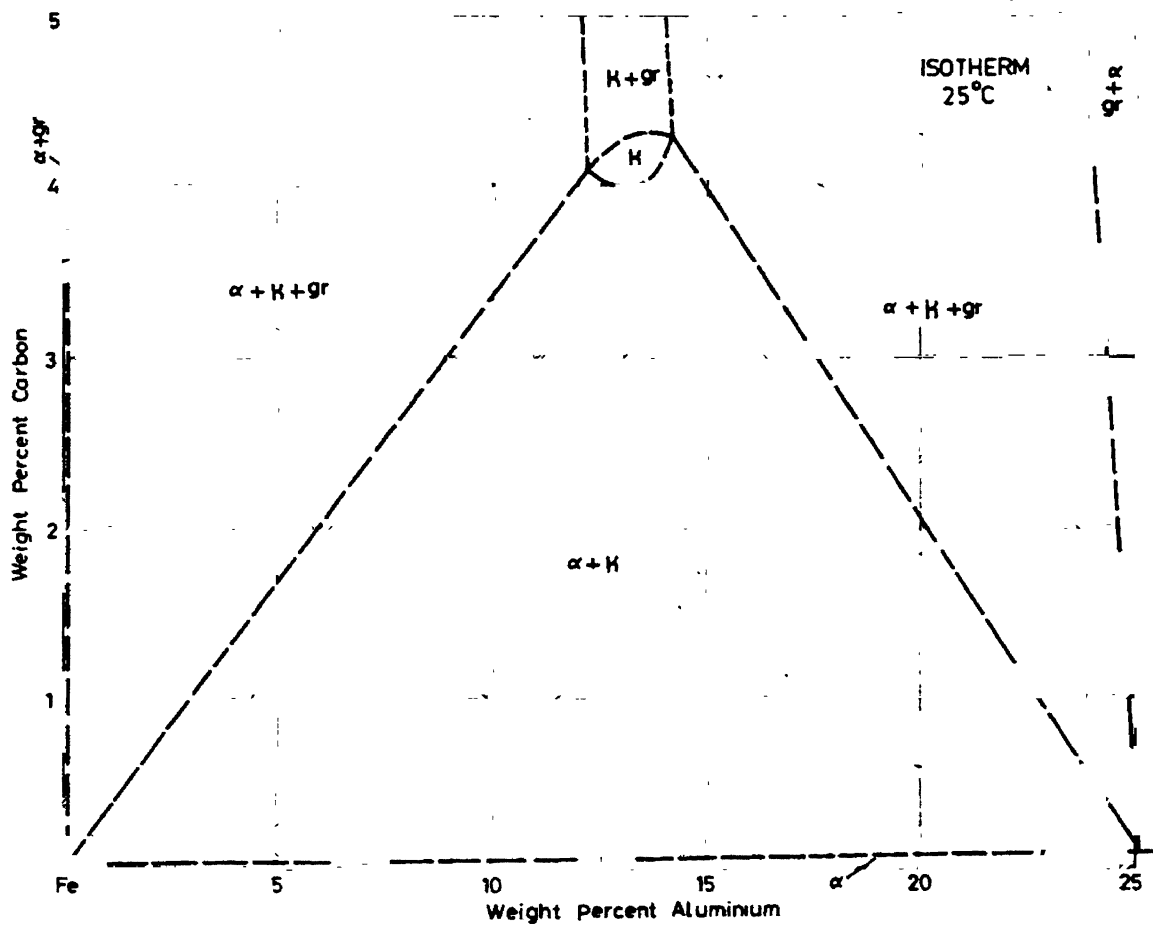
Figure 2.4   Fe-Al-C isotherms at 25°C in weight percent

Figure 2.5   Fe-Al-C isotherms at 1000°C in weight percent

12
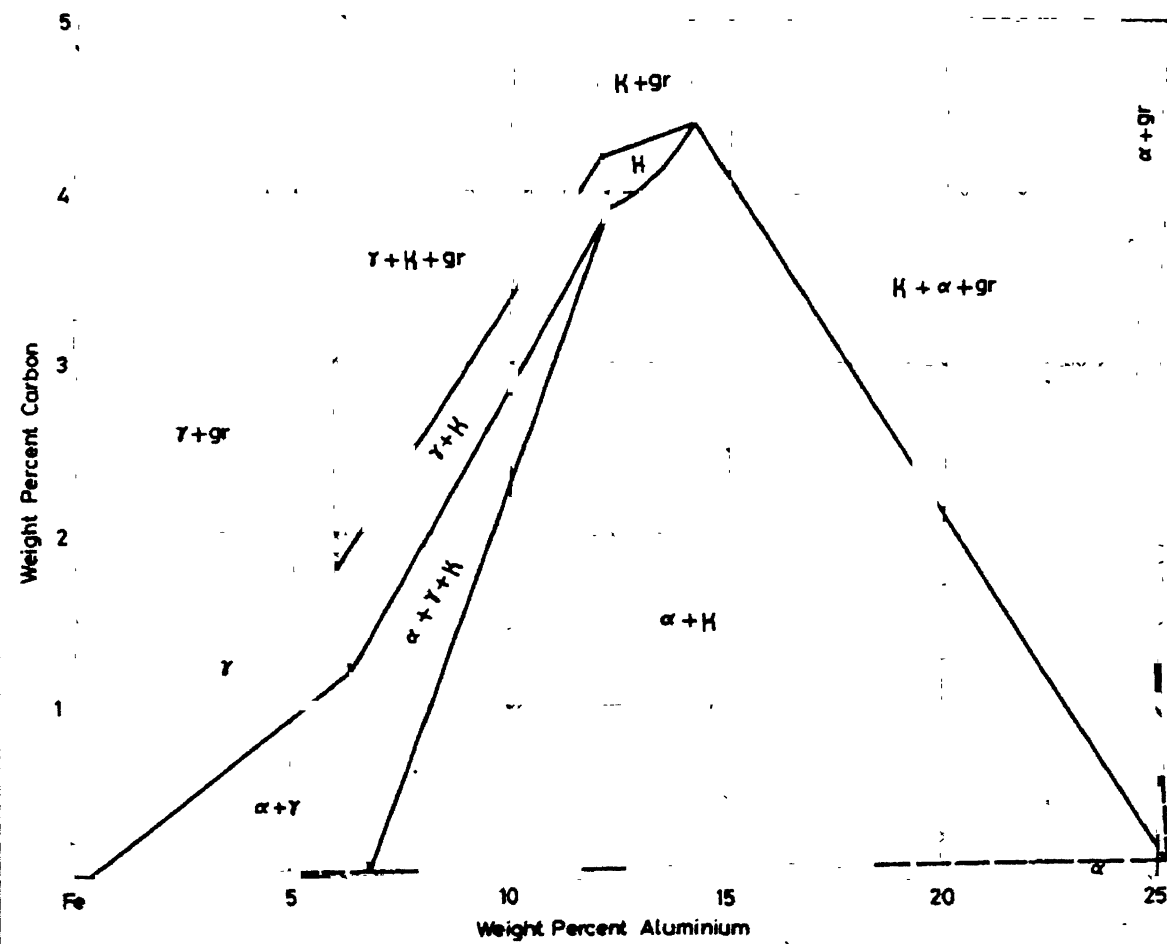
2.2. Room temperature mechanical behavior

Iron aluminides have been known to be brittle at room since the first study was conducted in 1930 [13]. However, the major cause of their low ductility and brittle fracture was not known. Liu *et al* have proposed an environmental effect as the major cause for room temperature embrittlement in iron aluminides [14]. They proposed that the embrittlement involves the reaction of water vapour with aluminium and the reaction product, atomic hydrogen enters the lattice and causes embrittlement.

$$2Al + 3H_2O \rightarrow Al_2O_3 + 6H \qquad\qquad\qquad \text{eqn. 2.1}$$
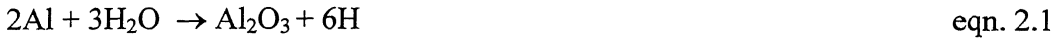
Direct evidence has also been provided recently for the production of hydrogen by reaction of iron aluminide with water vapour by Zhu *et al* [15] by a laser mass spectroscopic technique.

That hydrogen is the main damaging agent causing poor ductility was confirmed from tensile tests conducted in different environments. These results are summarized in Table 2.2. The effect of various test environments on the room temperature stress-strain behavior of iron aluminide is shown schematically in Figure 2.6. As evident from the figure ductility is higher in $Ar + 4\%H_2$ environment rather than humid air. This is because molecular hydrogen does not cause much embrittlement in Fe_3Al, because of its lower activity as compared with atomic hydrogen produced from water vapour reaction. As seen in this figure, testing in water vapour environment show the least ductility and vacuum/oxygen environments provide high ductility. Liu et al have shown that higher ductilities are observed in a dry oxygen environment rather than in vacuum because oxygen reacts with aluminium to form Al_2O_3 directly [14]

$$2Al + 3/2\ O_2 \rightarrow Al_2O_3 \qquad\qquad\qquad \text{eqn. 2.2}$$

thereby suppressing the aluminium-moisture reaction which provides nascent hydrogen. Generation of atomic hydrogen (eqn. 2.1) is suppressed and thus higher ductility is observed in dry oxygen environment.

The crucial factor in improving the room temperature mechanical properties of iron aluminides, i.e. the ductility, is to restrict the entry of hydrogen into the material and to possibly irreversibly trap diffusive hydrogen. The following paragraphs review the methods employed by researchers in achieving this goal.

13

Table 2.2a   Room temperature tensile properties of iron aluminides after heat treatment for 2 hr at $700^{\circ}C$ (B2 structure) [14]

Environment	Y.S. (Mpa)	U.T.S. (Mpa)	Ductility (%)
Vacuum	387	851	12.8
Oxygen	392	867	12.0
Air	387	559	4.1
H_2O vapour	387	475	2.1

Table 2.2b   Room temperature tensile properties of iron aluminides after heat treatment for 120 h at $500^{\circ}C$ (DO_3 structure)

Environment	Y.S. (Mpa)	U.T.S. (Mpa)	Ductility (%)
Vacuum	316	813	12.4
Oxygen	298	888	11.7
Air	279	514	3.7
H_2O vapour	322	439	2.1
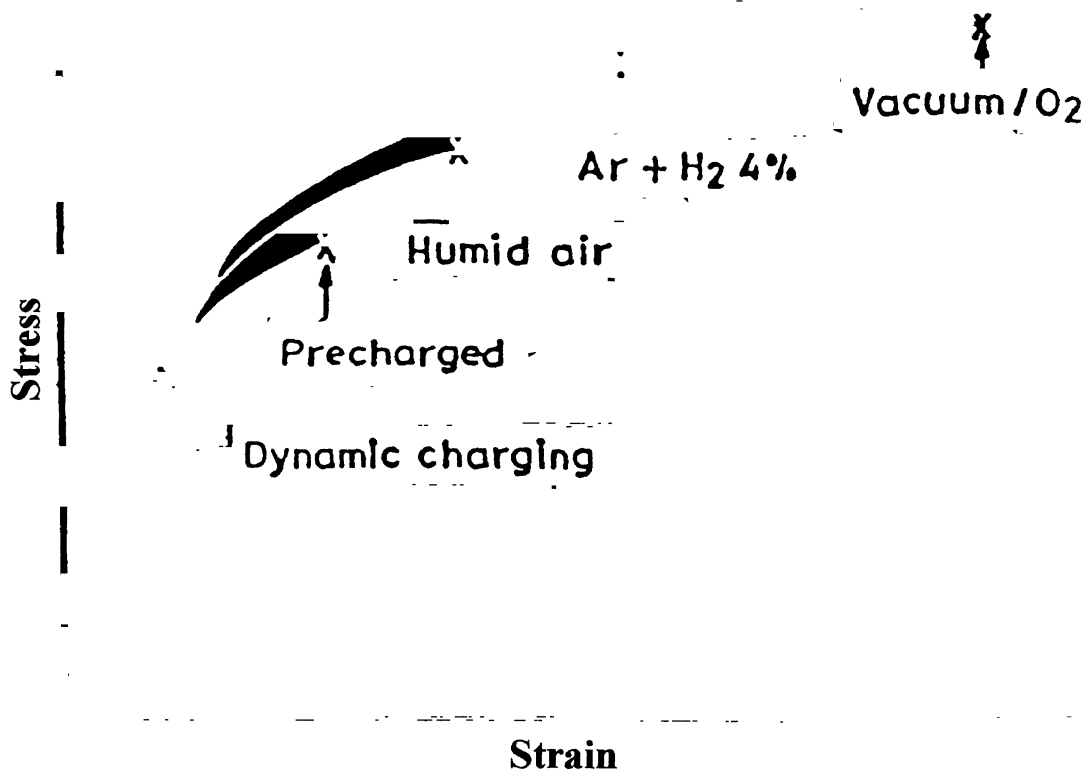
Figure 2.6 Schematic tensile stress-strain behavior of iron aluminides in various environments at ambient temperature

In order to obtain the desired properties of metals, alloying with additional elements is generally attempted. The type alloying addition would depend upon the property that is being addressed. For providing strength, elements that lead to solid solution strengthening or to the precipitation of age hardenable phases are added. This could also be increased by adding elements that refine the grain size and hence provide grain strengthening. In case the corrosion resistance of the metal has to be enhanced, passivity-inducing elements should be added. It should be emphasized that the alloying element that is added should not lead to the deterioration in some property where it is not intended. For example, if an element primarily added to enhance passivity, leads to the precipitation of ternary brittle intermetallics, especially at the grain boundaries, the

property of strength would be very severely affected. therefore, the possible deleterious effects of alloying should also be understood.

2.3. Effect of carbon addition

Most of the reported literature is on iron aluminides containing very low (<0.01 wt %) carbon content, produced using very high purity raw material because carbon was believed to embrittle these alloys [3]. It was recently reported that addition of carbon to the Fe-16 wt % Al alloy results in improved strength, machinibility, resistance to environmental embrittlement and creep resistance [4,5,6]. Carbon additions of 0.03 wt % or more result in precipitation of $Fe_{4-y}Al_yC_x$ phase (where x may vary between 0.8 to 1.2 and y between 0.42 and 0.71 [10]) in these alloys, which imparts significant dispersion strengthening and leads to improved creep resistance. Though $Fe_{4-y}Al_yC_x$ is a hard and brittle phase, its presence in the alloys matrix did not lead to reduction in ductility. This is because $Fe_{4-y}Al_yC_x$ precipitates were supposed to act as hydrogen traps, reducing the susceptibility of the alloy to hydrogen embrittlement [7]. This susceptibility to embrittlement in moist environments is a major cause for poor room temperature ductility and machinibility. Addition of carbon has been reported for alloys with low (16 wt.%) Al-contents. In these alloys the addition of 1 wt.% carbon was found to lead to the best combination of mechanical properties [8].

The addition of carbon (in the range of 0.5 to 1.1 wt %) to the Fe-Al alloy (the range of Al content is 16 to 20 wt %) also allowed the use of low cost processing techniques such as air induction melting (AIM) followed by electroslag remelting (ESR) [5, 7]. Cheap raw material such as steel scrap (which may contain significant amount of carbon) and commercial aluminium were used for melting of these alloys. The AIM and ESR ingots exhibited significant amount of precipitate $Fe_{4-y}Al_yC_x$ (where x may vary between 0.8 to 1.2 and y between 0.42 and 0.71 [10]). These precipitates form a continuous network resulting in a duplex Fe_3Al - $Fe_{4-y}Al_yC_x$ structure (Figure 2.7) [5]. Tensile testing was carried out for Fe-8.5AL-C alloys (where the range of carbon varied from .04 to 1.1 wt %) by Baligidad *et al.* According to them the alloys showed cleavage mode fracture at room temperature. The fracture changed to mixed (cleavage + dimple) mode at 400°C and finally to dimple mode fracture at 600°C (Figure 2.8) [28].

16

The reduced susceptibility to cracking of high carbon alloys was attributed [7,8] to (i) likely decrease in hydrogen solubility with increasing carbon content of the alloy and (ii) hydrogen entrapment by the precipitates. The surface cracking has been attributed to hydrogen liberated by the reaction between aluminium in the alloy and water used as the coolant [7]. Addition of carbon leads to the formation of phase, which may improve machinibility by (i) reducing susceptibility to environmental embrittlement [7] and (ii) by allowing formation $Fe_{4-y}Al_yC_x$ of small even size chips during machining [8] in Fe-16Al (in wt %) alloys.

The addition of carbon resulted in a significant increase in yield strength [6]. This may be attributed to the presence of a large volume fraction of hard. $Fe_{4-y}Al_yC_x$ precipitates and the formation of a Fe_3Al - $Fe_{4-y}Al_yC_x$ duplex structure. Similar results were obtained for Fe_3Al-based alloys with lower aluminium content [6]. The drop in strength observed above 600°C has also been reported for the low carbon alloys with similar Al contents [9]. The increase in ductility above 600°C may be related to the changes in failure mode from cleavage to the more ductile mixed mode failure and a likely change from DO_3 to B2 order in the material. Since the yield strength sharply fall for these intermetallics above 600^0 C irrespective of their carbon contents, it appears that the addition of carbon does not significantly affect the DO_3 to B2 structure [5].
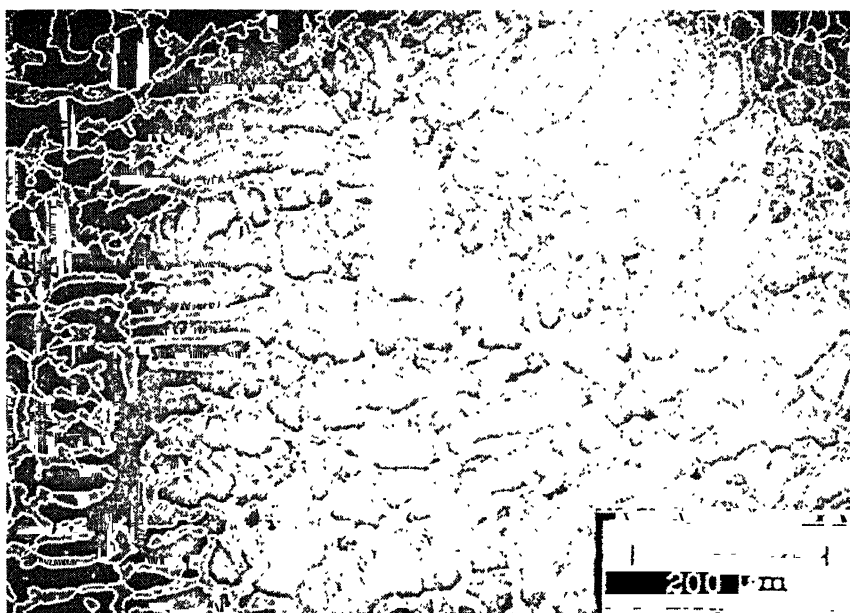
(a)
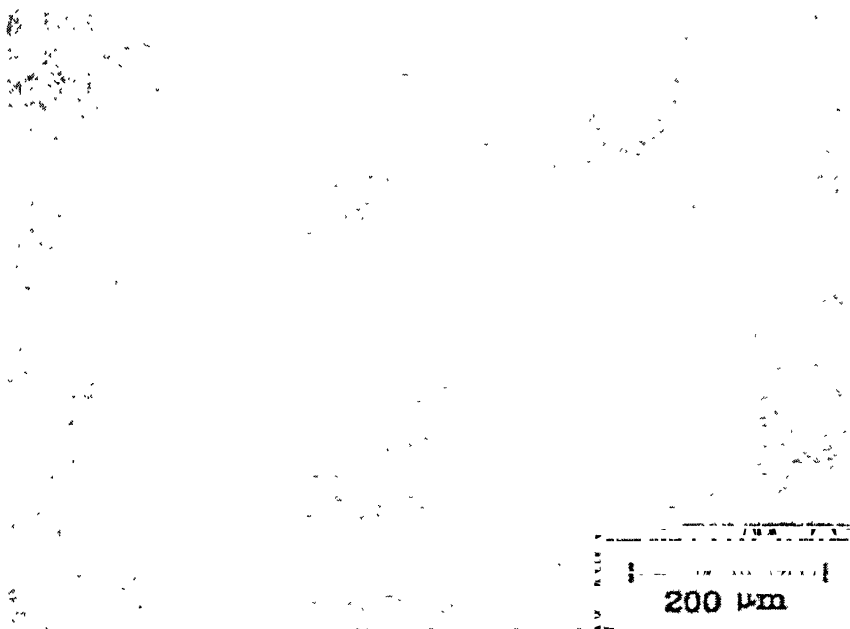
(b)

Figure 2.7   Optical micrographs of longitudinal sections of cast (a) AIM and (b) ESR ingots showing extensive precipitation of $Fe_3AlC_{0.5}$ [5]
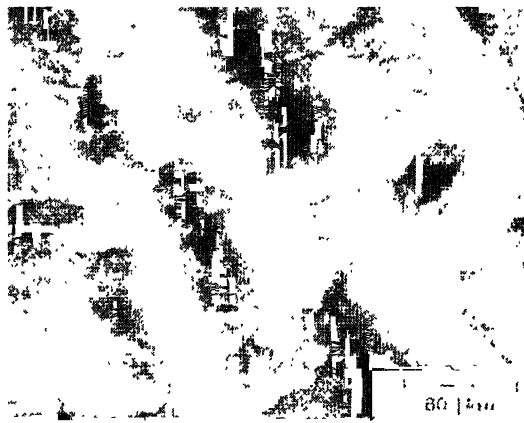
(a)
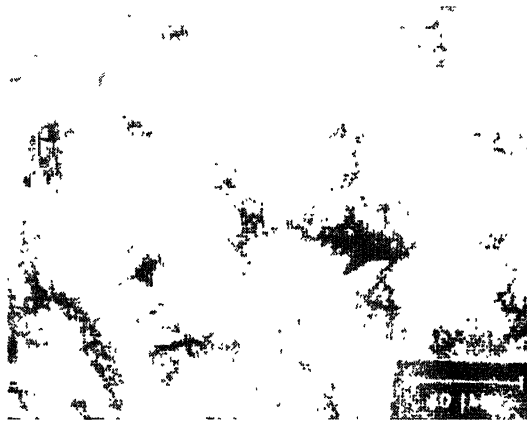
(b)
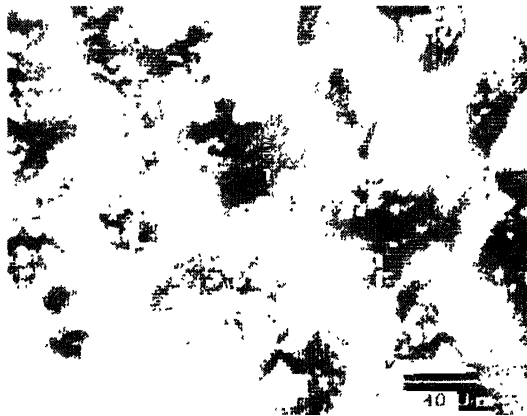
(c)

Figure 2.8   SEM fractographs showing the change in tensile fracture mode from (a) cleavage at room temperature to (b) mixed (dimple + cleavage) failure 400°C to finally (c) dimple failure at 600°C in a cast ESR Fe-8.26Al-0.46C alloy

The addition of carbon to Fe-Al alloys resulted in significant strength. At very low Al-contents (e.g. 8.5 wt % Al), the alloy is not susceptible to environmental embrittlement and the increase in strength is accompanied by a drop in ductility due to the presence of $Fe_{4-y}Al_yC_x$ precipitates. At higher Al contents (16-20 wt %), where the alloys are susceptible to environmental embrittlement, the benefits include improvement in machinibility and strengthening without loss of ductility. However, the strength drops on increasing the Al-content from 16 to 20 wt %. Similar results have been reported for low carbon alloys where the loss in strength with increasing Al content has been attributed to weaker DO_3 order and increased dislocation mobility. On increasing the Al-content to still higher levels, the strength starts increasing after 23 to 24 wt % (38-40 at %) Al when the alloys have a B2 structure. However, any carbon added to alloys containing more than 22 wt % (36.5 at %) Al is likely to precipitate out as graphite, which is a very soft phase. It is, therefore, unlikely that the addition of carbon to B2 Fe-Al alloys will lead to significant strengthening. Cast Fe-Al alloys with low carbon contents exhibit poor ductility (1-3%) and optimum ductility is obtained only after extensive thermomechanical processing. In contrast high carbon ESR alloys exhibit good (4-5%) ductility even in the cast condition. It is also observed that further increase in carbon content from 0.14 to 0.5wt% does not improve the creep and stress rupture properties [14, 6].

2.4. Hydrogen entry mechanism into metals and materials

Molecular hydrogen gas can readily enter a molten metal surface, often added accidentally as water contained in fluxes, mould dressings and alloying additions, dissociating into the mono-atomic form on dissolution, and remaining as a mono-atomic solute on solidification. The diatomic hydrogen molecule is too large to enter the surface of a solid metal, and must be dissociated into single atoms. Two mechanisms for this are known, electrochemical and chemisorption.

2.4.1. Electrochemical evolution

The electrochemical evolution of atomic hydrogen is one of the cathodic reactions in either a corrosion cell or an electroplating process. In addition, these can include processes such as acid cleaning and cathodic protection systems. As corrosion is

essentially an electrochemical mechanism, both are sufficiently similar to be considered identical for the purpose of hydrogen evolution, and take the form:

$$M + H_2O = MO + 2H \qquad\qquad \text{eqn. 2.3}$$

Most of the hydrogen atoms thus formed quickly combine to form diatomic gaseous hydrogen, but a portion of it enter the metal surface and remain as individual atoms in solution [13. 14].

2.4.2. Chemisorption

Chemisorption dissociation of hydrogen (Figure 2.9) is a rather different mechanism, and is well described by Christmann [16]. As a hydrogen molecule approaches a metal surface, weak Van Der Waal's forces begin to act upon it, drawing it closer. The molecule reaches an energy well, E_p, at distance Z_p, close to the surface, and very large forces would be required to force it any closer in a molecular form (Figure 2.9). At this point, however, the dissociation energy for the hydrogen molecule, typically 432 kJ mol^{-1} is exceeded by the chemisorption energy, which varies typically between 500 and 600 kJ mol^{-1}, depending on the metal involved [16]. Thus, the hydrogen molecule can be cleaved into two individual atoms, which are individually attracted to the surface by chemisorptive forces. At room temperature, these atoms enter an energy well, E_{ch}, which is closer to the surface than E_p, but are still prevented from reaching the metal surface. At higher temperatures, however, sufficient thermal energy is available to increase the vibrational amplitude of both, the hydrogen atoms and those of the metal surface, and individual hydrogen atoms can reach and enter the metal surface [16].
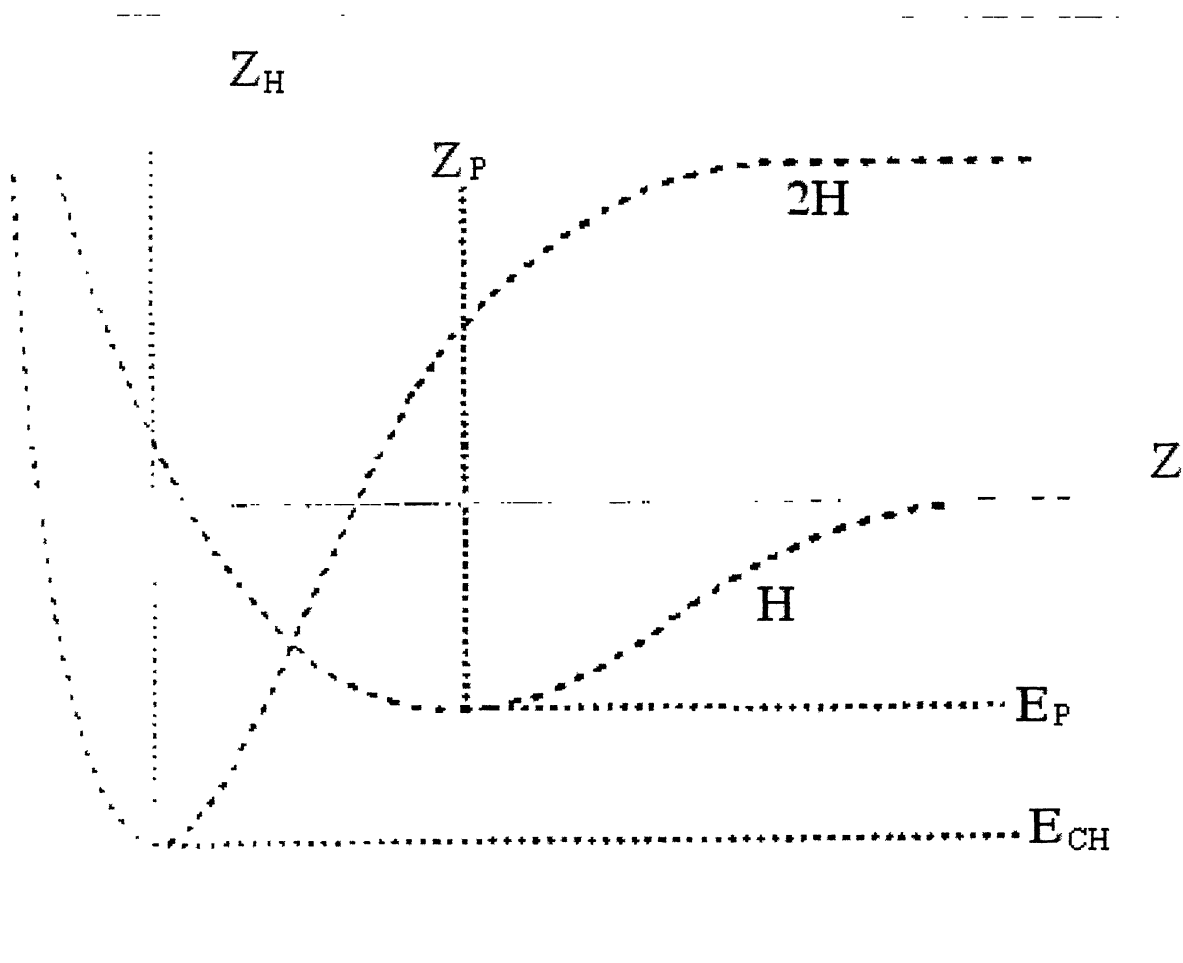
Fig. 2.9   Chemisorptive dissociation of hydrogen [16]

2.4.3. Hydrogen diffusion in iron aluminides

The pronounced susceptibility of iron aluminides to hydrogen embrittlement has been suspected to be consequence of ordering effects on diffusion behavior or of an enhanced fracture mechanism [15]. Long-range order generally is considered to slow down the process of hydrogen diffusion. However, extensive experimental data on room temperature diffusivity of hydrogen in iron aluminides is lacking. It has been already reviewed that cracking caused in iron aluminides is due to hydrogen. Recently Zhu *et al* have provided a direct evidence of hydrogen generation from the reaction of water with Fe-38.5Al using laser desorption mass spectroscopy [15]. The following subsections review the entry of hydrogen and its effect on the substructure of iron aluminides.

The diffusivity of hydrogen in four iron aluminides was determined by the technique of subscale microhardness profiling [16]. The diffusivity of hydrogen (in m^2/s) is 1.46×10^{-14} in Fe-28Al, 4.37×10^{-15} in Fe-28Al-2Cr, 5.45×10^{-15} in Fe-28Al-2Ti and 4.98×10^{-15} in Fe-28Al-1Cr-1Ti [19]. Similar values were obtained after hydrogen charging in NaCl solution. The important conclusion was that alloying with Cr or Ti lowers the diffusivity of hydrogen by an order of magnitude compared to the base intermetallic [19]. The diffusivity of hydrogen in Fe-38Al was also estimated by mathematical analysis of hydrogen concentration versus depth data obtained by Zhu *et al* [18] by applying the diffusion standard equation. It was found to be 2.38×10^{-15} m^2/s at room temperature.

As regards diffusivity of hydrogen in pure Al and α-Fe, there are several published reports that are available. The topic of hydrogen diffusion in pure α–Fe has been reviewed by Völkl and Alefeld [21, 22] and by Kiuchi and McLellan [23]. Figure 2.10 [21] and Figure 2.11 [23] show the values of diffusion coefficient of H in α-Fe obtained by various researchers. The feature that is to be observed is the relative large scatter in the experimental diffusivity data for hydrogen in iron, especially for temperatures lower than about 300K. This has been attributed to the errors in the experimental procedure which normally result in lower hydrogen diffusivity due to surface effects, defects in the surface regions like trapping sites, defects in the bulk regions like dislocations and impurity atoms, and surface oxide effects [23]. From these

figures, it can be seen that the room temperature diffusivity of hydrogen varies from 10^{-8} m^2/s to $10^{-12}\,m^2/s$.

Chiu *et al* have employed an electrochemical permeation technique to measure the room temperature diffusivity of an alloyed Fe_3Al-based alloy, recently [24]. The iron aluminides were ordered to obtain the B2 structure. The calculated diffusivity value was of the order of $10^{-9}\ m^2/s$ which they claimed was reasonable based on the fact that hydrogen diffusivity in BCC metals at room temperatures were of the same order magnitude.
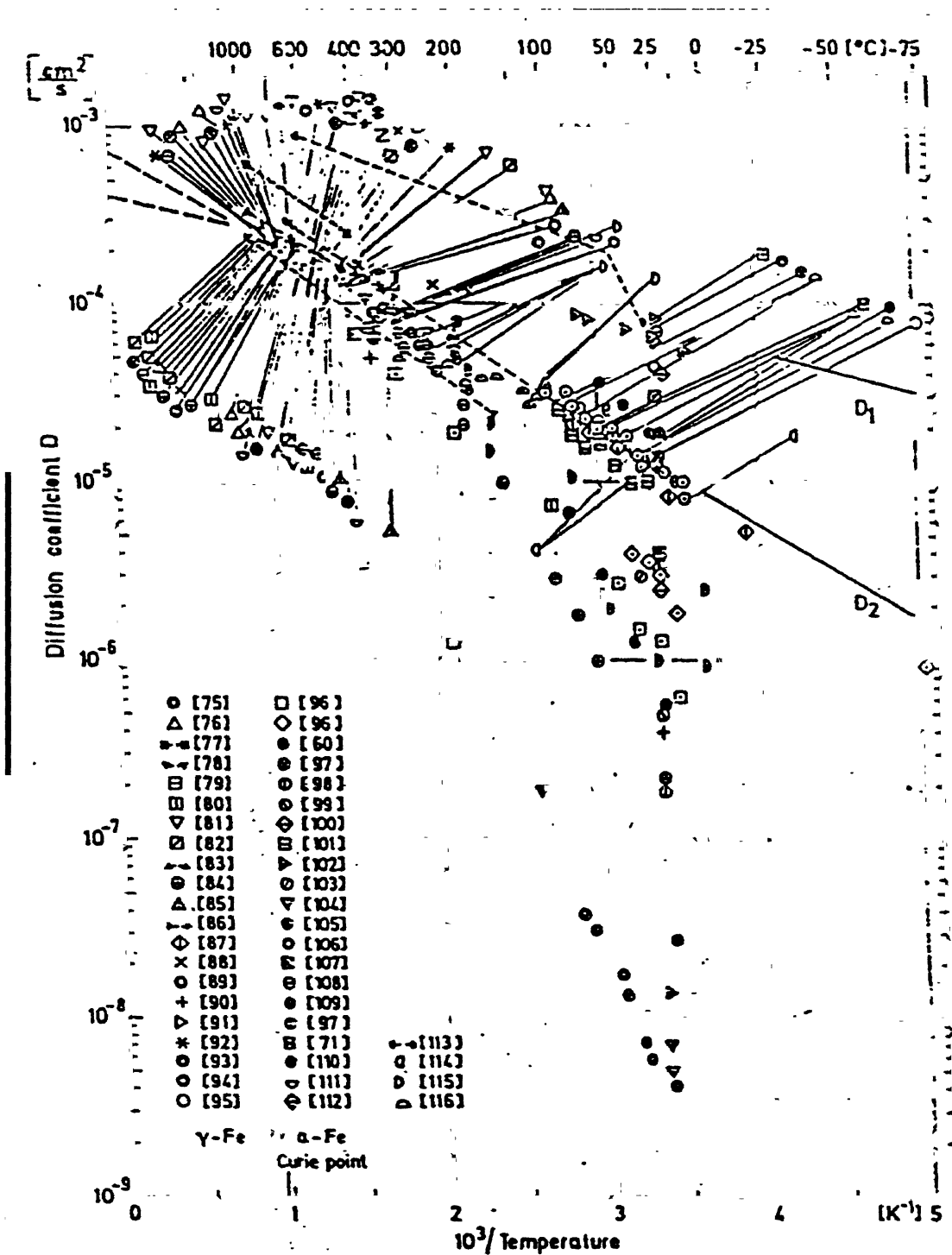
Figure 2.10   Diffusivity of hydrogen in α_{Fe}. (Numbers in brackets refer to literature cited in reference 21).
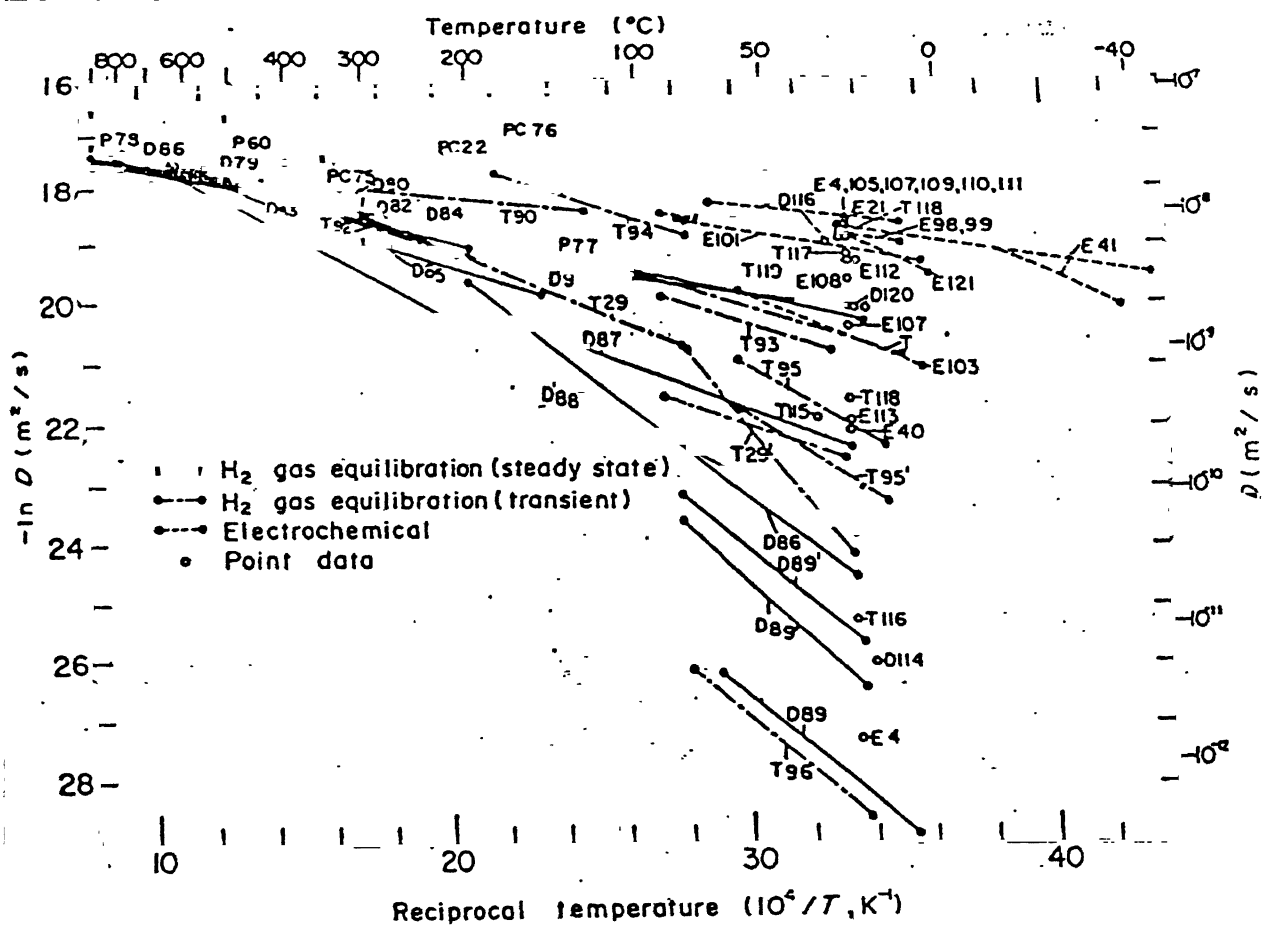
Fig. 2.11   Arrhenius representation of diffusivity of hydrogen in α_{Fe} [26]

2.5. Irreversible hydrogen trapping in iron aluminides

One of the impediments to the commercial application of iron aluminides is their poor room temperature ductility, which is due to their susceptibility to hydrogen embrittlement (HE). It is well known that hydrogen has to be accumulated at certain region in the lattice and once a critical hydrogen concentration is achieved, HE occurs. In this regard, both reversible and irreversible trapping of hydrogen has to be considered. Trapping of the hydrogen in the metal is likely to affect the HE. It is well known that certain elements or compounds when present in alloys act as trap sites for hydrogen. Traps can be classified as either reversible or irreversible, based on the binding energy of traps with hydrogen. They may be mobile (dislocations) or stationary (solute atoms, particles, grain boundaries) [25]. For, example Ti in steel acts like a reversible trap while incoherent TiC precipitates in steels are irreversible traps (due to trapping at the inclusion-matrix interface) [26].

Because traps are associated with various microstructural features, alloying and metallurgical treatments to modify trapping properties offer a promising avenue to the development of alloys with maximum resistance to hydrogen damage. Deep or irreversible trapping reduces the population of hydrogen at the crack tip and often increases resistance to hydrogen induced cracking (HIC) [25]. Conversely, shallow or more reversible traps permit more rapid hydrogen transport, which allows some traps to reach a critical concentration necessary to initiate cracking.

If the irreversible traps are finely and homogeneously distributed throughout the matrix, there is a good likelihood that hydrogen would be irreversibly trapped at these sites and hydrogen can not accumulate at critical regions to cause embrittlement. Therefore, addition of elements or compounds which can act as irreversible traps for hydrogen could also be envisaged to improve ductility of iron aluminides. However this may not be promising route because there would be sufficient accumulation of hydrogen, with time, at these locations and once the hydrogen concentration exceeds the critical concentration for embrittlement, the material would be susceptible to embrittlement. It should be noted that hydrogen appears to be generally trapped

reversibly in both Fe-25Al and Fe-35Al based on the reversible nature of embrittlement (i.e. recovery of ductility on baking treatments) [26].

Recently Baligidad *et al* have reported that addition of carbon in the range of 0.14 to 0.50 wt % significantly increases the room temperature strength of Fe-16 wt % (28 at %) Al alloys [27]. These alloys also exhibited good room temperature ductility. The improvement in ductility on C addition to iron aluminide also must be related to irreversible hydrogen trapping at the $Fe_{4-y}Al_yC_x$ precipitates [28]. This $Fe_{4-y}Al_yC_x$ phase has FCC crystal structure with Al atoms at the corner positions, Fe atoms at the face centered positions and carbon atom at the body center position (i.e. at the octahedral void) in the cube.

The diffusivities of hydrogen in Fe-16.2Al-0.54C and Fe-16.0Al-0.9C (in wt %) were determined by the technique of subscale microhardness profiling [48]. The diffusivity of hydrogen (in m^2/s) was estimated as 9.33×10^{-15} and 8.62×10^{-15} for these two alloys, respectively. It is evident that the alloy with higher carbon percentage (and thus higher volume fraction of carbides) showed lower hydrogen diffusion. This was attributed to the irreversible hydrogen trapping by the carbides [48].

2.6. Damage caused by hydrogen

Damage of metals due to the influence of hydrogen is quite frequent and leads to dangerous failures as well as loss of large amount of property. Practically all metal materials can be damaged by the absorption of hydrogen, if a sufficient amount can be penetrating into material. In most metals, the solubility of hydrogen at room temperature is very low. Nevertheless, its presence strongly influences their mechanical properties. Mainly three types of damage caused by hydrogen are observed in metals [16]. Those are

- Hydrogen embrittlement,
- Hydrogen induced stress corrosion cracking, and
- Hydrogen attack.

Hydrogen embrittlement and hydrogen attack are different phenomena in the sense that hydrogen attack, unlike hydrogen embrittlement, involves the formation of a second phase (methane) by the solute hydrogen, and, unlike hydrogen embrittlement, is

an elevated temperature phenomenon. It is usually considered that hydrogen attack is irreversible and occurs only above 200^0C; while hydrogen embrittlement is irreversible and occurs below 200^0C [16, 29-31].

Hydrogen induced stress corrosion cracking is a transition form between the classical hydrogen embrittlement and stress corrosion cracking and applies in particular to high-tensile steel in low aggressive water solution, austenitic steel in diluted sulfuric acid, alloys in halogenide solutions and uranium alloys in water solution [25, 63].

2.6.1. Hydrogen embrittlement

Hydrogen embrittlement occurs when solute hydrogen gas accumulates on lattice defects, usually dislocations and interfaces between the metal and a second phase, or grain boundaries, the latter two of which features can be considered to be complex dislocation arrays, restricting ductility and promoting brittle behavior. Embrittlement is observed as a loss of macroscopic ductility or as a loss of local ductility at the crack tip. This phenomenon occurs through a lowering of lattice cohesive strength. Hydrogen is able to produce two type of embrittlement,

- An atomistic embrittlement that always occurs when hydrogen is present, and
- A microscopic embrittlement that occurs only when sufficiently high concentration of excess hydrogen are present to cause high internal pressure. Both of these effects can lower the tensile stress required to spread an incipient microcrack nucleus [32].

The fracture processes typical of hydrogen embrittlement requires extensive localized deformation and are thus consistent with a model based on hydrogen transport by dislocation to create high localized hydrogen concentrations and subsequently high hydrogen pressure at microvoids and other volume defects in the lattice. This high pressure may aid in the extension of the defect by either continued plastic deformation or by brittle fracture until the internal pressure is subsequently reduced [33].

Hydrogen sources

Two common forms of hydrogen embrittlement exist, differentiated by the method by which hydrogen is introduced into the material, welding and surface electrochemical processes and reactions [16].

Welding

During fusion welding operations, hydrogen enters the molten weld pool. While the weld area remains hot from the welding process, this hydrogen diffuses away from the weld fusion zone and into the adjacent parent material (HAZ). Thus embrittlement occurs (Figure 2.12). In spite of the ease with which hydrogen cracking can be eliminated, and the high degree of understanding of the mechanism responsible, it remains a major cause of weld failure [16].

Surface electrochemical processes

Hydrogen is evolved in a mono-atomic form as part of the cathode reaction of almost any electrochemical reaction, several of which are commonly applied to ferrous surfaces. Common examples are processes such as electroplating and acid pickling, both of which are almost notorious causes of post-processing failure through hydrogen embrittlement. Another, less obvious, electrochemical mechanism is almost any aqueous corrosion process. In most instances, the level of hydrogen generated is insufficient to cause problems. The affected layer is removed by the corrosion process itself before any damage can be done by the hydrogen evolved in those cases. However, the ability of corrosion to utilize hydrogen in its destructive workings should never be underestimated [16].

Hydrogen may also enter the metals and alloys from hydrogen-bearing atmospheres during heat treatment or other manufacturing processes. Water vapour and steam may be decomposed to hydrogen at hot surfaces during those processes. Damage often occurs during exposure to a hydrogen-bearing environment [25].

2.6.2. Hydrogen-induced stress corrosion cracking

This type of damage is a transition form between the classical hydrogen embrittlement and stress corrosion cracking and applies in particular to high-tensile steel in low aggressive water solutions, austenitic steel in diluted sulfuric acid, alloys in halogenide solutions and uranium alloys in water solutions. When subjected to sustained load, a steel containing hydrogen may fail at a stress level that is much below its tensile strength [25, 63]. A typical example of transgranular hydrogen induced cracking in precipitation-hardened steel showing cleavage-like fracture planes, micropores, and ductile hairlines is presented in Figure 2.13.

When a building component or system is subjected to corrosion created by the development of hydrogen, the cathodically isolated hydrogen diffuses into the material and causes local embrittlement. The hydrogen develops either in oxygen-free, neutral or alkaline mediums by the reduction of water molecule or as a result of hydrolysis of corrosion products (in pitting locations, narrow cracks). In acid solutions (pH<4) the protons H^+ are reduced to H_2 [18]. In general, acid corrosion of steel in diluted halogenide solutions emanates from an acid corrosion mechanism in narrow gaps. The diffusion processes cause increased concentrations of halogenide and metal ions inside the cracks and, due to hydrolysis, the pH value in the crack sink. In addition, a decrease in the potential independent of the external polarization can be detected in the narrow cracks and splits. This is caused by the development of H_2 gas bubbles which leads to the production of a "short circuit cell" (occluded corrosion cell) at the crack opening which to a great extent is decoupled from the surface. Molecular hydrogen is less damaging for steel than atomic hydrogen due to its high dissociation constant at room temperature. When kinetic inhibition of recombination exists, as is the case with the presence of, for instance, sulfides, arsenic, selenium and phosphorus compounds, considerable partial pressures can occur due to the accumulation of adsorbed hydrogen atoms on the surface. The interstitially dissolved hydrogen is particularly mobile in steel. The diffusion coefficient of steel is between 10^{-4} and 10^{-5} cm^2/s, which is comparable with diffusion coefficients in fluids. Therefore, as soon as the hydrogen has penetrated through the phase boundary into the metal, it is capable of penetrating to a depth of 100 m into the material [18]. Thus, a lattice deformation takes place and also an accumulation of

31

hydrogen on the boundary surfaces (e.g. at grain boundaries, pores and inclusions). It can be proved that, with the increasing strength of the steel, a notched sample subjected to homogeneous hydrogen produces inhomogeneous distribution of the hydrogen. The hydrogen is concentrated in the range of the maximum hydrostatic stress in the ligament. If at first the material is hydrogen-free, for the same reason, the hydrogen absorbed on the crack edges is distributed selectively into the crack ligament. In this case the corrosive hydrogen is concentrated where the most damage exists, which is in cracks, notches or other material defects that cause an increase in stress. Therefore this type of material damage should not be considered as global but as very local hydrogen embrittlement [18].

2.6.3. Hydrogen attack

HA occurs as a result of atomic hydrogen diffusing into the steel and combining with carbon in solution to from methane, which remains trapped internally as bubbles. The localized internal decarburization and the build up of methane pressure results in fissures, which induce an apparent embrittlement of the macroscopic section of the steel and cause a loss of strength, swelling and ultimately fracture (Fig. 2.14). The temperature range for hydrogen attack of carbon steels extends from about 200^0C to 550^0C [25, 29, 63]. This temperature coincides with the range of service temperatures of steel in petroleum refining and other equipment. The items of equipment with which hydrogen attack is normally associated are usually items of hydrocarbon processing plant, which spend substantial periods of time, years rather than hours, at high temperatures and in contact with hydrogen. Thus they can be considered to operate in equilibrium conditions from microstructural and metallurgical thermodynamics aspects. While in contact with hydrogen containing process streams in such plants, the hydrogen is normally either molecular or combined with carbon, and the electrochemical processes responsible for the monoatomic hydrogen causing hydrogen embrittlement are absent because of the lack of water in the process stream. However, the previously discussed chemisorption mechanism can provide a source of individual hydrogen atoms at a metal surface in the absence of an aqueous electrochemical mechanism. When the chemisorbed hydrogen enters the structure, it reacts with the solute carbon in the α-Fe structure and destroys the

equilibrium of the α-Fe phase with carbon. As the system is operating under essentially equilibrium conditions, more non-solute carbon, in the form of metal carbides will dissociate, and redissolve in the α-Fe phase to restore the equilibrium altered by the reaction. Thus the material appears at a macro-scale to become decarburized, and this is the initial indication of hydrogen attack when normal macro scale examination techniques are employed. The rate of supply of carbon to restore the equilibrium solute carbon concentration will depend upon a number of factors. The dissociation of carbides is an Arrhenius-rate controlled process, and is consequently dependent upon the temperature. In addition, the binding energy of the specific carbide will be a factor, with the more stable carbides releasing carbon more slowly and at higher temperatures [16, 31].

As the supply of hydrogen continues, an increasing amount of methane is formed, consuming more and more carbon. The methane molecule is large, and is immobile in the lattice, and voids are formed in the microstructure. It is believed that these voids grow initially by the diffusion of iron atoms away from the void that is essentially a vacancy condensation mechanism [29-31]. After reaching a critical size, growth is by power-law creep driven by the increasing methane pressure within the void (Figure 2.15).

The pressure of methane within the voids can reach very high values, at which the behaviour of methane as a non-ideal gas becomes very relevant and the difference between methane pressure and methane fugacity becomes a major consideration in the prediction of void growth by creep [16, 30, 31].

The usual means of predicting the behaviour of materials in high pressure, high temperature hydrogen is Nelson curves (Figure 2.16). These curves delineate the safe and unsafe hydrogen pressure-temperature regimes for carbon and alloy steel in a purely empirical manner [37]. Understanding of the phenomena responsible for this degradation is far from complete, and therefore, the Nelson curves cannot be extrapolated to different environments, service conditions or steels. Recently, these curves have been updated, as new data becomes available, and form the basis for material selection for hydrogen service [16].
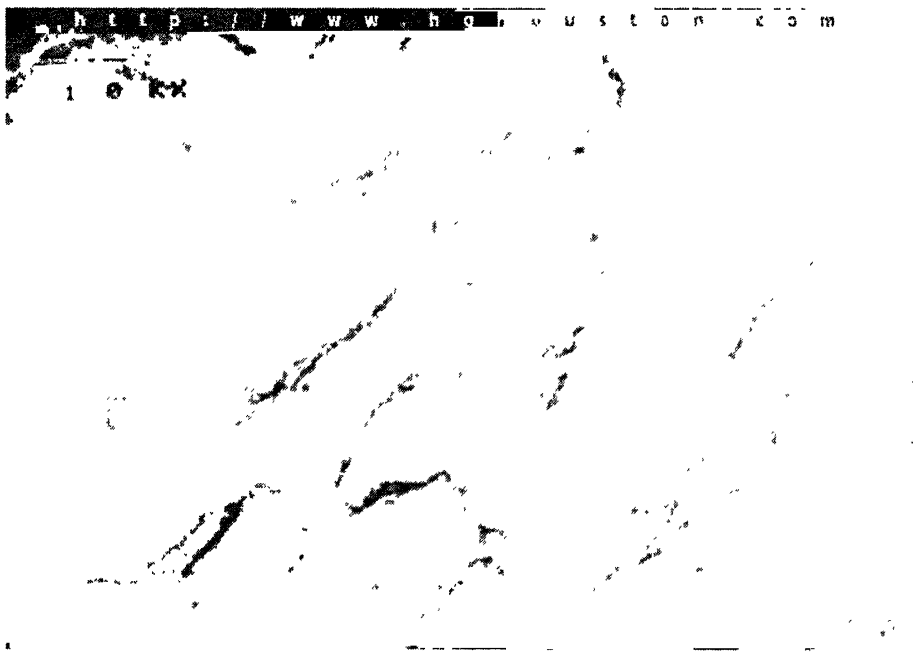
Figure 2.12   Fracture surface of a cap-screw that failed due to hydrogen embrittlement

Figure 2.13   Transgranular hydrogen induced cracking in precipitation-hardened steel showing cleavage-like fracture planes, micropores, and ductile hairlines [25]
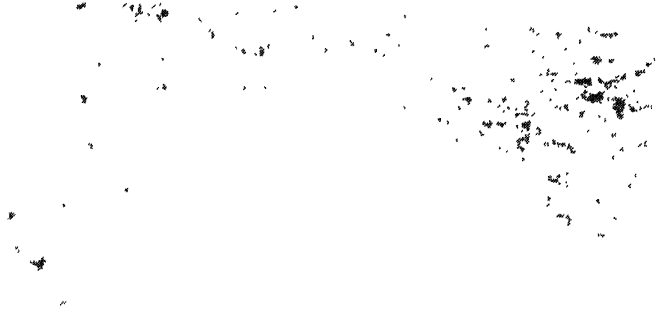
Figure 2.14   Hydrogen attack corrosion and cracking on the on the ID of an carbon
steel boiler tube
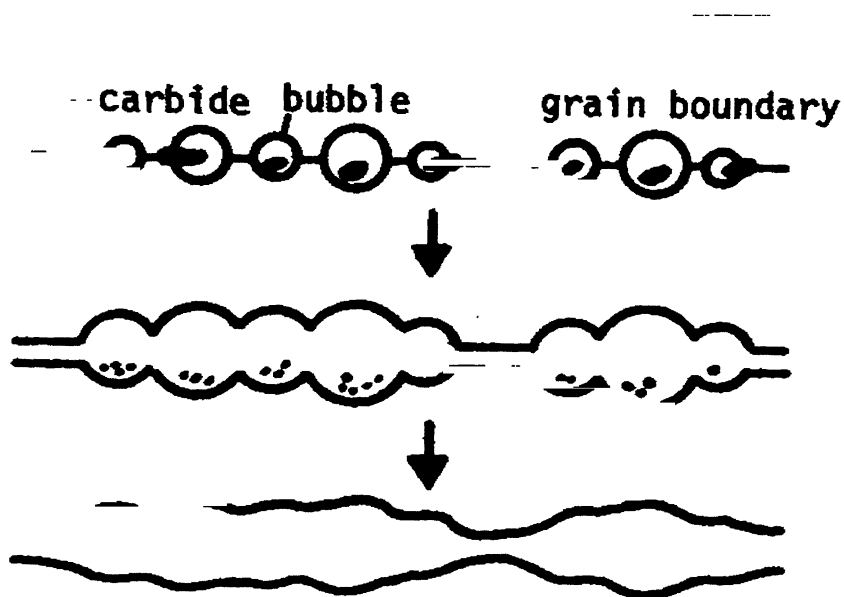
Figure 2.15   Schematic illustration showing the process of bubble growth and failure of
grain boundary

Figure 2.16   Nelson curves for hydrogen attack [29]

2.6.3.1. Stages of HA

Hydrogen attack is a form of internal decarburization associated with steels that are exposed to hydrogen at high temperatures and pressures. HA is caused by the nucleation, growth, and coalescence of methane bubbles, primarily along the grain boundaries. Methane is produced by an internal reaction between carbon and hydrogen. This phenomenon is observed for many years in both the petrochemical and the synthetic ammonia industries. HA separates itself kinetically into the three following stages [29, 31]:

- Incubation stage
- A stage of rapid attack
- A steady state stage.

Incubation stage

The incubation stage is the initial period of time during which damage of the material is not apparent. However, small bubbles of methane are formed in this period, and methane pressure builds up in submicroscopic voids. These voids grow slowly due to both internal methane pressure and applied stress. No noticeable change in properties is detectable by current mechanical testing methods in this period [29]. This period varies with the type of steel and severity of exposure; it may last only a few ours under extreme conditions (very high temperature and high hydrogen pressure associated with external applied stress) and become progressively longer at lower temperatures and pressures. Incubation time appears to be related to the growth of methane bubbles since it can be used as normalizing factor for exposure time and bubble size [29, 31]. With some steel under mild conditions, no damage can be detected by mechanical testing methods even after many years of exposure [29].

Rapid attack stage

As a considerable amount of methane pressure is formed inside the voids along the grain boundaries, the stresses inside the voids are increased. The growth of voids occurs due this increase in stresses. The pressure of the methane formed may exceed the

37

cohesion strength of the steel and cause intergranular fissuring [29]. The mechanical properties of the steel get affected badly due to this void formation and growth. After a certain period, depending on the operation-temperature and the hydrogen pressure, voids reach a critical size. At this critical size of voids, rapid fissure growth occurs and the mechanical properties of the steel deteriorate severely. A marked reduction of the strength and ductility of the steel is observed in this stage. As the incubation period, this stage is also depends similarly on the operation-temperature and the partial pressure of hydrogen [29, 31]. There are so many testing methods, with the help of which, this stage can be detected properly. The detection methods are discussed in this chapter later.

Steady state stage

During the previous two stages carbon from the solid solution of iron and carbon comes out and get reacted with hydrogen and thus, the solid solution becomes lean in carbon. At the steady state stage or final stage carbon in solid solution is exhausted and a large amount of methane is formed inside the fissures. Due to this very high pressure of methane inside the fissures a significant loss in mechanical properties, *i.e.*, a great loss in strength and ductility occur. And after a certain pressure of methane, depending on the cohesion strength of the steels, fracture will take place [29, 31]. As stated earlier, there are a number of effective testing methods are now available to detect this stage. The detection methods are discussed letter on.

2.6.3.2. *Forms of HA*

HA occurs in steels in two ways [29], surface decurburization, and internal decurburization and cracking. The combination of high temperature and low hydrogen partial pressure favors surface decurburization without internal decarburization and cracking. The combination of low temperature, but above 200°C, and high hydrogen partial pressure favors internal decarburization and cracking.

Surface decarburization

It does not produce fissures. In this respect, it is similar to decarburization created by the exposure of steel to certain other gases, such as air, oxygen, or CO_2. The usual

effects of surface decurburization are a slight, localized reduction in strength and hardness and an increase in ductility. Because these effects are usually small, there is often much less concern with surface decurburization than there is with internal decarburization [29].

A number of theories have been proposed to explain this phenomenon, but the currently accepted view is based on the migration of carbon to the surface where gaseous compounds (CH_4; or when oxygen-containing gases are present, CO) of carbon are formed, rendering the steel less rich in carbon [29, 31]. Water vapour hastens the reaction. Carbon in solution diffuses to the surface so that the rate-controlling mechanism appears to be carbon diffusion. As the carbon in solution is continuously supplied from the carbides, carbide stability is directly related to the rate of surface decarburization [29].

In cases where surface decarburization predominates over internal attack, the actual values of pressure/temperature combinations have not been extensively studied; however, the limits defined by Naumann [29] probably gives the most accurate trends. Due to him, long-duration exposures have indicated lower operating limits.

Internal decarburization

The solid-line curves in the Nelson curves shown in Figure 2.16 define the areas above which steel damage by internal decarburization and fissuring is observed. Below and left to the curve for each alloy, satisfactory performance have been experienced with periods of exposure of up to approximately 40 years. At temperature above and to the right of the solid curves, internal decarburization occurs. Internal decurburization and fissuring are preceded by an incubation period that depends on temperature and pressure.

Internal decarburization and fissuring are caused by hydrogen permeating the steel and reacting to form other gases, such as methane. The methane formed cannot diffuse out of the steel and typically accumulates at grain-boundary voids. This results in high localized stresses, leading to formation of fissures, cracks, or blisters in the steel. These defects cause substantial deterioration in mechanical properties. The addition of carbide stabilizers to steel reduces the tendency toward internal fissuring [29]. Elements such as Cr, Mo, W, V, Ti, and Nb reduce the number of nucleation sites by forming more

stable alloy carbides that resist breakdown by hydrogen and thus decrease the propensity to form methane [29].

The presence of non-metallic inclusions tends to increase the extent of blistering [35]. When steel contains segregated impurities, stringer-type inclusions, or laminations, hydrogen or methane accumulations in these areas may cause severe blistering. Additionally, sound welds with a minimum number of inclusions are essential in hydrogen service [35].

2.6.3.3. *Effect of parameters on HA*

Temperature:

At a constant pressure, Fig. 2.17 shows that an increase in exposure temperature increases the rate of methane bubble growth inside the fissure. Since increasing temperature decrease the driving force for formation of methane, it is not likely that a higher concentration of methane is responsible for this effect. Rather, the increase in bubble growth rate with increasing temperature is caused by more rapid vacancy diffusion to the bubble [30].

When the growth of gas bubbles involves a larger amount of vacancy diffusion in reaching equilibrium, the bubbles often take on the shape of irregular polyhedra. The faces of these polyhedra are the low indices crystallographic planes, usually {100}, {110}, or {111}. Due to the difference in surface energy of the various crystallographic planes, vacancies diffusing to a bubble may obtain a larger decrease in the total free energy of the system by condensing on the low indices planes. Thus faceted bubbles result [30].

Hydrogen pressure:

In Fig. 2.18 the effect of hydrogen pressure variation at a constant temperature is illustrated. The position of these curves show that less time is needed to attain appreciable bubble size if the hydrogen pressure is increased. Comparison of the slopes of these isobars also shows that the growth rate of the bubbles is increased as pressure increased [30].

Diffusion of vacancies to bubble nuclei to enable growth to occur should not be affected by pressure variation in this manner. Fig. 2.18 indicates increased methane production as hydrogen pressure is increased. This may be expected for two thermodynamic reasons. Since hydrogen obeys Sievert's law in the temperature range where HA is prevalent, more hydrogen is available for reaction with higher exposure pressure. Secondly, hydrogen acts almost ideally in having increased fugacity as its pressure is increased, and thus becomes more likely to react with the carbon [30].
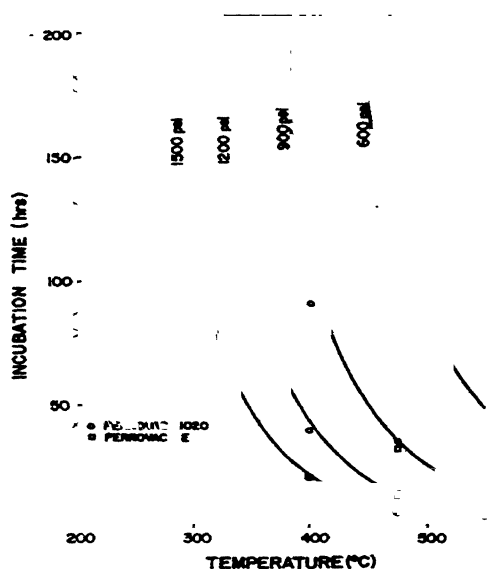
Figure 2.17 Incubation time at various exposure conditions
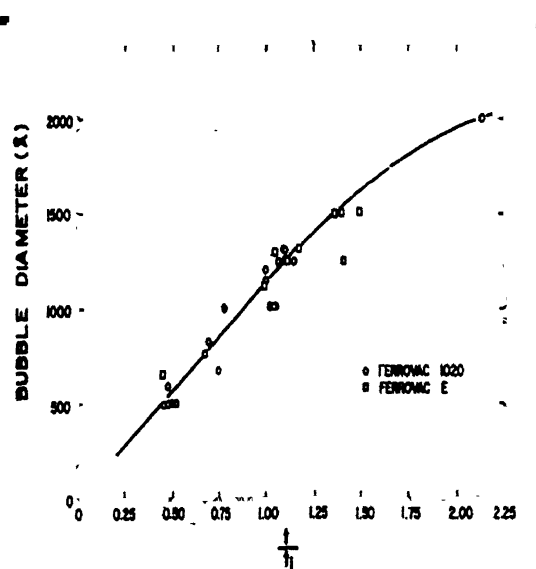
Figure 2.18 Effect of pressure on bubble growth

Impurity elements (P, As, Sb, Sn and Si):

HA is characterized by methane bubbles, which nucleate at carbides on grain boundaries and grow. In this sense, HA is an intergranular failure phenomenon. Impurity elements like P, As, Sb and Sn and an alloying element Si play significant roll in HA of steels. Sakai and Kaji performed extensive experiments on 2.25Cr-1Mo steel to study this aspect. P and As were found to restrict the methane bubble formation, whereas Sn and Si have the effect to promote bubble formation (Figure 2.19).

P and As:

Sakai *et al.* showed that P containing steels possesses low methane bubble density (the number of bubbles per unit area of the grain boundary) and larger bubbles. Since nucleation sites are mainly carbides on grain boundary, the number of carbides is an important factor determining the bubble density. However, the carbides in the P containing steels were much more than the bubbles and, further, did not seem to be less than those in the other steels as shown in Fig. 2.19. Other possible mechanism that may account for the decrease in bubble density is adsorption of P to the bubble surface. Since P is known to segregate strongly to grain boundaries (and to free surface) in steels, it is expected that P is absorbed to the surface of bubbles which nucleate on carbide particles in grain boundaries. The adsorption, on the one hand, improves the nucleation by lowering the surface energy by prohibiting hydrogen and carbon from adsorbing to the bubble surface. The prohibition means retardation of the methane formation reaction and causes lowering the pressure in bubble whish provides the driving force for bubble nucleation. In summery, it is probable that P restricts the bubble nucleation and reduces the bubble density through the adsorption to the bubble surface [35]. In the case where the step cooling treatment is given to the P-steels preceding the HA treatment, more P is segregated to the grain boundary and the effect of P must be intensified. Lowering of the bubble pressure also reduces the bubble growth rate or the bubble diameter. On the other hand, the low bubble density has a beneficial effect on the bubble growth because it can keep the carbon activity high during the bubble growth. This is may be the cause for bigger methane bubble in P-steels [35]. The effect of As on the bubble formation is essentially the same as that of P. this suggests that, although the segregation to As to
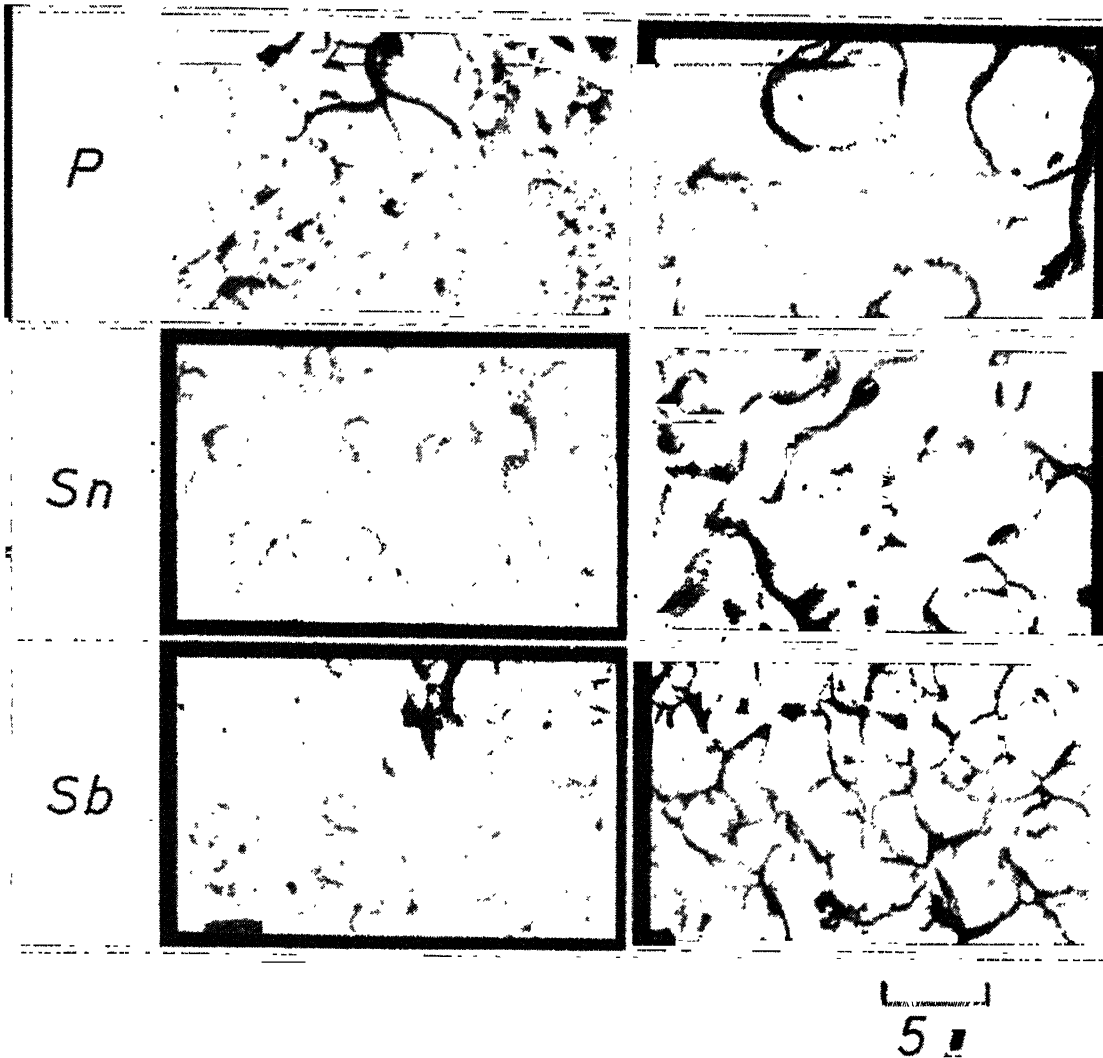
Figure 2.19   Scanning electron fractograph showing the effect of impurities on bubbles on grain boundaries

grain boundary has not been reported in 2.25Cr-1Mo steel, the same mechanism would be applied to the effect of As [35].

Sn, Sb and Si:

According to Sakai and Kaji the effect of Sn, Sb and Si on the methane bubble formation during HA was in contrast to that of P and As, *i.e.* addition of Sn, Sb and Si was beneficial for bubble formation. Sn did not segregate to the grain boundaries and to the bubble surface. Further the effect of Sn was not intensified by step cooling treatment. Another evidence is the fact that Sn does not temper embrittle steels indicates a strong repulsive interaction between Sn and C in Fe. Sn would reject carbon from solution and cause it to segregate to grain boundaries and to the bubble surface, activating the methane formation reaction. The same mechanism may be applied to the effect of Si and Sb; because it has been reported that Si does not segregate to the grain boundaries in 2.25Cr-1Mo steel and Sb does not embrittle this steel. However, the effect of Sb is not so strong that the reduction in carbon activity accomplished with the bubble growth could suppress the beneficial effect, leading to the retardation of the bubble growth rate [35].

The effect of Sn, Si and Sb, which promotes the bubble formation, seems to be offset by the addition of P and As which retards it.

2.6.3.4.   *The roll of gas venting*

As the HA of steel progresses, the methane bubbles linkup and vent the methane to the surface. This reduces the internal pressure and stops the swelling. The amount of swelling that occurs before venting is decreased by banding the steel, and by prior cold work. Banding tends to concentrate the bubbles in a plane. Cold work greatly increases the number of boundaries covered with bubbles. Since the complete decarburization of steel is often observed in steel that has undergone HA, one might expect that swelling continues until the carbon is exhausted [36]. However, inspection of Pishko's density data and his photomicrographs show that in his REM steel, the density changes significantly before any appreciable decrease in the volume of pearlite is observed. This leads to the suggestion that the expansion of steel undergoing HA is determined not by

the exhaustion of the carbide supply but by the venting of the methane to the surface, which relieves the internal pressure driving expansion.

Ransick and Shewmon have performed extensive experiments on this phenomenon on a silicon killed 1020 steel (0.2% C, 0.7% Mn, 0.3% Si, 0.022% S, 0.01% P). They determined that the methane filled fissures in steel undergoing HA vented the inside gas to the surface. This statement is supported by the observation of open fissures on the free surface, by vents formed on upraised disks above small inclusions, and by the observation of samples bent before HA that the surface vents parallel, and often merge with, internal fissures [36].

Bisaro and Geiger studied the evolution of CH_4 during HA. They reported occasional bursts which would raise the evolved CH_4 content well above that which could be accounted for by the diffusion of carbon to the outside surface and conversion there to CH_4. They suggested that these releases come from the rupture of blisters filled with CH_4. The bursts could equally come from the venting of deeper internal fissures.

The range of swelling values reported for steels undergoing HA has been substantial (2-10%) [36]. It could result from the differing times for the advent of venting. The rare-earth treated steel studied by Pischo [36] was banded and tended to form planes of bubbles along grain boundaries in the rolling plane. His samples were cut from plate with cuts normal to the rolling plane. Thus the planes of bubbles and the resulting fissures extended right up to a free surface. A minimal $\Delta v/v \cong 2\%$ resulted before swelling stopped. Decurburization proceeded without further growth.

Sorell and Humphries [36] have reported a quite deferent geometry for HA blisters. They showed examples of large blisters extending several inches along the circumference of an $8''$ diameter pipe. Here the rolling plane was in the wall, and the conditions of service (low hydrogen pressure and temperature for HA) were such that attack developed slowly and some surface decarburization occurred. The blisters tended to develop along the rolling plane and often followed long inclusions. Given decarburization and the absence of any cuts normal to the rolling plane (*i.e.* the circular pipe closes on itself), there were no easy paths for venting of methane to the surface. Low hydrogen pressure and low temperature also kept the methane pressure relatively low so that the blisters expand by creep rather than rupture due to high internal pressure. These

45

are the best conditions to minimize methane venting, and thus were conditions that give rise to the growth of large blisters by creep [36].

2.7. Stereology

Literally "stereology" means "the knowledge of space". Stereology is a body of mathematical methods relating three-dimensional parameters defining the structure to two-dimensional measurements obtainable on sections of the structure [38]. The stereological methods allow us to infer certain parameters of the structure from incomplete information, which is obtained from sections of a dimension lower than that of the original structure. The methods help us in determining the percentage of microconstituents in an alloy, which is beneficial in studies of equilibrium and transformation in solid state. Also, the correlation of mechanical properties with structure is likewise dependent upon quantitative microanalysis. Quantitative stereology is very efficient in not only to find means for measuring familiar geometric quantities but also to discover parameters that can be useful in establishing exact geometric relationships among properties of alloys. The parameters, which are discussed here, are

(i)   Volume fraction of different phases,

(ii)   Surface area of exploded features per unit volume,

(iii)   Contiguity of different phases,

(iv)   Size i.e. the mean intercept length of the grains of different phases,

(v)   Number density in two dimension of the grains of different phases,

(vi)   Probability of occurrence of different second phases, and

(vii)   Total edge length of the grains of the matrix in a unit volume.

2.7.1. Volume fraction

The volume fraction is one of the most important quantities required in quantitative stereological analysis. Random two-dimensional section planes may be utilized in different ways two obtain $\overline{V}_V$. There are three main methods to measure $\overline{V}_V$,

which are based on measurements of areas, measurement of lineal intercepts, and counting of points. These three methods are called areal analysis, lineal analysis, and point counting [37-40].

In 1848, French geologist Delesse recognized that volume fraction ($\overline{V}_V$) could be determined by measuring and summing the areas of intersection of a phase and then calculating the area fraction ($\overline{A}_A$) of that phases in microscopic sections.

In 1898, German geologist Rosiwal found that the same principle applies to linear fractions ($\overline{L}_L$). If a single random traverse is made on a randomly selected plan of polish, then the traverse can be regarded as having been placed at random in the three-dimensional structure, and the lineal fraction gives a direct estimate of volume fraction. However, a lineal analysis performed on a single plane of polish can never be more reliable, no matter how many traverse are made, than an aeral analysis of the same plane.

The first application of point counting method to structure analysis have been made in 1930 by Thomson. He superimposed a two-dimensional lattice on the structure either by the use of a ruled reticule in the eyepiece of the microscope or by the simultaneous projection of the lattice and a lanternslide of the structure. And in 1934, Glagolev developed the analogous principle for point fraction ($\overline{P}_P$). In the nomenclature of quantitative metallography developed by Underwood this is expressed by [37-40]

$$\overline{V}_V = \overline{A}_A = \overline{L}_L = \overline{P}_P \qquad \text{eqn. 2.4}$$

2.7.2. Surface area of exploded features per unit volume

The basic equation for obtaining the area of surfaces in a volume is

$$S_V = 2P_L \qquad \text{eqn. 2.5}$$

which was derived by Saltykov in 1945 and latter by Smith and Guttman in 1953 [35]. In the above equation, P_L denotes the number of intersection point between the randomly selected test lines and the boundaries of the concerned phase on a section plane. This equation applies to systems of surfaces with any configuration. It is valid for systems of discontinuous, separated or bounded surfaces. The value of S_V depends on the following three parameters:

(I)   Amount of the feature: S_V increases as the amount of the feature increases, provided the size and shape of the feature are same.

(II)   Size of the feature: S_V decreases as the size of the feature increases, provided the amount and shape of the feature are same.

(III)   Shape of the feature: S_V increases as the shape of the feature becomes more acicular, provided the size and amount of the feature are same.

2.7.3. Contiguity of different phases

The contiguity ratio, *i.e.* the degree of contact, can exert a significant influence on the properties of a structure. For example, the optimum spacing of fissionable particles in dispersion-type reactor fuels, the stress distributions in particle strengthened alloys, the susceptibility to crack propagation in a brittle second phase depend to some extent on the contacts between specific microstructural volume elements. Gurland defines the contiguity C as the fraction of the total interface area of a phase that is shared by particles of the same phase [38]. For a homogenous three-phase structure of α, β and γ, the contiguity of α-phase is given by

$$(C)_\alpha = \frac{2(S_V)_{\alpha\alpha}}{2(S_V)_{\alpha\alpha} + (S_V)_{\alpha\beta} + (S_V)_{\beta\gamma} + (S_V)_{\gamma\alpha}}, \qquad \text{eqn. 2.6}$$

where $(S_V)_{\alpha\alpha}$, $(S_V)_{\alpha\beta}$, $(S_V)_{\beta\gamma}$ and $(S_V)_{\gamma\alpha}$ are the interface areas per unit volume between α-α and α-β, β-γ and γ-α phases, respectively. In this case surface shared by two α-particles are counted twice. Now, Eqn (2) states that $S_V = 2P_L$, so

$$(C)_\alpha = \frac{4(P_L)_{\alpha\alpha}}{4(P_L)_{\alpha\alpha} + 2(P_L)_{\alpha\beta} + 2(P_L)_{\beta\gamma} + 2(P_L)_{\gamma\alpha}}, \qquad \text{eqn. 2.7}$$

where $(P_L)_{\alpha\alpha}$ is the number of intersections of the interface between α grains with a random line of unit length and $(P_L)_{\alpha\beta}$, $(P_L)_{\beta\gamma}$ and $(P_L)_{\gamma\alpha}$ are the average number of intersections that unit length of a random test line makes with elements of interface between α, β; β, γ; and α, γ phases, respectively. The ratio varies from 0 to 1 as the

distribution of the phase changes from a complete dispersed to a fully agglomerated structure. These equations are valid for any distribution of particle sizes and shapes [40].

2.7.4. Size or the mean intercept length of the different features

When the bulk properties of an aggregate containing grains, cells, or particles, it appears that some average distance across these randomly oriented volume elements is the important quantity, rather than a maximum dimension. Such an average distance is called the mean intercept length $(\overline{L}_3)$ of those space-filling volume elements. The $\overline{L}_3$ is defined for a single particle as

$$\overline{L}_3 = \frac{1}{N}\sum_{i}^{N}(L_3)_i,$$

<div align="right">eqn. 2.8</div>

Where the subscript 3 refers to the dimensionality of the particle, and the $(L_3)_i$ are the intercepted lengths from N random penetrations of the particle by a straight test line. This definition allows for the possibility of a particle-s being intercepted more than once by a single penetration of the test line. Thus this equation is applicable to concave bodies as well as convex one. From Eqn. 2.5 it can be derived that for a phase α

$$\left(\overline{L}_3\right)_\alpha = 4\frac{(V_V)_\alpha}{(S_V)_\alpha}.$$

<div align="right">eqn 2.9</div>

It has been observed that, $\overline{L}_3$ has a unique value, regardless of convexity or concavity, since both $(V_V)_\alpha$ and $(S_V)_\alpha$ are fixed quantities for any given system of particles, independent of particle shape [38].

2.7.5. Number density in 2D

Number density in 2D (N_A) of a feature is defined as the number of interceptions of features per unit area of the test plane of polish. This quantity is measured by counting the number of features divided by the total area of the field of view. In this process proper care should be taken during counting the number of features. Two categories of N_A measurements are important. In one case, the features to be counted are space filling and

$\overline{V}_V = 1$. In the other case, the features are not space filling, and $\overline{V}_V < 1$. In both the cases, the procedure stated below can be applied. If N_w number of features are lying wholly within a selected area A, and N_I number of features are intercepted by the area perimeter, then the total number of features in that field of view is calculated as

$$N_T = N_w + \frac{1}{2}N_I.$$

eqn. 2.10

Finally, the number density of a phase α in 2D can be defined as

$$\left(N_A\right)_\alpha = \frac{\left(N_T\right)_\alpha}{A} \text{ [38].}$$

eqn. 2.11

2.7.6. Probability of occurrence of features

For a structure having second phase particles, the second phase particles can be observed inside the grains of the matrix, between two grains of the matrix, and at the triple points of the grain boundaries of the matrix. The probability of occurrence of the second phase particles on the different location can be calculated by counting the number of second phase particles on the concerned location divided by the total number of that second phase particle in that field of view. So the probability of occurrence of a second phase particle α on the type of location 'l' can be defined as

$$\left(p_\alpha\right)_l = \frac{\left(N_\alpha\right)_l}{\left(N_T\right)_\alpha},$$

eqn. 2.12

where $\left(N_\alpha\right)_l$ = The number of second phase particles on the location 'l' and

$\left(N_T\right)_\alpha$ = The total number of second phase particles in the field of view.

2.7.7. Total edge length in a unit volume

The basic equation for obtaining the total edge length of features per unit volume (L_V) is as follows;

$$L_V = 2P_A;$$

eqn. 2.13

which was derived by Saltykov [37, 38] and Smith and Guttman [38, 40]. P_A is the number of intersection points of the concerned feature with the random test lines in a field of view. This equation is valid for all the system of lines in space consists of straight, curved, continuous or broken lines, oriented and located randomly throughout a certain volume, provided that all angles of intersection between lines and test planes are equally possible [38].

2.7.8. The estimation of statistical error

Stereological methods are statistical in nature and the measurements obtained by these methods are statistical in nature and are affected by sampling error. In this regard Central Limit Theorem is very useful. This fundamental theorem is a very powerful tool in statistical analysis in that it provides complete knowledge about the distribution of a random sample from any population.

Let x be some random variable that has an arbitrary distribution with mean μ_x and standard deviation σ_x Let a random sample consisting of n readings of the variable x be obtained from the population. The mean value of this sample ($\bar{x}$) can take on any value in the range of x, although the values tend to cluster about the mean of the population μ_x. Thus, the average value of a random sample of size n can itself be considered as a random variable that possesses a characteristic distribution function, mean and standard deviation. It can be shown that the theoretical mean value (expected value) of this random variable coincides with the mean of the population divided by the square root of the number of readings in the sample,

$$\mu_{\bar{x}} = \mu_x$$
eqn. 2.14

$$\sigma_{\bar{x}} = \frac{\sigma_x}{\sqrt{n}}$$
eqn. 2.15

In short, the Central Limit Theorem states that the distribution of the mean value of random sample of size n from an arbitrary population approaches to a normal distribution of mean μ_x and standard deviation to $\sigma_x / \sqrt{n}$ as sample size n increases. The mean of the sample is given by

$$\bar{x} = \frac{\Sigma x}{n}$$
eqn. 2.16

and the variance is given by

$$V_x = \frac{\sum(x-\bar{x})^2}{n-1}$$ eqn. 2.17

The standard deviation can be determined from the following equation

$$\sigma_x = \sqrt{V_x} \,.$$ eqn. 2.18

Therefore, the standard error of the mean i.e. the standard deviation of the mean can be represented as

$$\sigma_{\bar{x}} = \frac{\sigma_x}{\sqrt{n}} = \left(\frac{\sum(x-\bar{x})^2}{n(n-1)}\right)^{1/2}.$$ eqn. 2.19

According to statistical theory, there is a 65% probability that the mean $\bar{x}$ will fall between the limits $\bar{x} \pm \sigma_{\bar{x}}$, and a 95% probability that the mean will fall in the range $\bar{x} \pm 2\sigma_{\bar{x}}$ [38, 40].

2.8. Electrochemical corrosion

Corrosion can be defined as the degradation of a metal by an electrochemical reaction with its environment [39]. All metals are found in their low energy state ores, in the form of their oxides, sulfides, carbonates or more complex compounds. Large amount of energy is supplied in order to extract a pure metal from its ore. This pure metal is a high-energy state of the metal and hence they try to come back to the low energy state by recombining with the environment. This process is called corrosion. Figure 2.20 shows the thermodynamic energy profile for metals and their compounds. The thermodynamic aspects of corrosion will be briefly discussed. All the interactions between elements and compounds are governed by the free energy changes (ΔG). Any reaction is said to be spontaneous when ΔG for the reaction is negative. At room temperature most of the chemical compounds of metals have lower free energy than the pure metals and hence most of the metals have an inherent tendency to corrode.

In all kinds of aqueous corrosion, there are two reactions occurring at the metal/liquid interface; an electron producing reaction (anodic or oxidation reaction) and an electron consuming reaction (cathodic or reduction reaction). The corrosion reaction

for the creation of a wet electrochemical cell requires four basic requirements, the cathode on which the reduction reaction occurs, an anode on which oxidation occurs, an electrolyte to act as the conducting medium for ions and a electrical connection for electron to flow between the anode and cathode. The anodic reaction is invariably corrosion of the metal as shown in Eqn. 2.21. Several cathodic reactions can occur during corrosion [43]. The simplest of them is reduction of hydrogen ions (Eqn. 2.22). Another is reduction of an oxidized ion in solution (redox reaction) as in Eqn. 2.23. Another reaction is reduction of dissolved oxygen as in Eqn. 2.24. In the absence of any of these reactions water reduction will occur as in Eqn. 2.25.

$$M \Rightarrow M^{n+} + ne^- \qquad \text{(Anodic Reaction)} \qquad \text{eqn. 2.20}$$

$$2H^+ + 2e^- \Rightarrow H_2 \qquad \text{(Hydrogen Reduction Reaction)} \qquad \text{eqn. 2.21}$$

$$Fe^{3+} + e^- \Rightarrow Fe^{2+} \qquad \text{(Redox Reaction)} \qquad \text{eqn. 2.22}$$

$$O_2 + 4H^+ + 4e^- \Rightarrow 2H_2O \qquad \text{(Oxygen Reduction Reaction)} \qquad \text{eqn. 2.23}$$

$$2H_2O + 2e^- \Rightarrow H_2 + 2OH^- \qquad \text{(Water Reduction Reaction)} \qquad \text{eqn. 2.24}$$
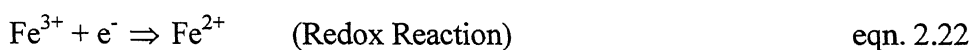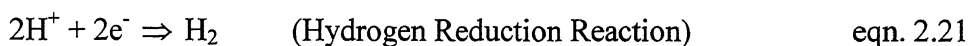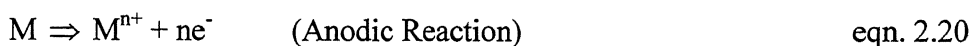
A basic wet corrosion cell is shown in the Figure 2.21. The potential difference between the anode and the cathode could be measured by using a voltmeter in the circuit. But this gives only the potential difference between the electrodes and in order to measure the absolute potential we need a third electrode. This third electrode is called as the standard electrode against which all the measurements can be made. The standard hydrogen electrode, saturated calomel electrode (SCE), etc. are usually used as the standard electrodes. The Table 2.3 gives some commonly used standard electrodes and their potentials.

Table 2.3   Galvanic series of various metals and alloys in seawater [41]

Active

Magnesium alloys

Zinc

Aluminum and aluminum alloys

Mild steel

Wrought iron

Cast iron

13% Chromium stainless steel, type 410 (active)

Lead-tin solders (50-50)

18-8 Stainless steel, type 304 (active)

18-8, 3% Mo stainless steel, type 316 (active)

Lead

Tin

Nickel (active)

Aluminum bronze

Red brass

Copper

Silicon bronze

70Cu-30Ni

Nickel (passive)

70Ni-30Cu (Monel)

Titanium

18-8 Stainless steel, type 404 (passive)

18-8, 3% Mo stainless steel, type 316 (passive)   ▼

Noble

2.8.1. Polarization

When a metal is not in equilibrium with the solution of ions, the electrode potential differs from the free corrosion potential by an amount known as the polarization [42]. It can also be said as over-potential or over-voltage. Polarization is a very important corrosion parameter as it is useful in calculating the rates of the corrosion process. The deviation of the equilibrium potential is a combination of an anodic polarization of metal and a cathodic polarization of the environment. If the electrons are made available as in equation 13, the potentials at the surface becomes more negative, suggesting that excess electrons with their negative charges accumulate at the metal/solution interface waiting for the reaction. This negative potential charge is called as cathodic polarization. Similarly, there will be a deficiency of electrons on the metal surface interface by the reaction shown in equation 2.21, which produces a positive potential change called anodic polarization [43]. In an aqueous electrolyte solution the surface will reach a steady potential, E_{corr}, which depends on the ability and rate at which electrons can be exchanged by the anodic and cathodic reactions. When the surface potential increases above the E_{corr} value, to a value E, then the anodic polarization is given by the difference between E and E_{corr}. At equilibrium the forward anodic reaction, i_a is equal to the reverse cathodic reaction, i_c. Hence the rate of the reaction can be given by,

$$i_a = i_c = i_o = A_o \exp[-\Delta G/RT] \qquad \text{eqn. 2.25}$$

There are two methods available for measurement of corrosion rate using polarization methods, namely Tafel extrapolation and polarization resistance. The polarization methods to measure corrosion rates have their inherent advantages. The main advantage of these methods is that the time taken for conducting experiments is relatively short, whereas the conventional weight loss methods require several days. The polarization methods are highly sensitive, and accelerating factors such as elevated temperature, to increase rates is generally not necessary. Moreover these methods are non-destructive and several repetition experiments can be carried out using the same sample.

The mixed potential theory forms a basic for explaining the polarization techniques. The mixed potential theory consists of two simple hypotheses:

1. Any electrochemical reaction can be divided into two or more partial oxidation and reduction reactions.

2. There cannot be net accumulation of electrical charge during an chemical reaction i.e., corrosion reaction the sum of the anodic oxidation currents should be equal to the sum of the cathodic reduction currents. In other words the total rate of oxidation should be equal to total rate of reduction [45].

Consider the reactions for zinc getting corroded in an acid solution. Then the anodic and cathodic reactions are given by,

$$Zn \Rightarrow Zn^{2+} + 2e^-$$ (Anodic reaction)   eqn. 2.26

$$2H^+ + 2e \Rightarrow H_2$$ (Cathodic reaction)   eqn. 2.27
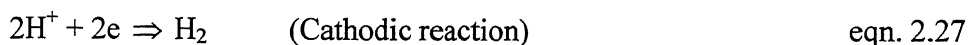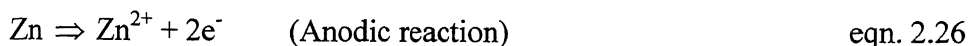
These reactions are called as the half-cell reactions and the potential corresponding to them are called cell potential. The potentials cannot coexist separately on an electrically conducting surface. The potentials will polarize to an intermediate value called as the corrosion potential or mixed potential (E_{corr}). When there is no external current flowing into the system, then the equilibrium potential attained is called open current potential (OCP) or free corrosion potential (E_{corr}). As the reactions polarize on the same surface the change in potentials is given by,

$$\eta_a = \beta_a \log (i_a/i_o)$$ Eqn. 2.28

$$\eta_c = \beta_c \log (i_c/i_o)$$ Eqn. 2.29

where η_a and η_c are anodic and cathodic polarization, β_a and β_c are the Tafel constants, I_a and i_c are the anodic and cathodic currents respectively. At E_{corr} the rate of anodic and cathodic reactions are equal and is equal to the current density, i_{corr}. The half-cell reactions for dissolution of Zn in acid are shown in the Figure 2.22 [42]. This figure is called as Evans diagram and represents an active material.

The various polarization techniques that are commonly used are linear polarization, Tafel extrapolation, potentiodynamic polarization and cyclic polarization. These polarization techniques are summarized in the Figure 2.23 [46].

Free
energy

Metal ⌐----------⌐ $\Delta G^{\ddagger}$
              └----------┘

ΔG

Corrosion
Ore   product

Reaction co-ordinate ►
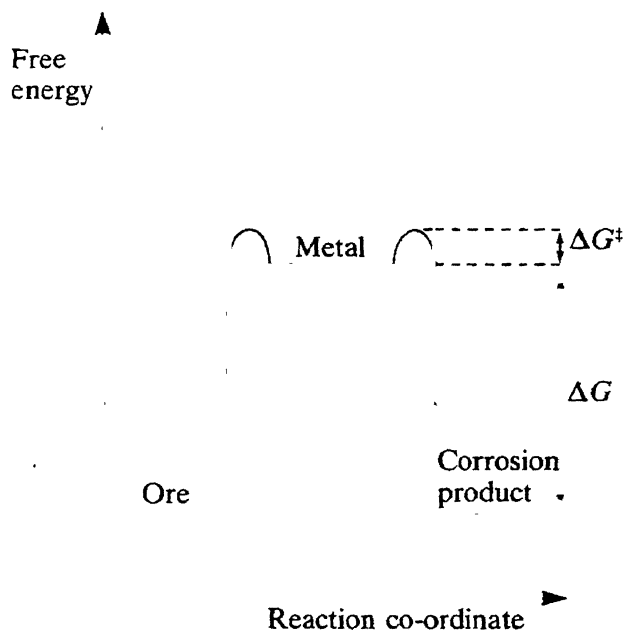
Figure 2.20   Thermodynamic energy profile for metals and their compounds
               [39].

(d) Electrical
    connection

(a) Anode ►

(b) Cathode ◄
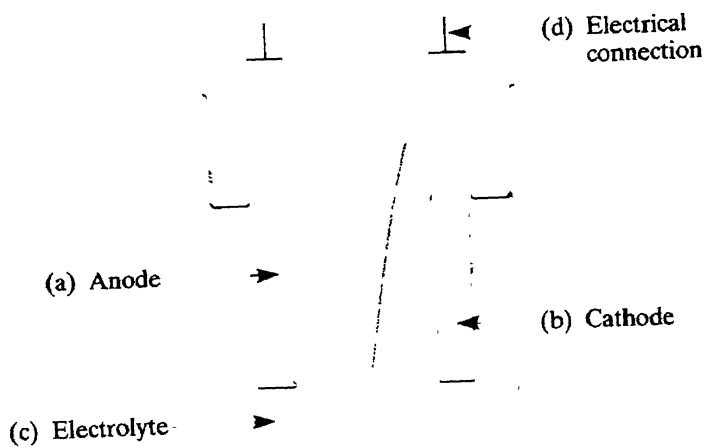
(c) Electrolyte ►

Figure 2.21   Basic wet corrosion cell [39].

Table 2.4 Standard reference electrode potentials [40].

Electrode	Electrolyte	Potential (V)
Calomel (SCE)	Saturated KCl	+0.2420
Calomel (NCE)	1.0 M KCl	+0.2810
Calomel	0.1 M KCl	+0.3335
Silver/Silver Chloride (SSC)	1.0M KCl	+0.2224
SSC	Sea water	+0.25 (approx)
Copper/Copper sulfate (CSE) Sea water		+0.30 (approx)
Zinc	Sea water	-0.79
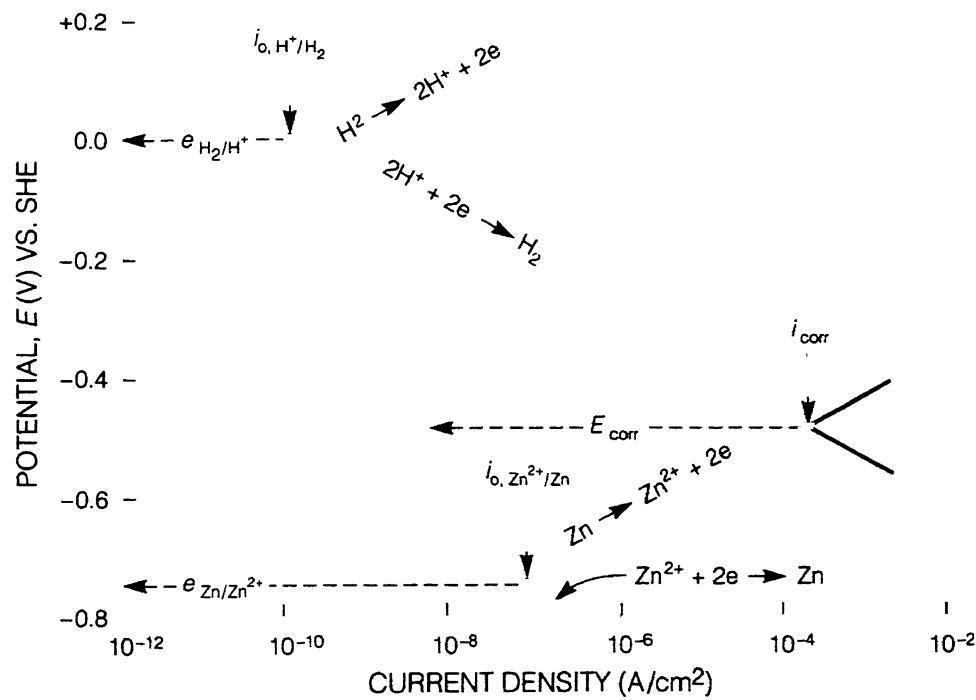
Figure 2.22   Evans diagram for an active metal (Zn) [40].
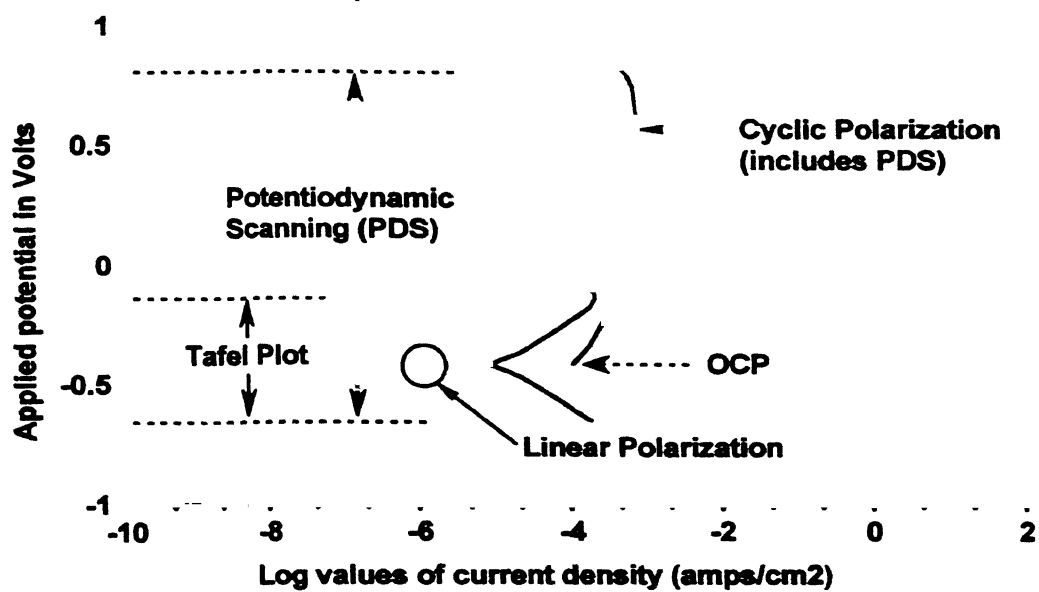
Figure 2.23   Various types of polarization methods [43].

2.8.1.1. *Potentiodynamic Polarization*

The potentiodynamic polarization is carried out in a wider range of potential spectrum and gives much more details about the samples response to the environment. The potentiodynamic polarization provides data about the metal behavior i.e., whether the metal is active or passive or active passive in the given environment. The plot elucidates the properties of the passive film and the effect of inhibitors on the corrosion behavior of the metal. Depending upon the nature of potentiodynamic polarization curve, alloys can be divided into active alloys and active-passive alloys. For an active metal the corrosion rate increases linearly with increase in the anodic polarization potential. This is due to the non-protective oxide layer, which forms on the metal surface. For an active passive metal the corrosion rate increases with polarization potential up to a critical current density, (i_{crit}) after which it falls down rapidly due to the formation of a protective passive film.

A typical potentiodynamic polarization plot is shown in Figure 2.24 for an active passive metal [44]. The figure shows the various regions of a potentiodynamic plot for an active-passive metal. The first two regions are the normal cathodic and anodic polarization regions that were discussed for the Tafel plot. The anodic region is widened to show the passive film formation. The anodic region can be subdivided into three main regions namely, the active region, the passive region and the trans-passive region. The active region and the cathodic curve can be extrapolated to extract the values of E_{corr} and i_{corr}. The active region ends at the primary passivation potential (E_{pp}) at which the passive film becomes stable and the corrosion rate falls rapidly. The current corresponding to this value is called as critical current density (i_{crit}). As the potential is increased beyond this value, the current density decreases until it reaches a steady current called as the passive current density (i_{pass}). The range over which the steady current is maintained is known as the passive range and it relates to the stability of the passive film. As the potential is increased further the passive layer breaks down and the anodic rate increases in the transpassive region. This breakdown in passivity can be attributed to the oxygen evolution or due to localized mechanisms such as pitting. In certain kind of alloys like stainless steel, there will be an additional region showing secondary passivity. This results due to the formation of some secondary oxide layer, which ultimately breaks leading to increase in the corrosion rate. The potential at which the passive film breaks is

60

known as pitting potential (E_{pitt}) and the potential at which the oxide film completely breaks apart and is called the breakdown potential (E_{break}).

The schematic diagram in Figure 2.25 shows the type of alloy that can be used depending upon the nature of the environment. The figure shows four types of alloys and three environments that are commonly used. For a reducing atmosphere, as in 1, either the non-passivating alloy A or the partially passivating alloy B is superior because they have better corrosion resistance in the active conditions. The alloys C and D produces strong passivity and hence alloying elements like chromium should be added. This makes the alloys more expensive and thus unjustifiable for the service condition [43]. For a moderately oxidizing atmosphere, number 2, the alloy C would be recommended because the reduction curve exceeds the critical current density and it is the only alloy showing stable passivity. In alloy B, the reduction curve exceeds critical current density, but the passive region is not broad enough to ensure good passive resistance. Alloy D is in a state of borderline passivity, with both active and passive states possible. For strong oxidizing condition in 3, alloy D is recommended as the reduction curve exceeds critical current density and the corrosion rate is low. In alloy C, the passivity breaks in this condition and it is in the transpassive region. Alloys A and B are not resistant to high oxidizing conditions.

The main limitation of potentiodynamic polarization that the sample surface gets disturbed after the experiment is completed. Hence the test can be conducted only once at a time. Moreover the exact corrosion rate cannot be predicted accurately by this method.
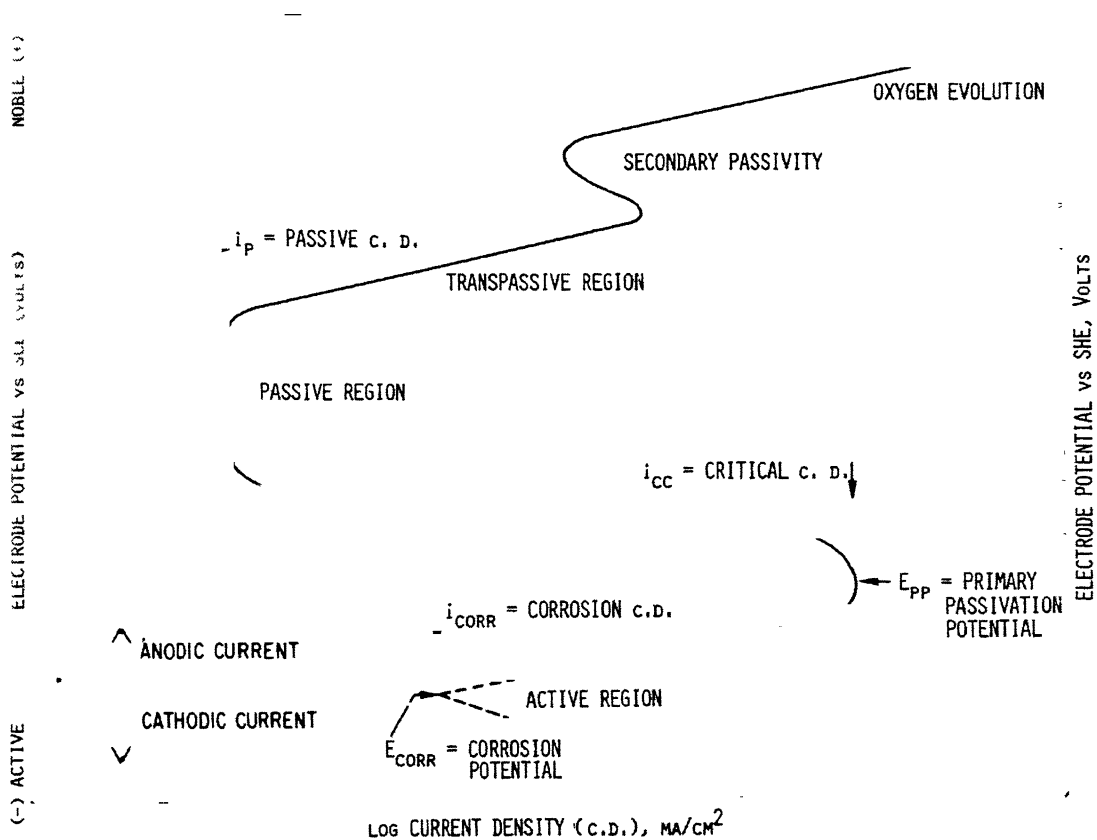
Figure 2.24   Schematic diagram showing the potentiodynamic polarization for an active-passive metal [47].
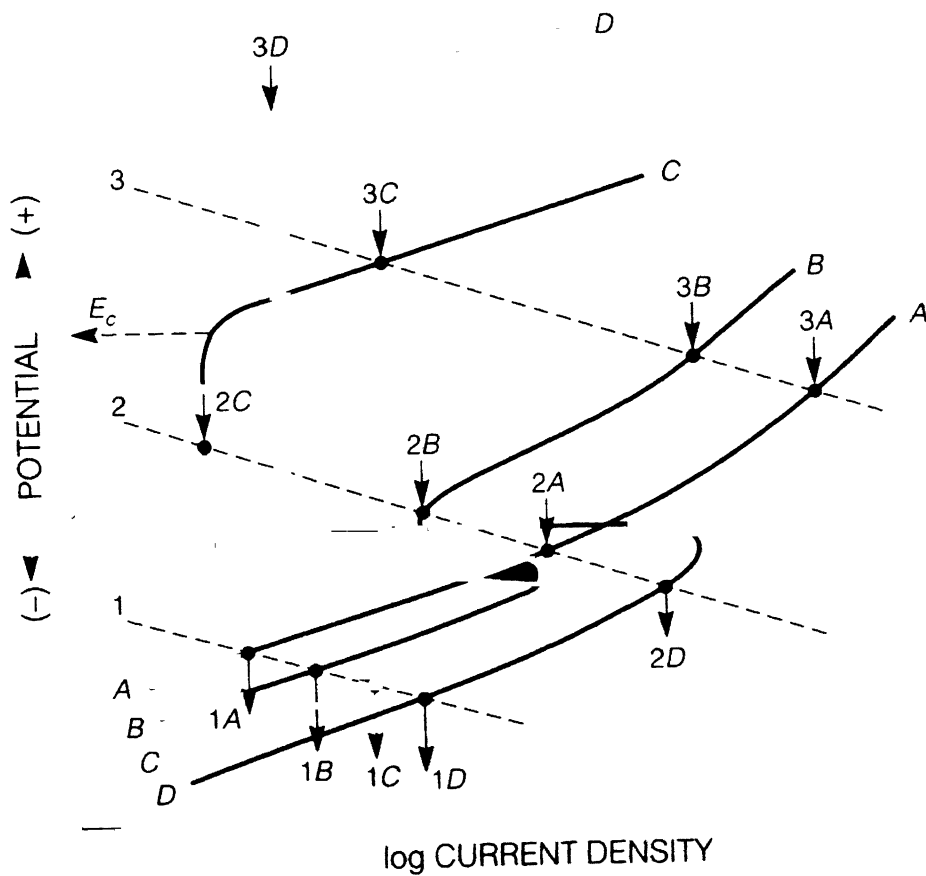
Figure 2.25   Anodic polarization curves for hypothetical alloy A, B, C and D in (1) reducing, (2) moderately oxidizing and (3) highly oxidizing environments [43].

CHAPTER 3

EXPERIMENTAL PROCEDURE

The aim of the present work is to understand the microstructural aspects of hydrogen attack in carbon alloyed iron aluminides. This involved hydrogen treatment of the material at different temperatures for different times, microstructural characterization, mechanical behavior assessment and electrochemical characterization. Hydrogen treatment was performed in a tube furnace. Stereological methods were applied to analyze the microstructural aspects. The mechanical behavior was investigated by microhardness testing. The potentiodynamic polarization behaviour was studied to understand dissolved hydrogen in the materials, prior to and after the high temperature hydrogen treatment.

3.1. Raw materials

The carbon alloyed iron aluminides were obtained from Defense Metallurgical Research Laboratory (DMRL), Hyderabad, India. Their composition (in at %) were Fe-28.1Al-2.1C (ESR56) and Fe-27.46Al-3.66C (ESR63). In terms of wt %, the compositions were Fe-16.2Al-0.54C (ESR56) and Fe-16.0Al-0.9C (ESR63). The ESR stands for electro slag remelted specimens and these marked materials were obtained from DMRL, Hyderabad, in the form of metal strips of dimension 120 mm × 57mm × 3.01mm and 110mm × 95mm × 2.97mm for ESR56 and ESR63, respectively. The processing technique utilized to obtain these strips was as follow [43].

Iron aluminide ingots containing about 15.5 wt % Al (28 at %) were prepared by air induction melting (AIM) and chill cast into cast iron moulds. Commercial purity aluminium and mild steel scrap were used as raw materials. Grinding was used to clean the surface of the iron charge. After melting, the slag product was skimmed off. Aluminium pieces were then added to the molten iron bath. The melt was held at 1620° C for a very short time (2 minutes) to prevent aluminium losses and then normalized to room temperature. The ingots were then tested for their soundness by radiography. These AIM ingots (55 mm diameter, 360 mm long) were machined to 50 mm diameter. They

were refined in an ESR furnace of 350 kVA capacity. A commercial prefused flux based on CaF_2 was used. The flux was preheated and held at 850°C for 2 hours before use in order to remove moisture. The iron aluminide electrode was remelted under this flux cover and cast into 76 mm ingot in a water cooled steel mould. At the end of the process, the power supply was gradually reduced to impose a condition of hot topping. To check their soundness, the ESR ingots were also radiographed. The ingots were then forged to a reduction ratio of 70% and after forging they exhibited recrystallized grains [43].

3.2. Hydrogen attack

3.2.1. Sample preparation

Rectangular specimens were cut from the bulk alloy samples by using a diamond cutter (Buehler-ISOMET). The specimen size could not be maintained to a standard uniform size due to the limited amount of available specimen. The specimen length varied from 7.80 mm to 7.36 mm while their breadth varied from 4.52 mm to 5.70 mm. The thickness of the specimen varied from 2.58 mm to 2.78 mm. All the surface of the specimens, after cutting, were mechanically polished in fine cloth using 0.5μ alumina powder and then degreased using acetone before being used for each experiment.

3.2.2. Apparatus for hydrogen attack experiments

The apparatus consisted of a tube furnace, a hydrogen gas cylinder, a argon gas cylinder, a gas pressure controller and a gas train. The furnace and the gas train are described in detail below. Figure 3.1 shows the schematic of the experimental set-up employed for the present investigation and Figure 3.2 shows the actual experimental set-up employed for the present experimental investigation.

Furnace with accessories

A vertical tube furnace of 150 mm length was employed to carry out the hydrogen treatment of the samples. The temperature of the furnace was controlled within ±2K by an ON-OFF type temperature controller (Toshniwal Instrument Pvt. Ltd., India), actuated by a Pt/Pt-10%RH thermocouple. The thermocouple EMF was measured by a four-digit

3

4   5   6

2

7
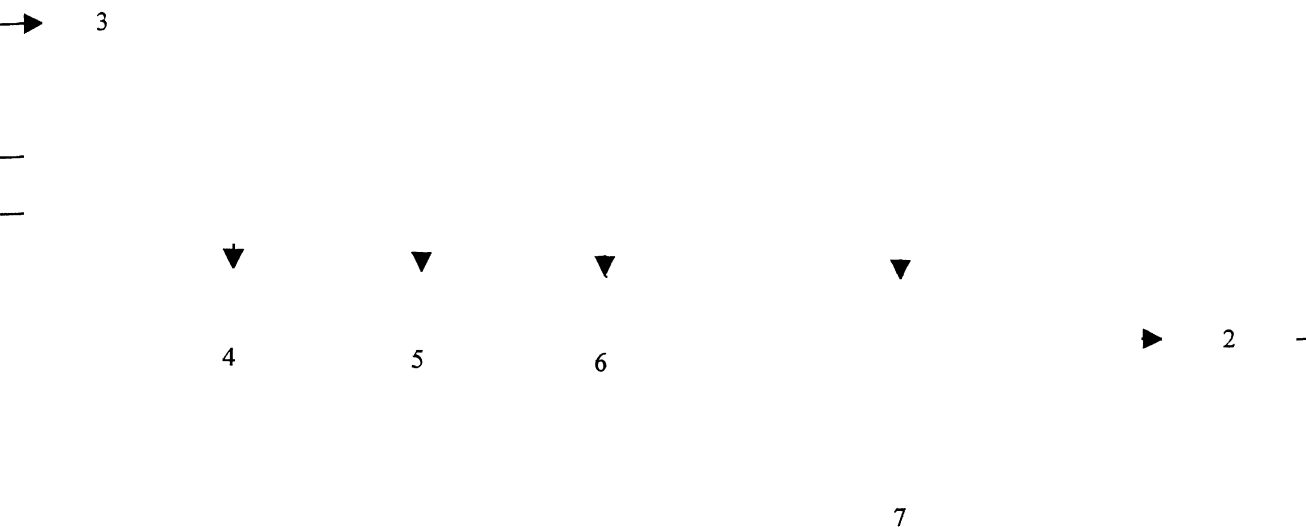
1. Gas cylinder   2. Two-stage gas regulator   3. Gas bubbler

4. Ascarite column   5. Anhydrous $CaCl_2$ column   6. Drierite column

7. Furnace

Figure 3.1   Schematic of the experimental set-up for the hydrogen treatment

Figure 3.2   Experimental set-up employed for the hydrogen treatment

millivolt-meter (SONIT, Type SE-402-4). A mullite tube (45 mm inner diameter and 460 mm length) acted as the reaction chamber. The mullite tube was fitted with silicone rubber stopper at the top to provide airtight fitting covers. Gas inlet tube and outlet tubes were inserted through the top of the reaction chamber through the silicone rubber stopper. All these tubes were glass fitted with rubber tubing and sealed with sealant. Teflon tapes were tightly wound on the locations where the glass tubes were fitted with the rubber tubes to avoid the leakage of hydrogen gas from the connections. Temperature profiling of the furnace showed that a constant temperature zone of about 25 to 30 mm was obtained in the central region of the furnace. The specimen was placed inside a quartz crucible with three holes at the bottom to allow easy passage of gas. This crucible was then hung from the top of the furnace using a steel wire into the reaction zone of the reaction chamber.

Gas train

The purpose of the gas train was to monitor the flow rates of the gas and purify it from probable impurities present. Pure gas was passed through a bubbler and capillary flow meter. The gas was then passed through Ascarite column (sodium hydroxide coated silica) to remove carbon dioxide. It was passed through anhydrous calcium chloride and Drierite ($CaSO_4$) columns successively before introduction into the reaction chamber. Drierite possesses low equilibrium residual water vapour pressure and therefore, it was used after the anhydrous calcium chloride column in the gas train for efficient removal of moisture. The outlet gas was passed out of the furnace through a bubbler to ensure that the flow of gas was being maintained through the system.

3.2.3. Experimental approach

The above-mentioned apparatus was used to study hydrogen attack on carbon-alloyed iron aluminides in five different conditions changing the treatment temperature and time. The different conditions are

(I)   700°C and 10 hours

(II)   700°C and 48 hours

(III)   900°C and 144 hours

(IV)   900°C and 336 hours and

(V)   900°C and 720 hours

The 3rd experiment (at 900°C for 6 days) was repeated for understanding the effect of duplicate hydrogen treatment on the samples.

The experiments were carried out isothermally. Once the furnace attained the test temperature, sufficient time (15 to 20 minutes) was allowed for temperature to stabilize. The furnace was then first flooded with argon gas for 10 minutes to remove all entrapped air and then again hydrogen gas was flowed in reaction chamber to remove the argon gas and to maintain the reaction environment condition inside the furnace before introduction of the sample.

The samples with freshly prepared surfaces (by fine cloth polishing by using 0.5 μ alumina powder) for hydrogen treatment were weighed in an analytical balance (Anamed, MX 7301A, India). The reading in this balance could be taken up to six places of decimal (in grams). The samples were then placed inside the quartz crucible, which was introduced into the reaction chamber by suspending by means of crucible through a steel wire. The hydrogen gas pressure was maintained at one atmospheric pressure. The whole system was maintained airtight (in order to prevent the entry of the atmospheric air) by tightening the silicone rubber stopper on the top of the mullite chamber. The flow of gas at the outlet ensured the hydrogen flow in the furnace. The sample and furnace temperature were allowed to equalize for a short time (2 to 3 minutes) before the timing of the experiment was begun.

The quartz crucible was taken out from the furnace at the pre-determined time interval. The furnace with the sample was allowed to cool to room temperature to avoid oxidation of the samples in atmosphere at high temperature, before the samples were taken out form the furnace. The inlet hydrogen was stopped only after the temperature of the reaction zone was lowered down to room temperature. The crucible with the sample inside was then taken out from the furnace. The weight of the samples was recorded using a single pan analytical balance. The samples were then utilized for microstructural

characterization and for measurement of microhardness, allowing a minimum time for the diffusion of reversibly trapped hydrogen gas to out of the samples.

3.3. Microhardness measurement

Microhardness measurements of both the phases, i.e. carbide and matrix, of all the samples were performed prior to and after the hydrogen treatment using a microhardness tester (Carl Zeiss, Jena, Jenavert, Germany) attached with an optical microscope. A diamond pyramid indentor with a 50-gram load was employed. Observations were made at a magnification of 500X. Thirty fields of view were chosen for each sample. All the values ware noted as Vickers hardness number (VHN) which was obtained from the formula written below;

$$VHN = 1854.4 * P/d^2 \ (Kg \ mm^{-2}), \qquad\qquad Eqn. \ 3.1$$

where 'P' is the load in grams and 'd' is the average of the two diagonals of indentation mark in micrometer.

3.4. Microstructural characterization

Standard metallographic techniques used for preparation of the samples were sectioning, mounting, grinding and polishing. A diamond wheel was used for sectioning the specimens. The diamond wheel was operated at a relatively slow speed in order to avoid any damage of the sample and the cutter. The specimens were hot mounted. Care was taken while mounting to maintain the flatness of the sample and the mount. Grinding of the sample was performed in a series of emery papers staring from coarse grit to fine grit. The sample was ground carefully to avoid higher relief of the softer matrix than the hard carbides. Polishing was performed by using 0.5 μm alumina powder. For revealing the microstructures, an etchant of composition (volumetric) 33% acetic acid (CH_3COOH), 33% nitric acid (HNO_3), 33%water (H_2O) and 1% hydrofluoric acid (HF) was used [45]. Optimum etching time was determined as 5 seconds after several trials.

The microstructures were recorded using an optical microscope (Axiolab A, Zeiss, Germany), attached with a digital camera (CE, Japan). They were later analyzed by the image-analysis program (Image-Pro Plus, version 4.1, Media Cybernetics, USA).

3.4.1. Measurement of the parameters

Volume fraction

In order to calculate the V_V of the spherically shaped carbides, a 6X6 grid was used and the sample was observed at 100X. In the case of the needle-shaped carbides present in the material, a 10X10 grid was used and the sample was observed a 200X. A higher magnification with higher number of total point grid was used because the volume fraction of disc shaped particles was very low. The number of points falling in the feature of interest was calculated manually and divided by the total number of points. The result provided the volume fraction.

In order to calculate the other parameters, five test lines of equal length at equal spacing were utilized. And then the following points were counted for 100 fields of view:

(i) n_{01}: The total number of intersection points between the test lines and the grain boundaries,

(ii) n_{02}: The total number of intersection points between the test lines and the partition line of grains and carbides,

(iii) n_{03}: The total number of intersection points between the test lines and the partition line of carbides ,

(iv) n_{04}: The total number of intersection points between the test lines and the partition line of grains and the particles,

(v) n_{05}: The total number of intersection points between the test lines and the partition line of carbides and particles,

(vi) n_{06}: The total number of intersection points between the test lines and the partition line of particles,

(vii) n_{07}: The total number of intersection points between the test lines and the grain boundaries which were hidden by carbides,

(viii) n_{08}: The total number of intersection points between the test lines and the grain boundaries which were hidden by particles,

(ix) n_{09}: Total number of carbides in each field of view,

(x) n_{10}: Total number of particles in each field of view,

(xi) n_{11}: Total number of carbides on the grain boundaries in each field of view,

(xii) n_{12}: Total number of particles on the grain boundaries in each field of view.

(xiii) n_{13}: Total number of grains in each field of view.

(xiv) n_{14}: Total number of triple points hidden by the carbides in each field of view.

(xv) n_{15}: Total number of triple points hidden by the particles in each field of view.

(xvi) n_{16}: Total number of unhidden triple points in each field of view.

Two typical microstructure (Fig. 3.3) of as-received Fe-16.2Al-0.54C alloy were analyzed in order to explain the procedures above. The results are tabulated in Table 3.1. In this figure 3.3, the imposed random test lines are shown. The dashed lines represent the hidden grain boundaries and partition lines between the carbide-carbide, carbide-particle and particle-particle.
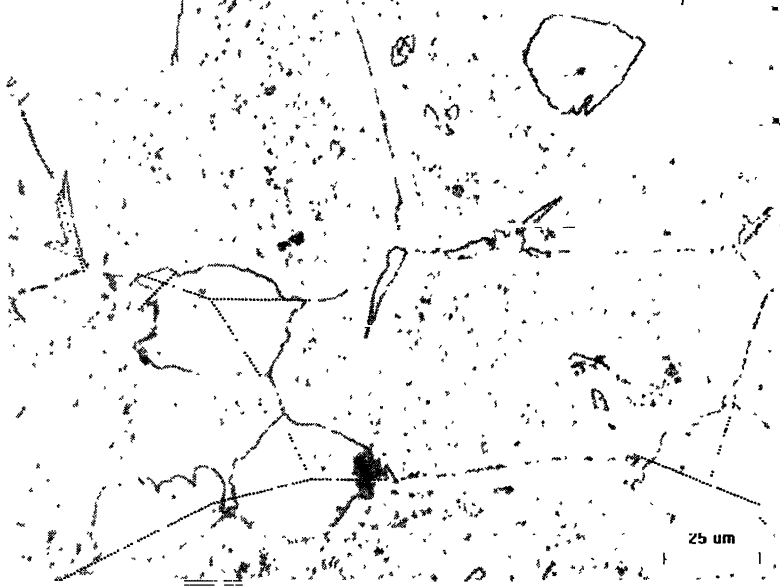
(a)
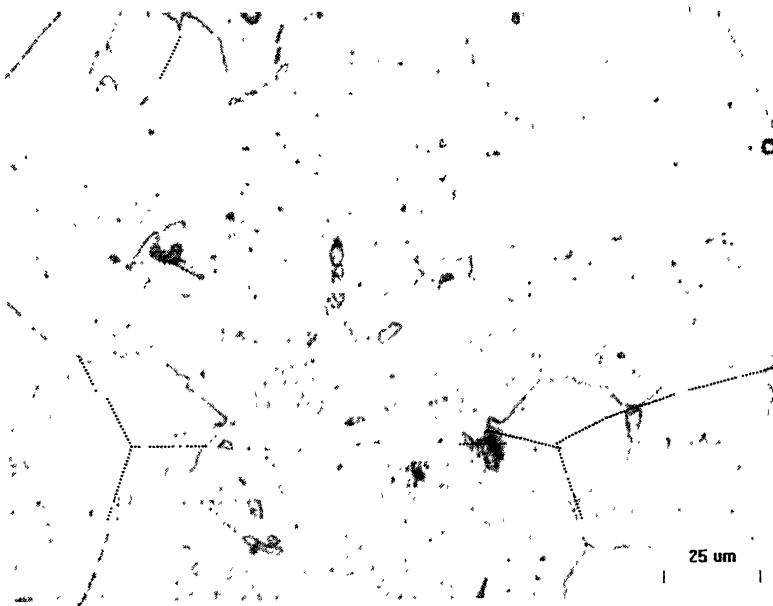
(b)

Figure 3.3   Optical micrographs of Fe-16.2%Al-0.54%C (wt%) showing the imposed
random test lines where the dashed lines represent the hidden grain
boundaries and partition lines between the carbide-carbide, carbide-
particle and particle-particle

Table 3.1   The points counted to calculate different parameters

Figure	n_{01}	n_{02}	n_{03}	n_{04}	n_{05}	n_{06}	n_{07}	n_{08}	n_{09}	n_{10}	n_{11}	n_{12}	n_{13}	n_{14}	n_{15}	n_{16}
Fig 3.3a	4	6	0	17	0	2	4	2	5	23	4	11	4	3	3	0
Fig 3.3b	1.5	1.5	1	8	1	0	4	1	5	24	3	6	3	2	0	0

Surface area of exploded features per unit volume

Surface areas of exploded grains, carbides, and particles per unit volume were calculated by using the Eqn. 2.2.

Surface areas of exploded grains $(S_V)_G = \dfrac{2(2n_{01} + 2n_{07} + 2n_{08})}{L}$,

Surface areas of exploded carbides $(S_V)_C = \dfrac{2(n_{02} + n_{03} + n_{05})}{L}$ and

Surface areas of exploded particles $(S_V)_P = \dfrac{2(n_{04} + n_{06} + n_{05})}{L}$,

where L is the total length of the test lines and G, C, P stands for grains, carbides and particles, respectively. During the calculation of $(S_V)_G$ 2 is multiplied with n_{01}, n_{07}, and n_{08} because when a test line intersects the boundary of two grains the number of intersection points were counted as one.

Contiguity of different phases

Contiguity of grains, carbides and particles were calculated by using the Eqn 2.4.

Contiguity of grains $C_G = \dfrac{2(2n_{01})}{(2n_{01} + 2n_{07} + 2n_{08})}$,

Contiguity of carbides $C_C = \dfrac{2(n_{03})}{(2n_{02} + n_{03} + n_{05})}$, and

Contiguity of carbides $C_P = \dfrac{2(n_{06})}{(n_{04} + n_{06} + n_{05})}$.

Size i.e. the mean intercept length of the grains of different phases

This parameter was calculated by using the Eqn 2.6.

Size of the grains $\left(\overline{L}_3\right)_G = 4 \dfrac{\left(V_V\right)_G}{\left(S_V\right)_G}$,

Size of the carbides $\left(\overline{L}_3\right)_C = 4 \dfrac{\left(V_V\right)_C}{\left(S_V\right)_C}$, and

Size of the particles $\left(\overline{L}_3\right)_P = 4 \dfrac{\left(V_V\right)_P}{\left(S_V\right)_P}$.

Number density in 2D

This parameter was calculated by using Eqn 2.8.

The number density of grains in 2 dimension $\left(N_A\right)_G = \dfrac{\left(N_T\right)_G}{A}$,

The number density of carbides in 2 dimension $\left(N_A\right)_C = \dfrac{\left(N_T\right)_C}{A}$, and

The number density of particles in 2 dimension $\left(N_A\right)_P = \dfrac{\left(N_T\right)_P}{A}$.

Probability of occurrence of features

Probability of occurrence of carbides inside the grains $\left(p_C\right)_{inside} = \dfrac{n_{09} - n_{11}}{n_{09}}$,

Probability of occurrence of carbides between two grains $\left(p_C\right)_{between} = \dfrac{n_{11} - n_{14}}{n_{09}}$,

and

Probability of occurrence of carbides on the triple points $\left(p_C\right)_{triple} = \dfrac{n_{14}}{n_{09}}$.

Similarly,

Probability of occurrence of particles inside the grains $\left(p_P\right)_{inside} = \dfrac{n_{10} - n_{12}}{n_{10}}$,

Probability of occurrence of particles inside the grains $\left(p_P\right)_{between} = \dfrac{n_{12} - n_{15}}{n_{10}}$, and

Probability of occurrence of particles at the triple points $(p_P)_{triple} = \dfrac{n_{15}}{n_{10}}$.

Total edge length of the grains in a unit volume

Total edge length in a unit volume was calculated by using the Eqn 2.10.

Total edge length of the grains between three grains in a unit volume

$$(L_V)_{GGG} = \frac{2n_{16}}{A},$$

Total edge length of the grains between two grains and carbides in a unit volume

$$(L_V)_{GGC} = \frac{2(3n_{14})}{A}, \text{ And}$$

Total edge length of the grains between three grains in a unit volume

$$(L_V)_{GGG} = \frac{2(3n_{15})}{A}.$$

3.4.2. Scanning electron microscopy

Scanning electron micrographs were obtained for all the samples after the hydrogen treatment in a scanning electron microscope (SEM) (JEOL JSM 840A). The samples were finely polished up to 0.5-micrometer finish using Al_2O_3 powder and then were etched before the SEM observations. The samples were over etched slightly in order to obtain better contrast for SEM observations.

3.5. Electrochemical polarization studies

Electrochemical polarization studies were conducted using a Perkin Elmer potentiostat (Model 263A). Its ± 20 V compliance and ± 200 mA (± 2 A with 94 Option) output capabilities allowed rapid and accurate potential or current control in the electrochemical cell. The schematic of a potentiostat connected with the polarization cell is shown in Figure 3.4. The potentiostat consists of an ammeter, an electrometer and a power supply. Three probes from the potentiostat were connected to the working electrode, reference electrode and counter electrode. The fourth probe was grounded. The polarization cell used for the polarization studies was the flat cell. The schematic representations of the flat cell are shown in Figure 3.5. The flat cell was used in the

present study. An Ag/AgCl electrode in saturated KCl was used as the reference electrode and the counter electrode was a platinum grid. The potential of the reference electrode was +197mV with respect to standard hydrogen electrode (SHE). The working electrode was placed in the flange and tightened so as to expose only $1 cm^2$ of the sample area to the electrolyte. The samples did not require any type of polymer mounting for this type of cell, as there was provision for attaching the sample without mounting. However, both the surfaces of the sample should be flat in order to prevent leakage of electrolyte.

Two sets of experiments were conducted. In the first set, a sample without any hydrogen treatment was tested at different normalities of H_2SO_4 from 0.1 N to 1.0 N to study the effect of acid solution of different strength. In the second set, experiments were carried out in a solution of 0.5 N sulfuric acid on the samples before and after exposure to hydrogen. The solutions were prepared using distilled water and laboratory grade chemicals. The surfaces of all the samples that were exposed in electrolyte were polished up to 4/0 emery paper and the samples were tested in the flat cell. As the exposed area of the hydrogen treated samples were less than $1 cm^2$, the samples were cold mounted. Cold mounting was done using a resin powder and organic solvent. An electrical wire was soldered before the mounting to the sample in order to provide electrical contact with the anodic point of the cell in this case. The sample with the attached wire was cold mounted to expose only the concerned surface. The exposed area was measured by slide calipers before attaching with the cell.

3.5.1. Free corrosion potential stabilization

The free corrosion potential (E_{corr}) was monitored after immersion of the samples in the electrolyte until a steady potential was obtained. These experiments used to define the range of experimental potentials in the electrochemical experiments. Proper care was taken so that the specimens were immersed in electrolytic solution for a minimum specified duration. Precautions were also taken to avoid any delay in starting the experiment immediately after immersing the specimen and providing the connections. All the experiments were performed twice for reproducibility purposes.

3.5.2. Potentiodynamic Polarization

The potentiodynamic polarization was carried out in the potential range of −700 mV to +1600 mV for all the samples. The experiments were started immediately after immersion of the alloy in the electrolyte. This prevented the formation of a surface film before the experiment was started. This also allowed comparison of $i_{critical}$. All potentiodynamic polarization experiments were carried out at a scan rate of 0.5 mV/s.
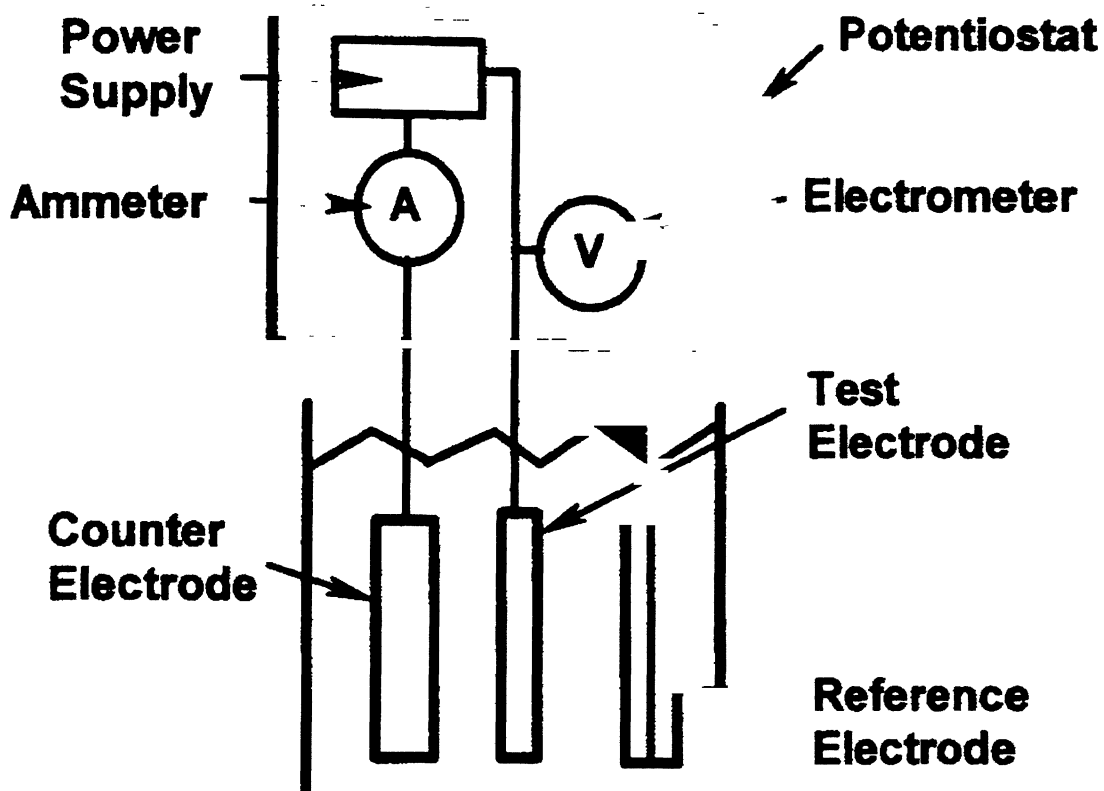
Figure 3.4   Schematic diagram showing the connections in the potentiostat
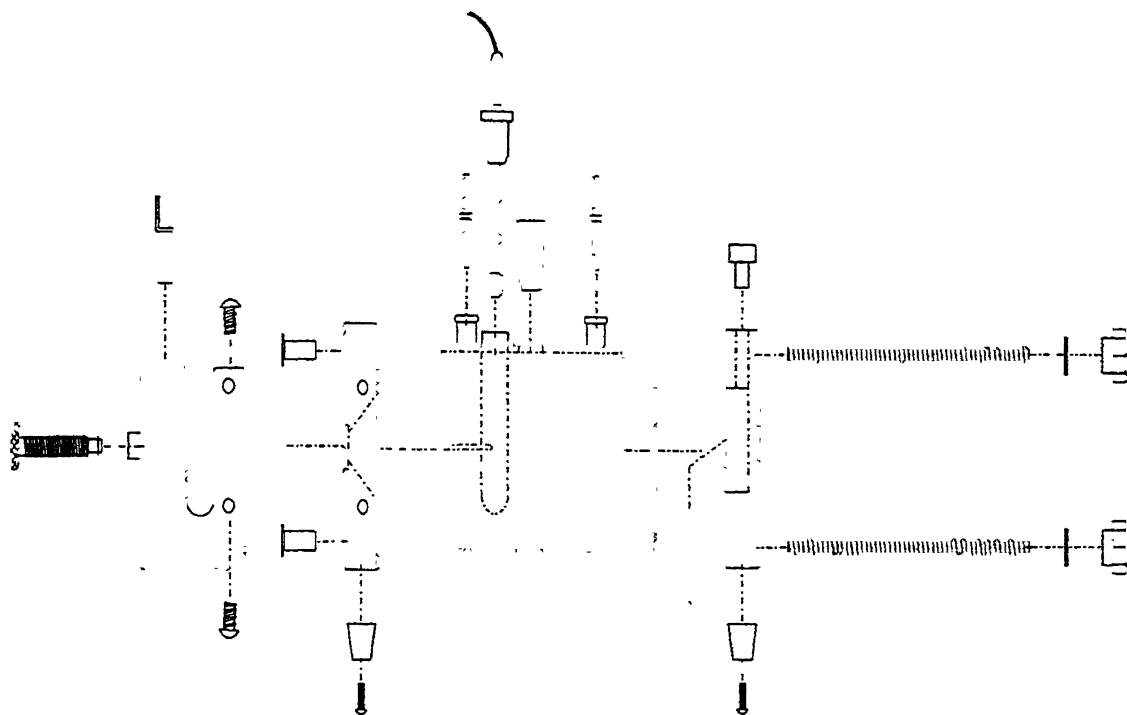
Figure 3.5   Schematic Representation of Flat Cell

CHAPTER 4

RESULTS AND DISCUSSION

4.1. Characterization of as-received material

The Fe-16.2Al-0.54C alloy obtained from Defense Metallurgical Research Laboratory (DMRL), Hyderabad, India was characterized in detail. The optical characterization, stereological characterization, structural analysis and compositional analysis will be discussed below in detail.

4.1.1. Microstructural characterization

The microstructures of the as-received iron aluminide alloys were initially analyzed. The alloys possessed recrystallized grains. This was expected because the thermomechanical processing of the alloys was performed at a high temperature (550^0C to 600^0C) where dynamic recrystallization had taken place [62]. The following discussion will focus attention on the Fe-16.2Al-0.54C alloy, as the hydrogen attack studies were conducted only for this alloy. The alloy exhibited a two-phase structure (Fig 4.1). According to Baligidad *et. al* [50,51], the matrix phase is based on Fe_3Al and the precipitates are $Fe_{4-y}Al_yC_x$ carbides possessing perovskite structure. The carbides were distributed uniformly throughout the matrix of iron aluminide. Two different types of morphology of the carbides were observed. The first type appeared as circular on the two-dimensional micrograph and the other as needle-shaped (Figure 4.1).

The optical micrographs of the four sections, i.e. long traverse, short traverse, rolling plane-I and rolling plane-II of as-received Fe-16.2Al-0.54C alloy are shown in the Figures 4.2a, 4.2b, 4.3a and 4.3b, respectively. This rolling plane-I and rolling plane-II refers to the planes at the top and bottom of the as-received plate. The carbides as well as the grains did not exhibit any directional elongation for the different sections, thereby indicating that recrystallization had taken place due to the high temperature thermomechanical processing of the ESR ingots of the alloy. The microstructures of rolling plane-I and II were similar. This confirmed that there were no variations in microstructure along the thickness of the sample. It was difficult to reveal
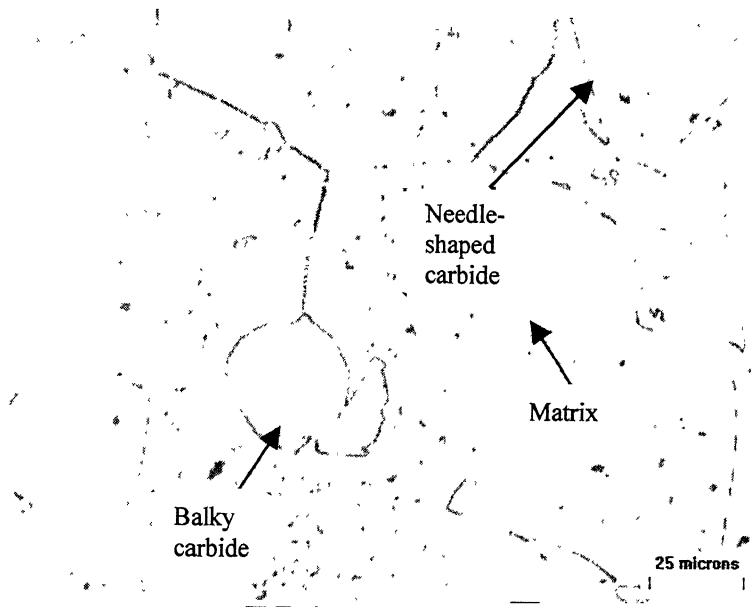
Figure 4.1   Optical micrographs of Fe-16.2Al-0.54C (wt %) showing the grains, bulky
              carbides and needle-shaped carbides

the grain boundaries in the microstructures of the long and short traverse sections by etching. If a longer time was allowed for etching, the needle-shaped carbides were darkened immediately along with the matrix. It is evident from the Figures 4.2 and 4.3 that the number density (N_A) of the needle-shaped carbides was higher in case of long and short traverse sections. However, the mean intercept length ($\overline{L_3}$) of the needle-shaped carbides is lower for these two sections. These microstructural aspects of the needle-shaped carbides result due to the hot rolling. During hot rolling, these carbides were elongated parallel to the rolling planes. The major axis of these carbides are aligned parallel to the rolling direction. Although the matrix was recrystallized during high temperature thermomechanical processing, the major axis of the needle-shaped carbides retained their shape. Therefore, the $\overline{L_3}$ of the needle-shaped carbides was higher in rolling plane than that in short and long traverse sections, whereas N_A was higher in case of short and long traverse sections than in case of the rolling plane.
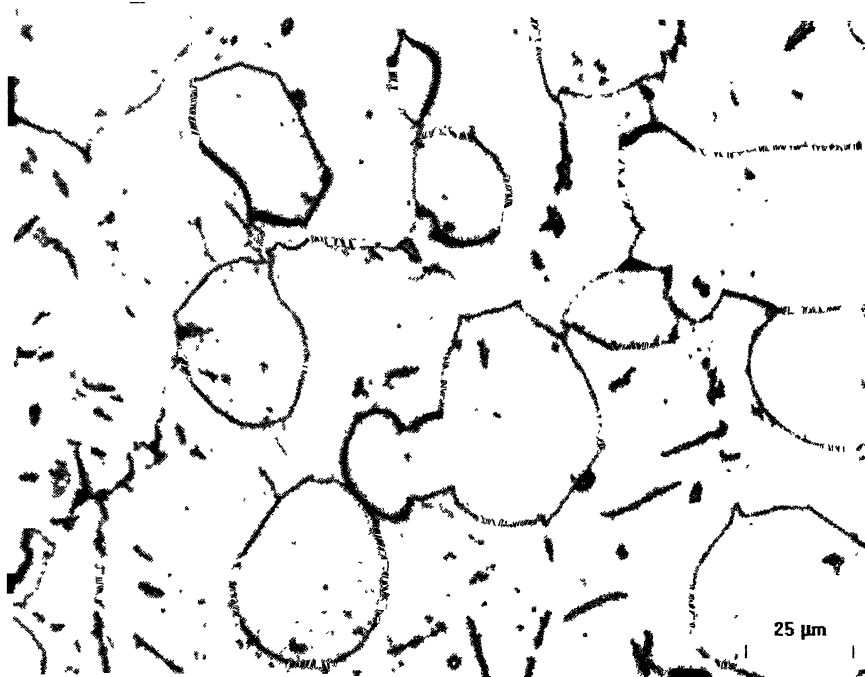
(a)
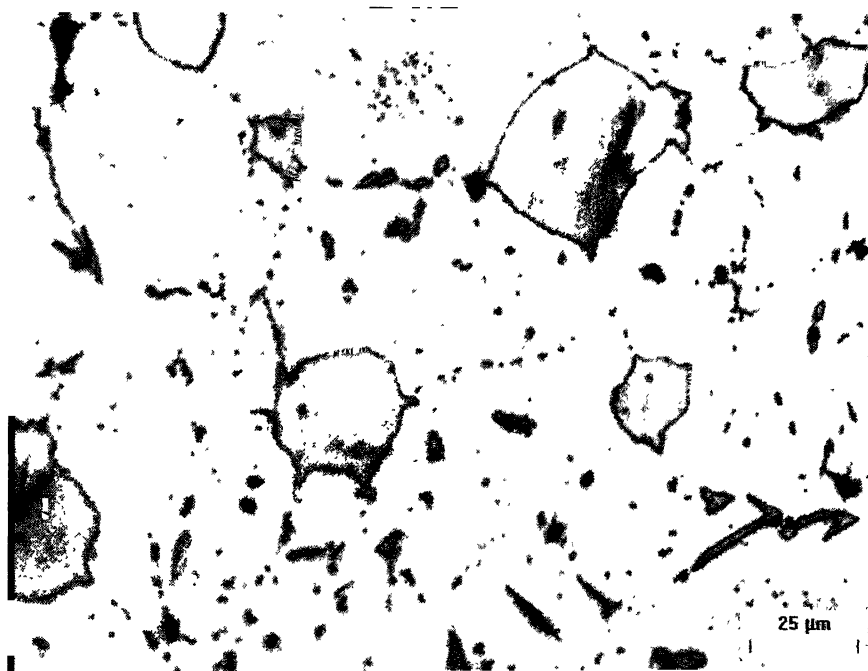
(b)

Figure 4.2   Optical micrograph of (a) long traverse section and (b) short traverse section of as-received Fe-16.2Al-0.54C alloy
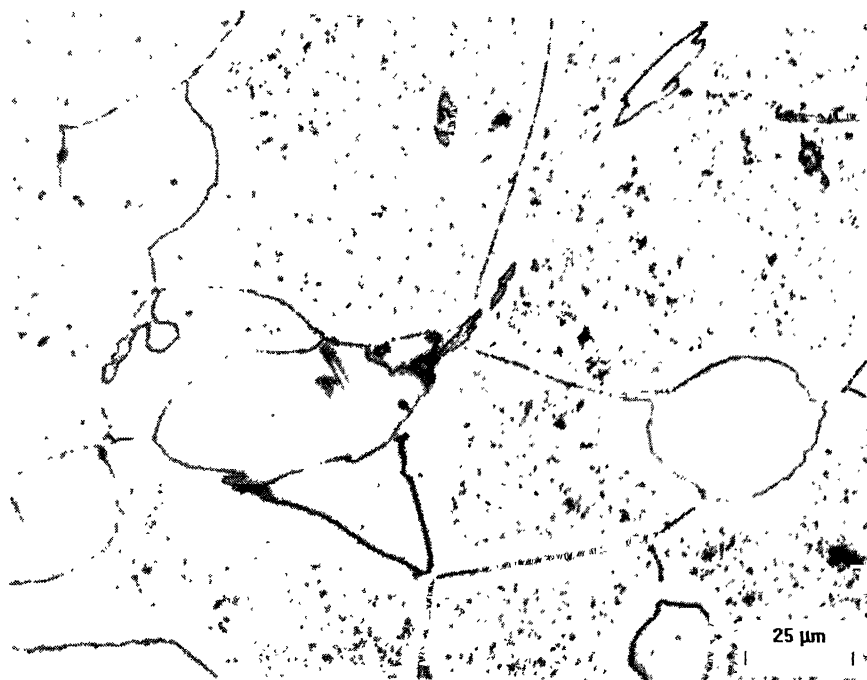
(a)

(b)

Figure 4.3   Optical micrograph of (a) Rolling plane-I section and (b) Rolling plane-II
              section of as-received Fe-16.2Al-0.54C alloy

4.1.2. Stereological analysis of as-received material

The rolling plane would be specifically discussed during the stereological analysis because the available area for analysis was larger for the rolling plane. The mean volume fraction ($\overline{V}_V$) and the surface area of exploded features per unit volume (S_V) for grains, bulky carbides and needle-shaped carbides were determined for the as-received material and these are reported in Table 4.1. The 95% confidence interval, which is a measure of the sampling error, is provided beside the individual measurements. The $\overline{V}_V$ data indicates that the microstructures predominantly contain grains and bulky carbides in the ratio of 4:1. The needle-shaped carbides contribute only about 1% of the microstructural volume. This observation is validated by the microstructures presented earlier (Figures 4.1 and 4.3a, b). It is interesting to note that although the $\overline{V}_V$ of needle-shaped carbides was the least, it possessed the highest percentage error. This implies that more sampling was required in the case of needle-shaped carbides to achieve the same confidence interval as that of bulky carbides. This is because the needle-shaped carbides occur very randomly in a field of view (FOV) since they are present in lower amounts. The second column in Table 4.1 provides the exploded surface area per unit volume (S_V) of different features. As all the three features (i.e. matrix, bulky carbides and needle-shaped carbides) are in the same microstructure, the ratio of S_V of these features gives the ratio of their absolute surface areas. The value of S_V depends on the following three parameters:

(I)   Amount of the feature: S_V increases as the amount of the feature increases, provided the size and shape of the feature are same.

(II)   Size of the feature: S_V decreases as the size of the feature increases, provided the amount and shape of the feature are same.

(III)   Shape of the feature: S_V increases as the shape of the feature becomes more acicular, provided the size and amount of the feature are same.

It can be seen (Table 4.1) that the exploded surface area of all the three features are of the same order of magnitude, although the $\overline{V}_V$ of grains and bulky carbides are an order of magnitude higher than that of needle–shaped carbides. This is due to the result of combination of the three factors stated above. The S_V value of matrix grains was the

maximum of all the three features due to its large value of $\overline{V}_V$ (although the grains were relatively large in size and not acicular in shape). The lower S_V of the bulky carbides than the grain matrix was due to their moderate values of $\overline{V}_V$ and $\overline{L}_3$. Although the needle-shaped carbides were low in $\overline{V}_V$, due to their small size and acicular shape they possessed almost similar value of S_V as bulky carbides.

Table 4.2 presents the contiguity, the mean intercept length and two-dimensional number density of different phases. Contiguity is a measure of the fractional surface area of each feature occupied by other features of the same type. As the contiguity values of bulky carbides and needle-shaped carbides is very low, it indicates that occurrence of contacting bulky carbides and contacting needle-shaped carbides are very rare. In other words, these features avoid features of the same type. Mean intercept length $(\overline{L}_3)$ provides a measure of the size of the features. As can be seen from the micrographs in Fig. 4.1, 4.3a and 4.3b, the grains possess the largest $\overline{L}_3$ and the needle-shaped carbides have the smallest. This is a derived result from $\overline{V}_V$ and S_V measurements. The error is higher since the errors in the $\overline{V}_V$ and S_V get accumulated. The last column in Table 4.4 provides the two-dimensional number density of different features. This has been reported for the sake of completeness without having any direct bearing on any 3D quantity.

Table 4.3 provides the total edge length between three grains, two grains and bulky carbides, and two grains and needle-shaped carbides. This information is useful for diffusional modeling where these edge lengths can be used to represent and understand short-cut paths for diffusion. It can be seen from the Table 4.3 that the edge length between bulky carbides and matrix is approximately two times more than that between three grains of matrix or between needle-shaped carbides and matrix. Therefore, it is anticipated that hydrogen (and carbon) would diffuse much more easily through the interfaces between the bulky carbides and matrix. In that way, the edge lengths could be utilized to understand hydrogen attack at elevated temperatures.

Table 4.4 contains the probability of occurrence of bulky carbides and needle-shaped carbides at different locations. It is seen that bulky carbide is 3.5 times more

likely to occur on a grain triple point and two times more likely to occur between two grains as compared to inside a grain. This must be related to the sympathetic nucleation of the carbides at heterogeneities and also to the easy diffusion of carbon through grain boundaries, during the formation of these carbides. On the other hand needle-shaped carbides are more likely to occur inside grains than between grains or in between triple points. It may also be noted that the measurement of occurrence of needle-shaped carbides at grain triple points has an appreciable error due to its very random occurrence and due to the lower volume fraction of the needle-shaped carbides.

Table 4.1   Volume fraction and exploded surface area of different features on the rolling plane of as-received Fe-16.2Al-0.54C alloy

Features	Volume fraction		Exploded surface area (μm^{-1})	
	mean	95% confidence interval	Mean (μm^{-1})	95% confidence interval
Bulky carbides	0.189	0.038	0.019	0.093
Needle-shaped carbides	0.016	0.149	0.017	0.110
grains	0.795	-	0.042	0.049

Table 4.2   Contiguity, mean intercept length and number density in 2D of different features on the rolling plane of as-received Fe-16.2Al-0.54C alloy

Features	Contiguity		Mean intercept length ($\bar{L}_3$)		Number density in 2D	
	mean	95% confidence interval	Mean (μm)	95% confidence interval	Mean (μm^{-2})	95% confidence interval
Bulky carbides	0.027	0.551	55.046	0.131	0.141	0.076
Needle-shaped carbides	0.034	0.453	5.576	0.259	0.538	0.076
grains	0.657	0.113	82.562	0.049	0.139	0.054

Table 4.3   Total edge length in unit volume of as-received Fe-16.2Al-0.54C alloy determined from the rolling plane section

Location	Mean (μm^{-2})	95% confidence interval
Between three grains	0.171	0.015
Between grains & bulky carbides	0.440	0.111
Between grains & needle-shaped carbides	0.184	0.247

Table 4.4   Probability of occurrence of bulky carbides and needle-shaped carbides

Location	Bulky carbides		Needle-shaped carbides	
	Mean	95% confidence interval	Mean	95% confidence interval
Inside grains	0.145	0.338	0.602	0.181
Between grains	0.309	0.268	0.342	0.186
On triple points	0.546	0.183	0.057	0.333

4.1.3. Structural Analysis

The structure of the carbides was analyzed by X-ray diffraction and their compositions were determined by EPMA. These will be presented and discussed below.

The X-ray diffraction pattern of the as-received alloy Fe-16.2Al-0.54C using CuK_{α} (λ = 0.15045) radiation is shown in Figure 4.4 [48]. The presence of Fe_3AlC precipitates in the matrix was confirmed. The Fe_3AlC phase possesses a FCC crystal structure with Al atoms occupying the corners of the cube, Fe atoms at the face centers and the carbon atom at the body center position (i.e. the octahedral void at ½, ½, ½) [55]. The published lattice parameter (a) of the structure is 0.377 nm while indexing of carbide peaks in the pattern provided a lattice parameter of 0.374 nm [48]. The slight mismatch of the calculated lattice parameter with the published lattice parameter was explained to result due to the relative small number of d_{hkl} values utilized to calculate the lattice parameter [48].
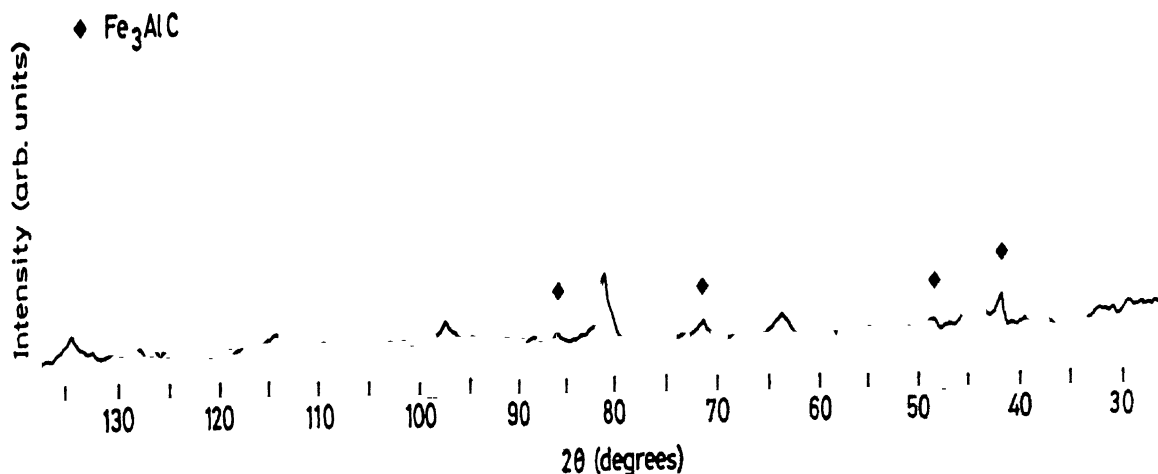
Figure 4.4   XRD pattern of as-received Fe-16.2Al-0.54C alloy using CuK_α (λ = 0.15405 nm) radiation [48].

4.1.4. Compositional Analysis

The hot mounted metallographic samples of the long traverse, short traverse, rolling plane-I and rolling plane surfaces of the Fe-16.2Al-0.54C (Fe-28.1Al-2.1C in at %) were compositionally analyzed in the electron probe micro-analyzer (EPMA). Compositions were analyzed by point analysis in order to determine the local compositions at different locations. The results of point compositional analysis are reported in Table 4.5 and 4.6. The compositions have been reported in atomic percent in order to elucidate the stoichiometric formula of the matrix and the carbide phase.

The composition of the matrix was generally similar for all the sections. The atomic percent of iron, aluminium and carbon of the matrix varied in the range of 71.84 to 77.44, 21.96 to 27.80 and 0.35 to 2.25, respectively. It is evident from this range of compositions that the atomic ratio of iron and aluminium in the matrix is in the order of 3:1, thereby suggesting the stoichiometric formula of the matrix phase as Fe_3Al. Interestingly, the Al contents in the matrix phase for the rolling plane sections were generally slightly lower than for short and long traverse sections, the reasons for which are not known.

The composition of the bulky carbides approximates to 64.17Fe-19.81Al-18.35C. In two instances (indicated by italics in Table 4.5), the carbon content in the bulky carbide phase was lower. This must have resulted because of the interaction volume of the incident electron beam in the EPMA enveloping a significant percentage of the matrix phase, probably due to the orientation of the bulky carbide in the location from where the analysis was obtained.

The needle-shaped carbides exhibited much wider variations (the low carbon containing analyses have been italicized in Table 4.5 and 4.6), but generally could be approximated as 62.40Fe-19.87Al-17.73C, similar to the bulky carbides. The higher number of data points for the needle shaped carbides indicating lower carbon content must be due to the interaction volume of the matrix included in the analysis. This is anticipated as needle-shaped carbides are relatively small in size. It is therefore very difficult to perform precise point analysis on needle-shaped carbides due to their size.

The stoichiometric formula of the bulky carbides can be written as $Fe_{4-y}Al_yC_x$, where y varies from 0.91 to 1.19 and x varies from 0.90 to 1.02. Similarly the formula of the needle-shaped carbides can be written as $Fe_{4-y}Al_yC_x$, where y varies from 0.99 to 1.12 and x varies from 0.82 to 0.96. This formula is compatible with the formula suggested as $Fe_{4-y}Al_yC_x$ (where y varies from 0.42 to 0.71 and x varies from 0.8 to 1.2) by Palm *et.al.* [10], whereas Baligidad *et.al.* [50] suggested the formula of the carbide as $Fe_3AlC_{0.5}$.

Table 4.5   Summery of compositional of Fe-16.2Al-0.54C alloy at several different locations in long and short traverse sections

Plane of view	Phase	Composition (at%)		
		Iron	Aluminium	Carbon
Long transverse	Matrix	71.84	27.80	00.35
		72.07	26.73	01.20
	Bulky carbide	63.97	20.69	15.33
		62.98	30.41	06.61
		71.36	26.33	02.31
	Needle-shaped carbide	61.38	22.49	16.13
		61.50	19.90	18.60
		61.97	18.91	19.11
		69.06	26.94	04.00
Short transverse	Matrix	72.76	26.25	00.99
		73.39	24.39	01.22
	Bulky carbide	67.80	18.18	18.02
		69.82	26.74	03.44
		63.23	20.10	16.67
		59.77	21.11	19.12
	Needle-shaped carbide	64.63	28.06	07.30
		65.27	29.01	05.73
		65.43	16.03	18.53
		65.19	29.40	05.42

Table 4.6   Summery of compositional of Fe-16.2Al-0.54C alloy at several different locations in rolling plane-I and rolling plane-II

Rolling plane-I	Matrix	77.44	21.96	00.60
		73.72	25.34	00.94
	Bulky carbide	71.27	20.14	18.61
		58.44	21.13	20.42
		72.25	*26.51*	*01.24*
	Needle-shaped carbide	*72.50*	*24.92*	*02.58*
		62.96	19.70	17.34
		73.18	*26.10*	*00.72*
Rolling plane-II	Matrix	75.63	22.13	02.25
		72.38	26.84	00.78
	Bulky carbide	61.01	20.28	18.71
		62.55	18.43	19.02
	Needle-shaped carbide	69.25	26.48	04.27
		62.98	20.69	16.33

4.2. Thermodynamic and kinetic considerations

The thermodynamic feasibility of methane formation in Fe-16.2Al-0.54C was theoretically examined at 700°C and at 900°C. Moreover, the kinetics of hydrogen diffusion into the material was evaluated theoretically to obtain insights on the depth of attack.

4.2.1. Thermodynamics

Karnaukhov and Morozov (1947), and Nizhelskii (1957) showed that the solubility of hydrogen in molten iron diminishes with increasing carbon content [57]. Nizhelskii observed a small increase in the solubility at carbon content greater than 4% It is observed that at 0.54 wt % of carbon (as present in the as-received alloy) the decrease in hydrogen solubility is only 2 cc per 100 gms (i.e. 1.78×10^{-4} wt % hydrogen) of molten iron at 1550°C. Klyachko and Izmanova (1957) found an increasing absorption of hydrogen with increasing carbon content in the range 0.025 to 02.64 wt %. A little quantitative data exist about the influence of aluminium on the solubility of hydrogen in steel. Karnaukhov and Morozov obseveda decrese of solubility with increase in aluminium content in steel [57].

The amount of hydrogen required for the formation of methane in as-received Fe-16.2Al-0.54C (wt %) alloy at 700°C and at 900°C was theoretically computed and compared with hydrogen solubility. The free energy required for the methane formation due to the reaction (Eqn. 4.1) of carbon in the alloy and hydrogen dissolved in the alloy was calculated from the Eqn. 4.2, 4.3 and 4.4. This free energy value was used to figure out the solubility of hydrogen in the alloy. As enough data was not available on the diffusivity of hydrogen in iron aluminide alloys, the calculation was based on the data on diffusivity of hydrogen in α-iron. Measurements of the solubility of hydrogen in carbon alloys were complicated by the formation of methane, and hence the few experimental data found in the literature are controversial.

In atmosphere containing hydrogen methane forms in steels at higher temperature by the reaction stated below.

$$[C]_{Fe} + 4[H]_{Fe} = CH_4(gas)$$ eqn. 4.1

This reaction can be obtained from the reactions stated below.

$$C(gr) + 2H_2(gas) = CH_4(gas) \qquad \text{eqn. 4.2}$$

$$\tfrac{1}{2} H_2(gas) \Rightarrow [H]_{Fe} \qquad \text{eqn. 4.3}$$

$$C(gr)) \Rightarrow [C]_{Fe} \qquad \text{eqn. 4.4}$$

$$C(gr) + 2H_2(gas) = CH_4(gas) \qquad \text{eqn. 4.2}$$

For this reaction, the Gibb's free energy (ΔG_2) is given by ($-91040 + 110.7T$) J (range 773K to 2000K) [58]. The energy as reported in another source [59] is ($-69120 - 22.25T \ln T - 65.34T$) J. Therefore, the energies ($\Delta G_{2'}$) estimated at 700°C using these relations are 16671.10 J and 16259.34 J, respectively, while at 900°C, are 38811.1 J and 38687.93 J, respectively. It is evident from the free energy values that both the relationships provide comparable values.

$$\tfrac{1}{2} H_2(gas) \Rightarrow [H]_{Fe} \qquad \text{eqn. 4.3}$$

For the eqn. 4.3, the equilibrium constant, K, as the reciprocal of the absolute temperature has been provided by Dyakonov and Samarine. Straight-line relationships (Fig. 4.5) were found for every form of iron. They also computed the free energy change of this reaction from the solubility data of Sieverts et al [57] using the Vant Hoff's equation. According to them, the equilibrium constant as a function of temperature ca be represented by [57]

$$\log K_\alpha = -\frac{1250}{T} - 2.51 \ (\alpha\text{-iron}),$$

$$\log K_\gamma = -\frac{1220}{T} - 2.335 \ (\gamma\text{-iron}),$$

$$\log K_\delta = -\frac{1340}{T} - 2.46 \ (\delta\text{-iron}) \ \text{and}$$

$$\log K_l = -\frac{1590}{T} - 1.71 \ (\text{liquid iron}) \qquad \text{eqn. 4.5}$$

The data for α-iron was utilized and calculated K_α values are 1.604 X 10^{-4} and 2.655X10^{-4} at 700°C and 900°C, respectively. Using the relation (ΔG^0 = -RT lnK) between change in

The data for α-iron was utilized and calculated K_α values are 1.604×10^{-4} and 2.655×10^{-4} at 700°C and 900°C, respectively. Using the relation ($\Delta G^0 = -RT \ln K$) between change in free energy and equilibrium constant, K, at standard state the ΔG_3 was calculated as 70689.20 J and 80297.97 J at 700°C and 900°C, respectively. Interestingly, Dyaknov and Samrine [57] provided another equation ($\Delta G = 5730+11.5T$ cal/mole) for calculating free energy change for reaction 4.3 for α-Fe. Utilizing this equation, $\Delta G_{3'}$ was calculated as 70791.19 J and 80414.39 J at 700°C and 900°C, respectively.

$$C(gr)) \Rightarrow [C]_{Fe} \hspace{4cm} \text{eqn. 4.4}$$

For the eqn. 4.4, the free energy change is given by $\Delta G_4 = (22600 - 42.26T)J$ [58,59]. Utilizing this, ΔG_4 is determined as -18518.98 J and -26970.98 J at 700°C and 900°C, respectively.

Therefore, the free energy change for eqn. 4.1 (i.e. the ΔG for the formation of 1 mole of CH_4) can be obtained from the free energies determined above by the relation $\Delta G_1 = \Delta G_2 - 4 \times \Delta G_3 - \Delta G_4$. ΔG_1 was determined at 700°C and 900°C using the evaluated values above. All combinations were utilized. This provided the following values for ΔG_1 (Table 4.7).

Table 4.7   Free energy change for the formation of 1 mole of CH_4 due to the reaction of carbon in Fe-16.2al-0.54C alloy and hydrogen dissolved in the alloy

ΔG_1 values (J)	At temperature 700°C	900°C	The ΔG values used (J)
$(G_1)_1$	-247566.72	-255409.8	G_2, G_3 and G_4
$(G_1)_2$	-247974.68	-255875.48	G_2, $G_{3'}$ and G_4
$(G_1)_3$	-247978.48	-255532.97	$G_{2'}$, G_3 and G_4
$(G_1)_4$	-248386.44	-255998.65	$G_{2'}$, $G_{3'}$ and G_4

Expressing the relationship between the equilibrium constant and free energy for equation 4.1 in terms of partial pressure of methane, we obtain

$$\Rightarrow [H]_{Fe}^4 = \frac{f_{CH_4}}{[C]_{Fe}} \times e^{\frac{\Delta G_1}{RT}}$$

Eqn. 4.6

It has been assumed that in the dilute solution of carbon in the alloy $[C]_{Fe} = 0.54$ wt%. The hydrogen contents required (in wt %) for methane formation at 700°C and 900°C, for f_{CH_4} varying in the range of 1 to 10^{-3} atmosphere have been calculated and tabulated in Table 4.8. The fugacity of methane is related to its partial pressure and this has been provided elsewhere. This will not be discussed because the partial pressure of methane is adequate to understanding the present results.

Table 4.8   Values of hydrogen contents required (in wt %) for methane formation in α-iron at 700°C and 900°C

Temperature (°C)	Methane pressure (atmosphere)			
	1	1×10^{-1}	1×10^{-2}	1×10^{-3}
700	5.47×10^{-4}	3.09×10^{-4}	1.73×10^{-4}	0.10×10^{-4}
900	16.47×10^{-4}	9.26×10^{-4}	5.21×10^{-4}	2.93×10^{-4}

As the partial pressure of hydrogen used during the treatments was 1 atmosphere the estimated hydrogen content in the alloy at 700°C and 900°C is much higher than the hydrogen contents required for methane formation (Table 4.8). Hence, the formation of methane at 700°C and 900°C is thermodynamically feasible. If it is assumed that hydrogen solubility in Fe-16.2Al-0.54C alloy is similar to that in Fe, then the same estimation can be made.

The solubility of hydrogen in α-Fe (BCC) can be expressed by the following formula [61]

$$\log(at\%H) = -\frac{1376}{T} - 0.655$$

eqn. 4.7

where T is in Kelvin.

$$\log(at\%H) = -\frac{1376}{T} - 0.655 \qquad \text{eqn. 4.7}$$

where T is in Kelvin.

Therefore, the solubility of hydrogen is 1.50×10^{-4} wt % and 2.62×10^{-4} wt % at 700°C and 900°C, respectively. The solubility of hydrogen in iron at 724°C and at 899°C was reported as 1.79×10^{-4} wt % and 3.95×10^{-4} wt %, respectively, in another source [57] and therefore, comparable to the values obtained from eqn. 4.6.

Comparing the hydrogen solubility with the methane fugacities generated (Table 4.7), it is evident that methane fugacity must be around near to 1×10^{-3} atmospheres. Moreover, it can be concluded that methane formation in Fe-16.2Al-0.54C is thermodynamically feasible during hydrogen treatment at 700°C and at 900°C. The methane pressure developed due to hydrogen attack can be utilized for modeling hydrogen attack, as per the theoretical models proposed [64]. However, this has not been addressed due to enormous computation involved.

4.2.2. Kinetics

The depth up to which hydrogen attack can take place (and hence the formation of methane) in Fe-16.2Al-0.54C at 700°C and 900°C has been determined.

The temperature dependence of hydrogen diffusion in α-Fe is given by [57]

$$D_T = D_0 \exp\left(-\frac{12133.6 \; J \; per \; mol}{RT}\right) \qquad \text{Eqn. 4.8}$$

where D_T is the diffusivity at temperature T (in degrees Kelvin), Do is the pre-exponential constant and is the universal gas constant. From this equation, D_T has been calculated as 4.78×10^{-4} cm^{2}sec^{-1} and 6.17×10^{-4} cm^{2}sec^{-1} at 700°C and 900°C considering the D_T at 298 K as 1.6×10^{-5} cm^{2}sec^{-1} [57].

Assuming that unidirectional hydrogen diffusion occurs from the surface into the alloy under unsteady state, the dependence of concentration with time and diffusion distance is given by Fick's second law [60, 65]

$$\frac{\partial c}{\partial t} = D \frac{\partial^2 c}{\partial^2 x} \qquad \text{eqn. 4.9}$$

$$\frac{C_{x,t} - C_0}{C_s - C_0} = 1 - erf\left(\frac{x}{2\sqrt{Dt}}\right),$$

<div align="right">eqn. 4.10</div>

where, $C_{x,t}$ is the hydrogen level at a distance x from the surface after the diffusion time t, C_0 is the base hydrogen content, C_s is the hydrogen content at surface and D is the diffusivity of hydrogen in α-iron. In the present study, C_0 is assumed as 0, C_s is 1.50×10^{-4} wt % and 2.62×10^{-4} wt % at 700°C and 900°C, respectively (estimated earlier). The concentration of hydrogen in Fe-16.2Al-0.54C alloy as a function of diffusion distance x and time at 700°C and 900°C has been plotted in Figure 4.6. The depth of penetration is higher at higher temperature and time, as expected. The methane pressure expected can be estimated utilizing this figure and eqn. 4.5. This has been shown in Figure 4.7. It is observed that the methane pressure decrease rapidly with increasing distance into the material. Maximum hydrogen attack is therefore anticipated in the region near the surface. Therefore, it is reasonable to undertake microstructural characterization after hydrogen treatments on the surfaces.
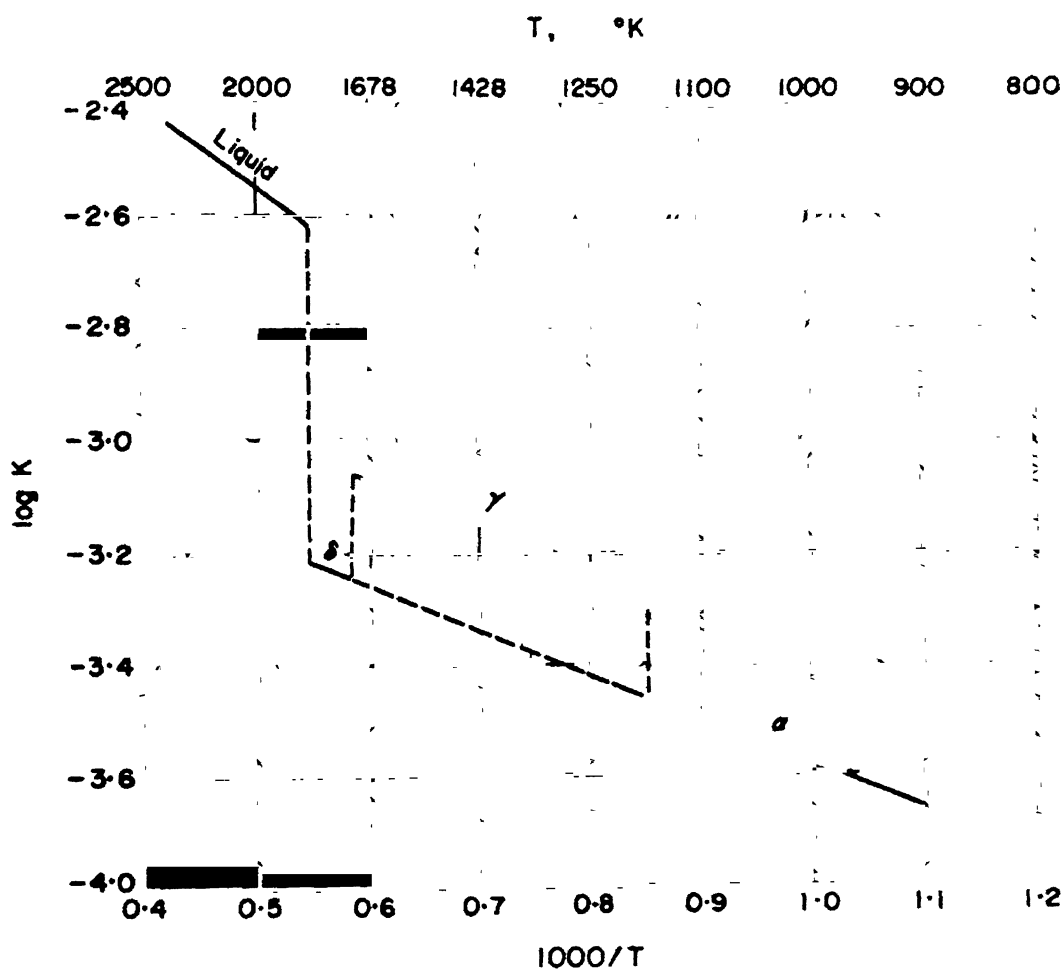
Figure 4.5   Solubility isobar for hydrogen in iron at 1 atm. pressure (Dyaknov and
Samarine)
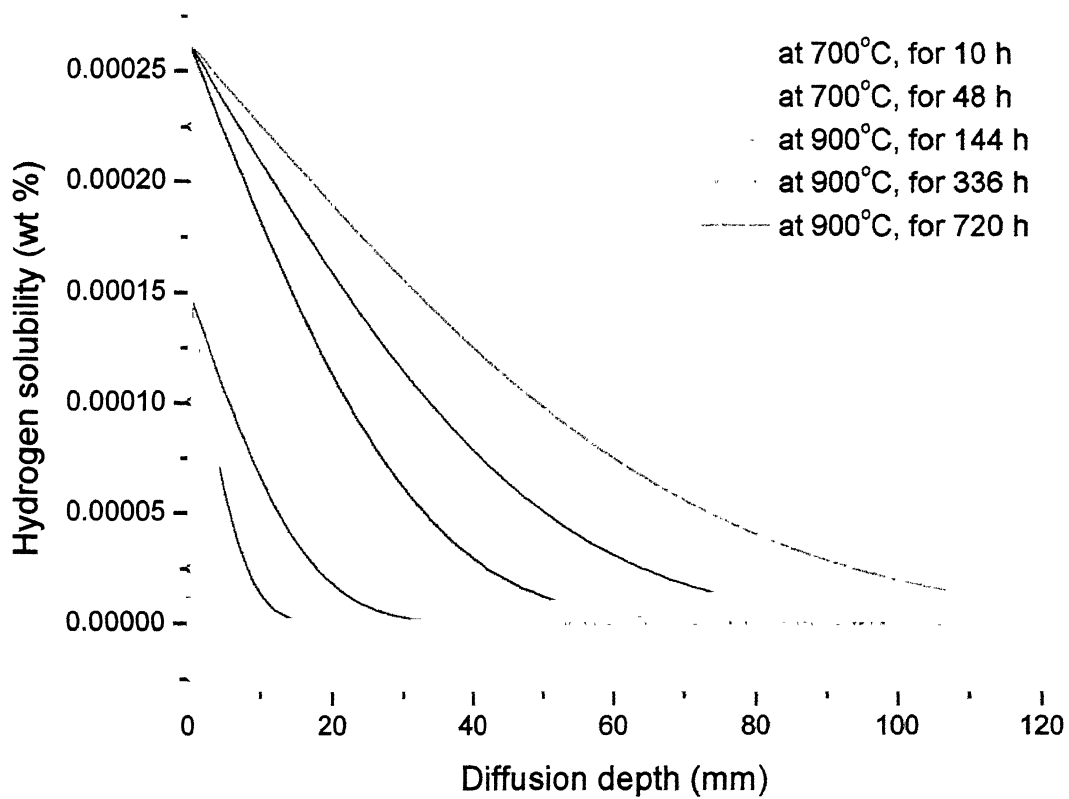
Figure 4.6   Hydrogen solubility in α-Fe at 700°C and 900°C for different time
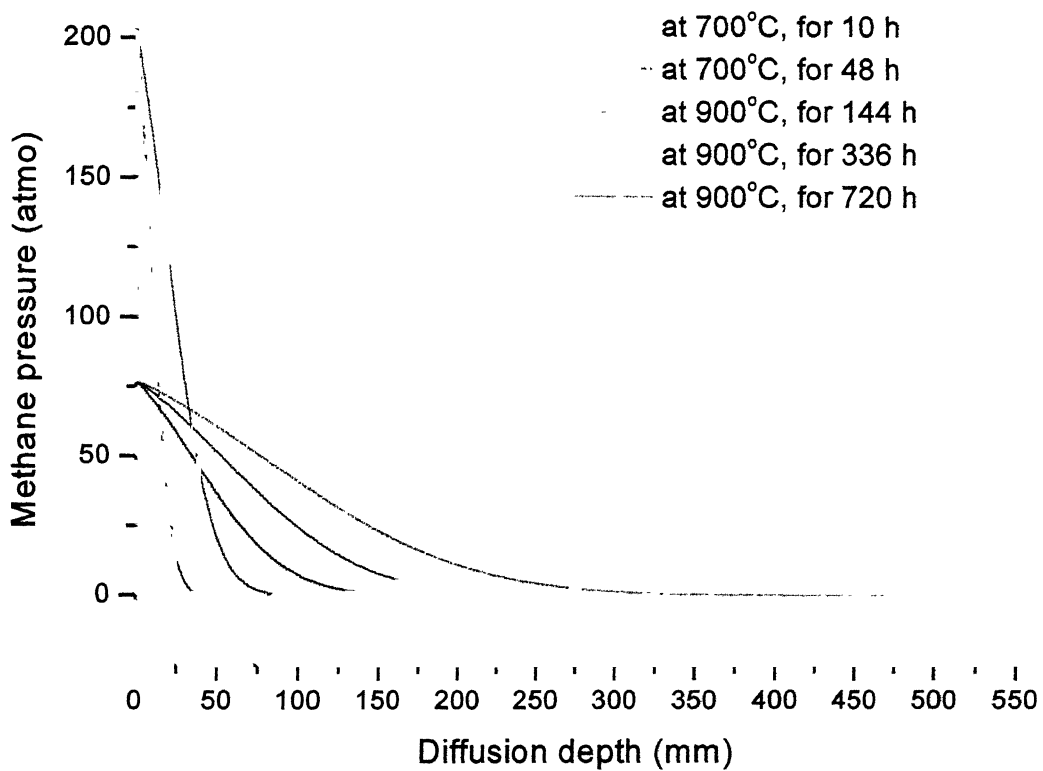
Figure 4.7   Methane pressure with respect to hydrogen diffusion depth in α-Fe at 700°C and 900°C for different time

4.3. Characterization after hydrogen treatment

The effects of high temperature hydrogen treatment on the carbon alloyed iron aluminides for the following five different conditions will be addressed:

(I)   700°C and 10 hours

(II)   700°C and 48 hours

(III)   900°C and 144 hours

(IV)   900°C and 336 hours and

(V)   900°C and 720 hours

The rolling section was observed by optical and scanning electron microscopy (SEM) for understanding the effect of hydrogen treatment. These will be discussed separately below.

4.2.2. Optical microscopy

Figures 4.8a and 4.8b present the optical micrographs after hydrogen treatment at 700°C for 10 hours and 48 hours, respectively, for the Fe-16.2Al-0.54C alloy. Some hairline attack on the blocky carbides was noticed in the sample hydrogen treated for 10 hours (Figure 4.8a). The degree of attack was enhanced in case of sample, treated for 48 hours. The width of the line of attack was more in this case (Figure 4.8b). Some of the interfaces between the blocky carbides and the grains of the matrix were also observed to be degraded (although less severely). The carbides along those interfaces were decomposed slightly in the process of methane formation. The thermodynamic feasibility of methane formation in the Fe-16.2Al-0.54C alloy during hydrogen treatment at 700°C will be discussed later in this chapter.

It was also noticed that the needle-shaped carbides were spherodized in the sample treated for 10 hours. The spherodized needles were smaller in size. Neither the needle-shaped carbides nor the spherodized carbides were observed in the case of 48 hours treatment. The decomposition of the smaller needle-shaped carbides could be due to dissolution process, whereby the larger carbides grow at the expense of smaller ones by Ostwold-ripening process [60].

The optical micrographs after hydrogen treatment at 900°C for 144 hours are shown in Figure 4.9. The experiment at 900°C for 144 hours was repeated and the micrographs (a) and (b) are from two separate duplicate experiments. It can be seen from the micrographs that the degradation of the blocky carbides was more enhanced in this case. However, the degree of attack was not apparently increased at the interfaces of the carbides and matrix. The tendency of spherodization of the carbides into a more regular spherodized shape was also observed.

Figures 4.10a and 4.10b show the optical micrographs of hydrogen treated alloy at 900°C for 336 hours and 720 hours, respectively. Interestingly, hydrogen attack at the carbide parse was noticed in only a few carbides. In contrast to the earlier case, the interfaces between the carbides and matrix were significantly affected. It is evident from Table 4.5 that the edge length between the matrix and carbides is higher than between three grains of matrix or between two grains and carbides. As these edge lengths can act as short cut diffusion paths for hydrogen at higher temperature, the pronounced hydrogen attack at the interface between the blocky carbides and grains could be understood. The pores formed at the interfaces between the bulky carbides and the matrix could probably be due to methane formation in the sample treated for 720 hours. It is unlikely that the attack in the carbides after hydrogen treatment at 900°C for 336 hours and 720 hours was polished (removed) out during metallographic surface preparation, as only a slight polish was employed before observation, and the same procedure applied for the earlier samples were employed. Therefore, the probable reason for the lower degree of attack of bulk carbides had to be understood. As the properties varied with time and temperature of exposure, the nature of the surface after the treatments needed to be understood before the polishing procedure. The surfaces were observed in the SEM for this purpose.

(a)
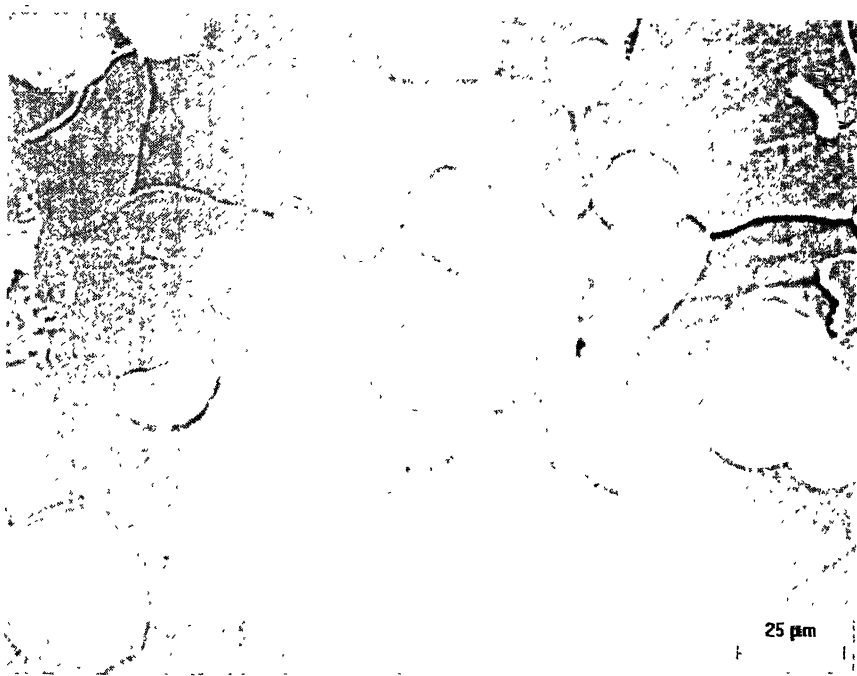
(b)

Figure 4.8   Optical micrographs showing the surface features after hydrogen treatment at (a) 700°C for 10 h, and (b) 700°C for 48 h.

(a)

(b)

Figure 4.9   Optical micrographs showing the surface features after hydrogen treatment at (a) $900^{\circ}C$ for 144 h-I, and (b) $900^{\circ}C$ for 144 h-II (duplicate experiment).

(a)

(b)

Figure 4.10   Optical micrographs showing the surface features after hydrogen treatment at (a) 900°C for 336 h, and (b) 900°C for 720 h.

4.2.2. Scanning electron microscopy

All the samples after the hydrogen treatment were observed in the SEM in order to understand the effect of hydrogen treatment. The surfaces were observed both before and after the slight polish. The discussion will deal with the later case first.

Figures 4.12 show the SEM micrographs of hydrogen treated alloy at 700°C for 10 hours. Features of hydrogen attack were not evident at low magnification (Fig. 4.4a). However, the attack at the bulky carbides was distinctly visible at higher magnifications (Fig. 4.12b through d). It can be seen that only a few carbides were affected due to the hydrogen treatment. Figure 4.12d reveals that the attack was on certain crystallographic direction, based on the straight nature of the attack features. Moreover, all the lines formed due to the attack were not of same length. It is also interesting to observe that the lines of the attack were arranged within certain specific angles. Most of the lines were arranged between an angle of $27°$ to $30°$. This may be because the reaction proceeded along certain preferred planes, possibly due to surface energy considerations. The crystal structure of the carbide is an ordered FCC arrangement of type Ll_2, with carbon atom in the octahedral interstice. A perfect atomic arrangement of this type would be correspond to the formula Fe_3AlC possessing perovskite structure (Figure 4.11). It is determined that 15 out of 42 combinations of the planes $\{111\}$ and $\{110\}$ make an angle of $35.26°$ between them. As the plane of viewing was not on the exact crystallographic orthogonal coordinates it is anticipated that the angle between planes would be lower than theoretically expected. Therefore, it is reasonable to conclude that the planes along which hydrogen attack proceeds in the carbides are $\{111\}$ and $\{110\}$. Moreover, this is reasonable because they are low index planes. The reason for the degradation to occur along these planes needs to be understood. In the Fe_3AlC structure, the $\{111\}$ and $\{110\}$ planes contain both carbon and aluminum atom (Figure 4.11). The attack may have been preferred on these planes as both carbon and aluminium are removed during the high temperature hydrogen treatment. The reaction of carbon and hydrogen during hydrogen

treatment and the reaction of aluminium with oxygen (thermodynamic feasibility of oxidation of aluminum is proved later in this chapter) are the two important reactions.

The SEM micrographs after hydrogen treatment at 700°C for 48 hours are shown in Figures 4.13. The carbides were affected more severely in this case, although all the carbides did not get affected, like in the previous case of 10 hours. The lines of attack were wider and deeper compared to earlier case and indicated similar preferred alignment among themselves (Fig. 4.13c and d). It was also noticed also that the interfaces between bulky carbides and the matrix were attacked. This was not noticed in earlier case of 10 hours treatment at700°C. The disappearance of the needle-shaped carbides must also be noted (Fig. 4.13b).
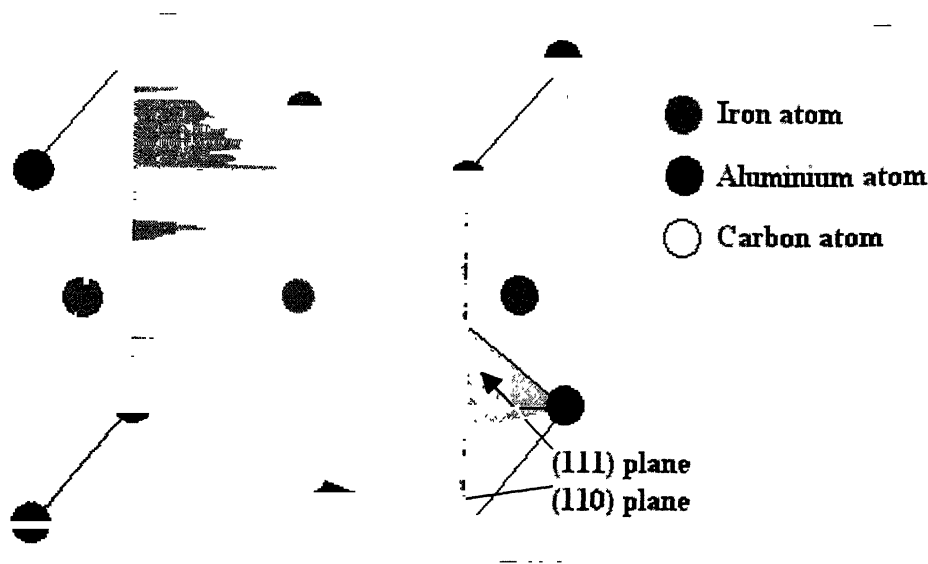
Figure 4.11   The perovskite structure of Fe₃AlC carbide showing the planes of attack ((111) and (110))

Figures 4.14 and 4.15 show the SEM micrographs of hydrogen treated alloy at 900°C for 144 hours. The effect of hydrogen treatment was more prominent in this case. It can be noticed that a larger number of carbides were attacked in this case (Fig. 4.14a, b and Fig. 4.15a, b) than in the case of 48 hours treatment at 700°C. It appears that the line attacks in the bulky carbides was similar to that observed for the samples treated at 700°C. However, they were enlarged and were deeper and wider after treatment at 900°C

(Fig. 4.14c, d and Fig. 4.15c, d). This severity of attack at the carbides is because the diffusivity of hydrogen into the alloy (as well as the diffusivity of carbon out of the carbides) increases with increasing time and temperature. The volume fraction of bulky carbides, needle-shaped carbides, grains, attacked inner portion of bulky carbides and attacked interface between bulky carbides and grains of hydrogen treated Fe-16.2Al-0.4C alloy were estimated (Table 4.7) by stereological methods using the image-analysis program (Image-Pro Plus, version 4.1, Media Cybernetics, USA). The volume fraction of the attacked inner portion of bulky was increased to 0.025 after hydrogen treatment at 900°C for 144 h in comparison to 0.019 obtained at 700°C for 48 hours (Table 4.8). The attack at the interfaces between the bulky carbides and matrix was also more severe here than the previous cases of hydrogen treatment at lower temperature. The needle-shaped carbides were not observed in this case like the previous case of 48 hours treatment at 700°C. The tendency of spherodization of the bulky carbides was also noticed in this case (Fig. 4.14a, b and Fig. 4.15a, b). This is due to the higher temperature heat treatment of the alloy.

The SEM micrographs after hydrogen treatment at 900°C for 366 hours are shown in Figure 4.16. It is interesting to note that almost all the carbides did not show any kind of line attack or formation of fissure due to hydrogen treatment. The carbides were spherodized more in this case (Fig. 4.16a) and the growth of some of the carbides were noticed (Fig. 4.16b and c). The tendency of linking up of the carbides was also observed (Fig. 4.16a and b). The growth of bulky carbides must be due to the higher temperature (900°C) heat treatment for longer time (336 hours). As the kinetic parameters (temperature and time) were higher in this case, the diffusional process must also have been faster. However, the anticipated higher reaction rate between hydrogen and carbide was not observed. The degradation of the bulky carbides was less than in the shorter time of hydrogen treatment. The SEM micrographs (Fig. 4.16c and d) showed carbide coarsening, but practically no hydrogen attack occurred inside the carbides. However, it is evident from the Figure 4.16c and d that the dissolution of carbides at the interface between the bulky carbides and the matrix did occur. This could have resulted due to the higher edge length between the bulky carbides and matrix, than between three grains of matrix or between two grains and carbides (Table 4.5). As these edge lengths can act as

short cut diffusion paths for hydrogen at higher temperature, the hydrogen attack is more pronounced at the interface between the bulky carbides and grains. The probability of occurrence of bulky carbides is 3.5 times more likely on a grain triple point and two times more likely between two grains as compared to inside a grain (Table 4.6). As a result diffusion of carbon through the interfaces between the bulky carbides and the matrix was easier at the higher temperature of 900^0C. This may be a plausible cause of severe reaction observed at the interfaces of bulky carbides and matrix of the sample hydrogen treated at high temperature for longer time.

Figure 4.17 shows the SEM micrographs of hydrogen treated alloy at $900^\circ C$ for 720 hours. Similar to the case of hydrogen treatment at $900^\circ C$ for 366 hours, there was practically no visible degradation inside the carbides in the samples treated at $900^\circ C$ for 720 hours. The volume fraction of bulky carbide decreased to 0.151 (from 0.189 for the case of without hydrogen treatment, Table 4.8). The spherodization and growth of carbides was observed to be more than that of carbides of the sample treated at $900^\circ C$ for 366 hours (Fig. 4.16a and b). The linking up of the carbides was also evident in this case (Fig. 4.17b and c). The lower volume fraction of the carbides is due to the continuing process of carbide spherodization and ripening. This is illustrated by the micrograph in Figure 4.17b, where the growing carbides have been interconnected by the diffusional process. The process of pore closure was also observed clearly in Figure 4.17d, thereby further validating the ripening of the carbides at $900^\circ C$ for 720 hours.

It is clear from the SEM microstructural observation that the interface between blocky carbides and grains were mainly affected. The carbides are also effected. The degree of attack was increased as the kinetic parameters i.e. temperature and the time period were increased. However, at the higher temperature the attack of the bulky carbides was not evident for longer time (336 hours and 720 hours). This could probably be related to the nature of surface coverage of oxide formed at higher temperature for longer time. In order to understand this, the dissociation pressure of alumina at $700^\circ C$ and $900^\circ C$ was determined thermodynamically. The values of $\left(p_{O_2}\right)_{eqm}$ for the formation of alumina (Eqn. 4.11) on the surface of the samples hydrogen treated at $700^\circ C$ and $900^\circ C$ were compared with the ambient p_{O_2} of the system during the treatment in the following section.

110

$$1.33Al(s) + O_2(g) = 0.67Al_2O_3(s)$$

<div align="right">eqn. 4.11</div>

The Gibb's free energy (ΔG) required for the formation of 0.67 mole alumina (i.e. the mole of alumina formed by consuming 1 mole of oxygen) by the reaction stated above is $-1124800+217.87T$ J in the temperature range of 993K to 2327K [58, 59], where T is the reaction temperature in Kelvin. Therefore, the values of ΔG are -0.91×10^3 kJ and -0.89×10^3 kJ.

From Eqn. 4.9,

$$\Delta G_9 = RT \ln\left(p_{O_2}\right)_{eqm}$$

<div align="right">eqn. 4.12</div>

The values of $\left(p_{O_2}\right)_{eqm}$ computed were 1.36×10^{-50} atm. and 4.21×10^{-44} atm. at 700°C and 900°C, respectively. As these values are much less than the partial pressure of ambient oxygen during the hydrogen treatment, the formation of alumina on the surface of the samples hydrogen treated at 700°C and 900°C was thermodynamically feasible.

However, the oxide growth on the surface is also important and this is dictated by the kinetics. The longer time of exposure and higher the temperature of exposure would thicken the surface oxide scale. Thicker oxide scale hinders the hydrogen attack by minimizing hydrogen contact with metal surface, as the diffusivity of hydrogen in alumina is low [41]. It was therefore anticipated that the lower degree of hydrogen attack seen at higher temperature and longer time of exposure could be due to surface oxide formation. In order to verify this, the surface nature after hydrogen treatments are shown in Figure 4.18 through 4.20 for all the treatments carried out. It can be observed that thicker oxide layer covered the surfaces of the samples after hydrogen treatment at higher temperature for longer time. Therefore, the lower degree of hydrogen attack is concluded to be due to surface oxide formation at higher temperature for longer time of exposure.
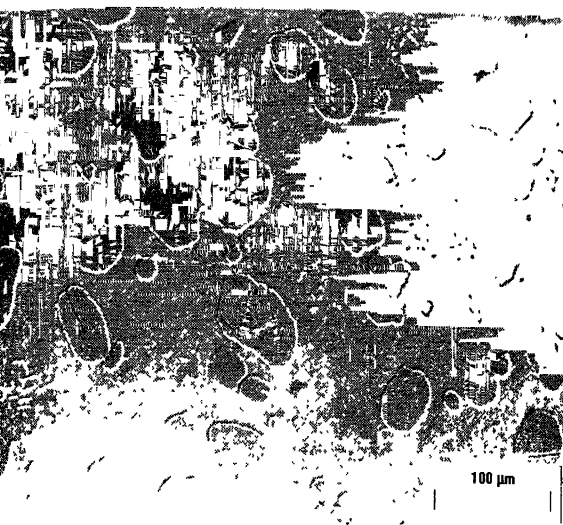
(a)
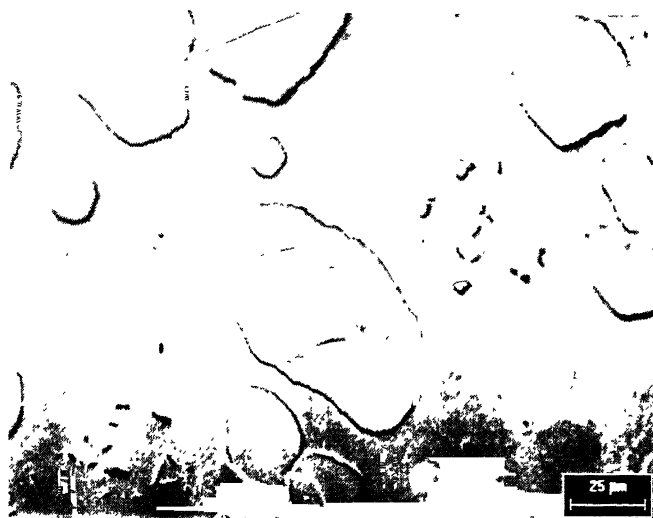
(b)
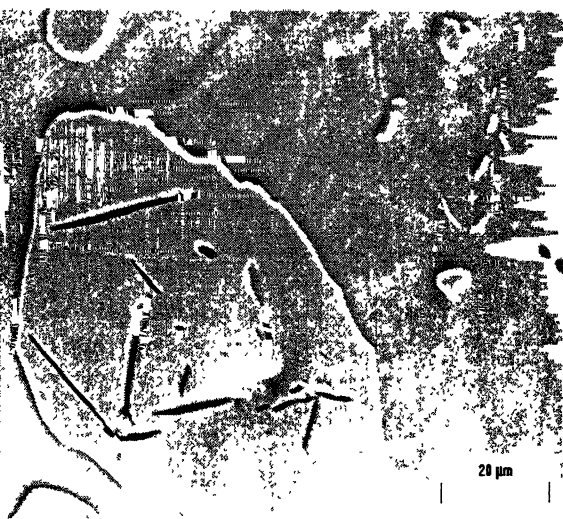
(c)

(d)

Figure 4.12   SEM micrograph showing the hydrogen attack after hydrogen treatment at
700°C for 10 hours

(a)

(b)

(c)
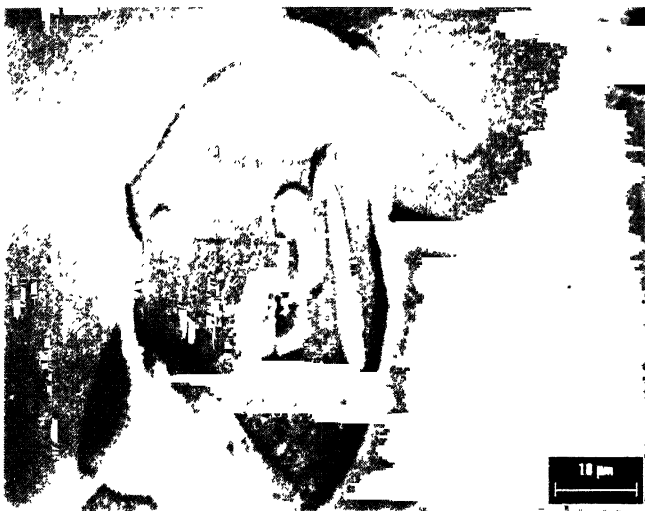
(d)

Figure 4.13   SEM micrograph showing the hydrogen attack after hydrogen treatment at
700°C for 48 hours

113
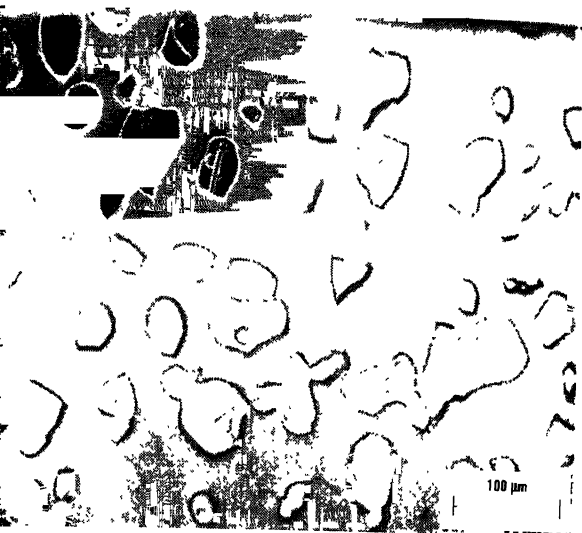
(a)

(b)
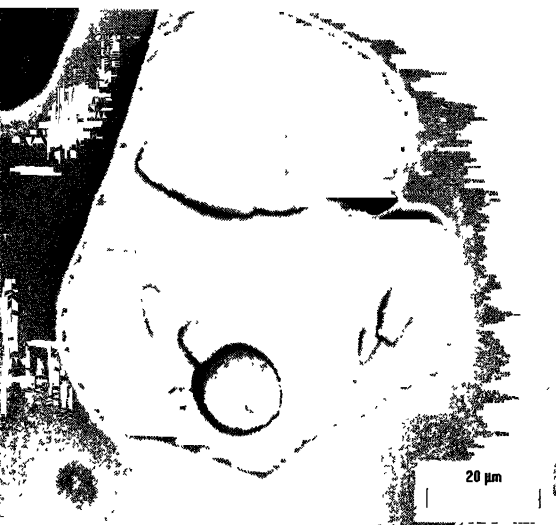
(c)
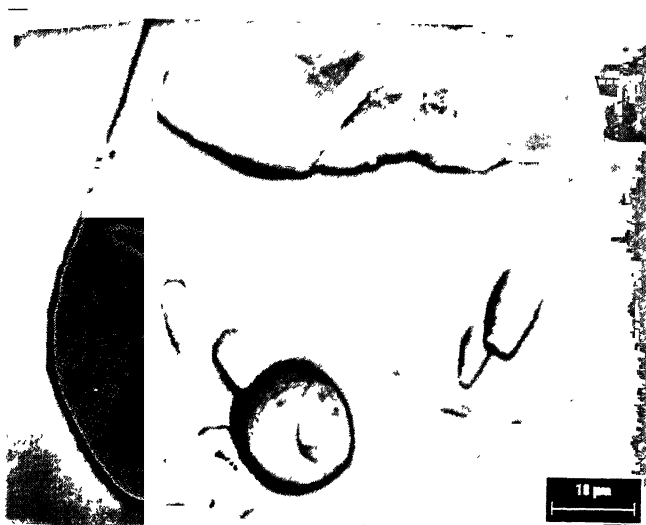
(d)

Figure 4.14   SEM micrograph showing the hydrogen attack after hydrogen treatment at
900°C for 144 hours

114

(a)

(b)
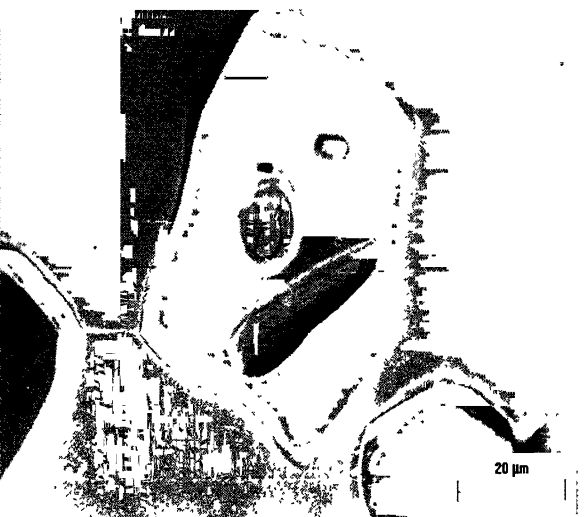
(c)

(d)

Figure 4.15   SEM micrograph showing the hydrogen attack after hydrogen treatment at
900°C for 144 hours (duplicate experiment)
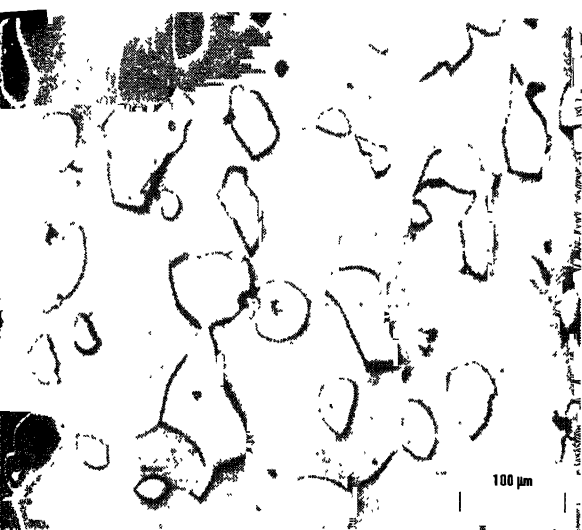
(a)

(b)
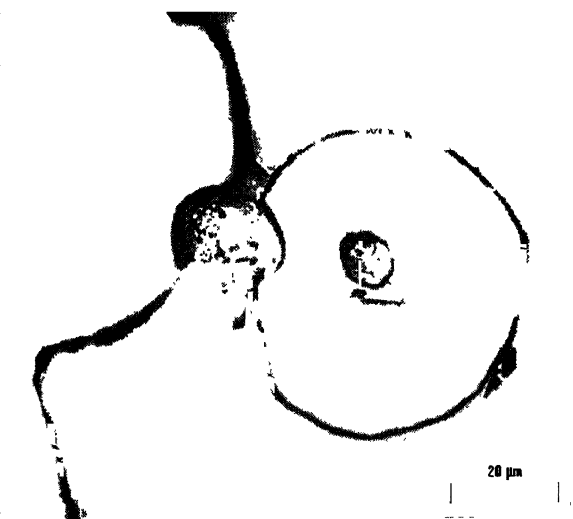
(c)
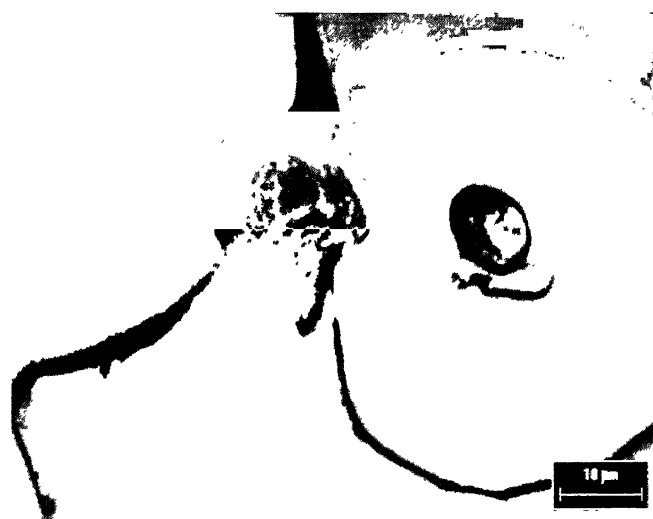
(d)

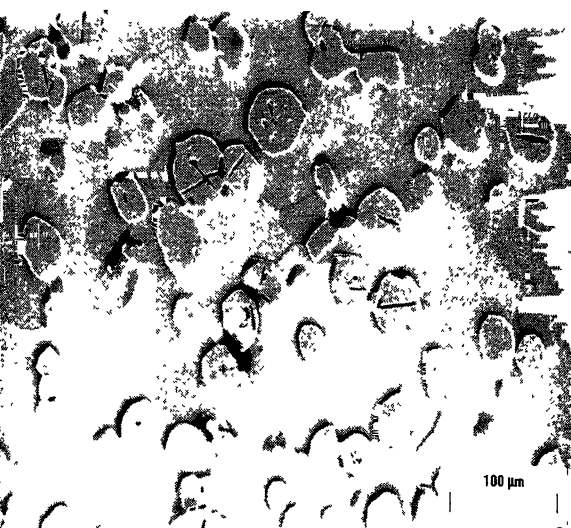Figure 4.16   SEM micrograph showing the hydrogen attack after hydrogen treatment at
900°C for 336 hours

116
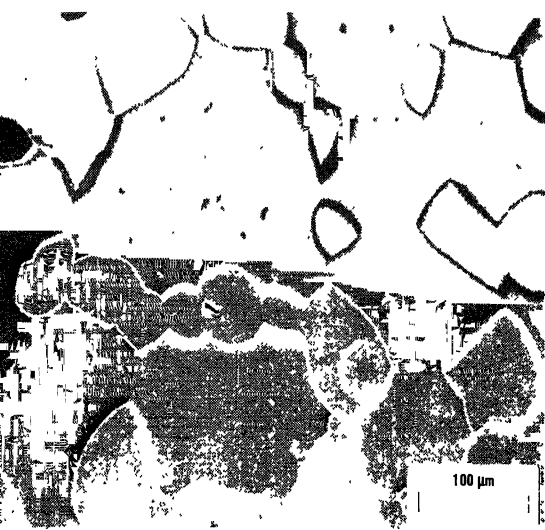
(a)

(b)

(c)
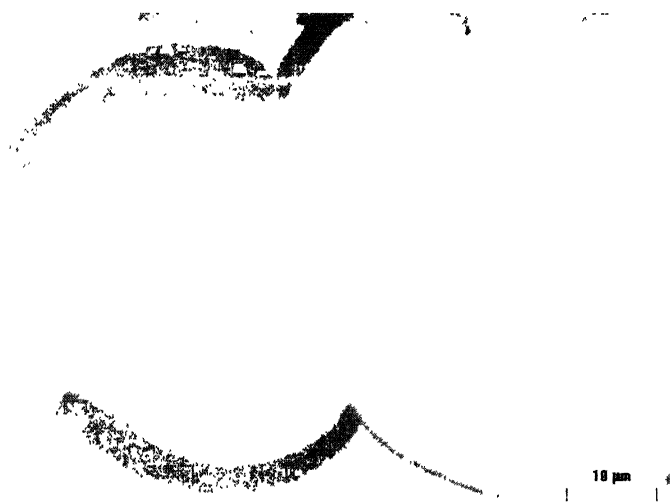
(d)

Figure 4.17   SEM micrograph showing the hydrogen attack after hydrogen treatment at
900°C for 720 hours

Table 4.9   The comparative volume fraction data of bulky carbides, needle-shaped carbides, grains and attacked inner portion of bulky carbides of hydrogen treated Fe-16.2Al-0.4C alloy

Treatment		Bulky carbides		Needle-shaped carbides		Grains		Attacked inner portion of bulky carbides	
Temp (°C)	Time (h)	Mean	Error, ±	Mean	Error, ±	Mean	Error, ±	Mean	Error, ±
Without treatment		0.189	0.038	0.016	0.149	0.795	-	-	-
700	10	0.187	0.021	-	-	0.810	-	0.003	0.612
700	48	0.169	0.016	-	-	0.812	-	0.019	0.391
900	144	0.165	0.041	-	-	0.808	-	0.025	0.225
900	144	0.167	0.051	-	-	0.806	-	0.024	0.401
900	720	0.158	0.019	-	-	0.829	-	-	-
900	336	0.151	0.013	-	-	0.830	-	-	-

15.0KV   100μm
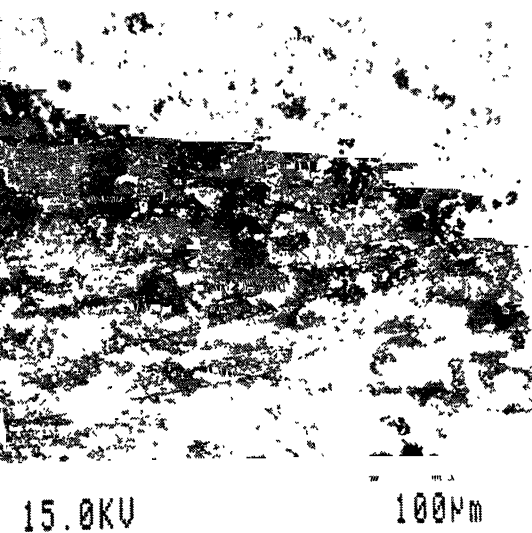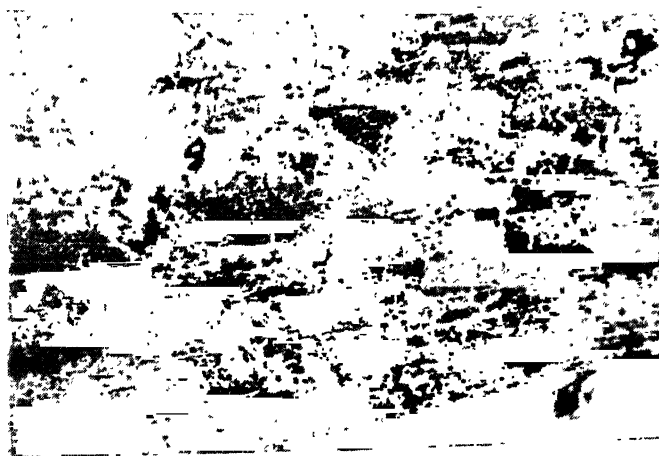
(a)   (b)
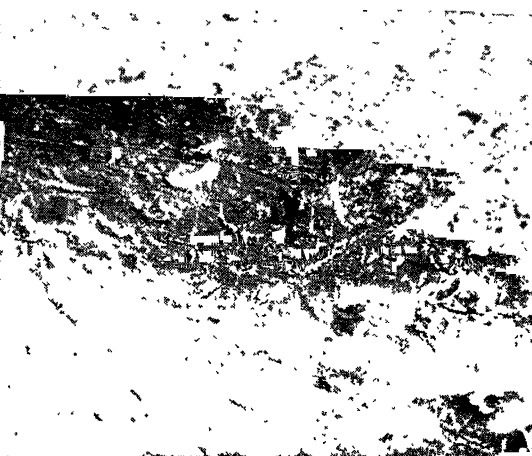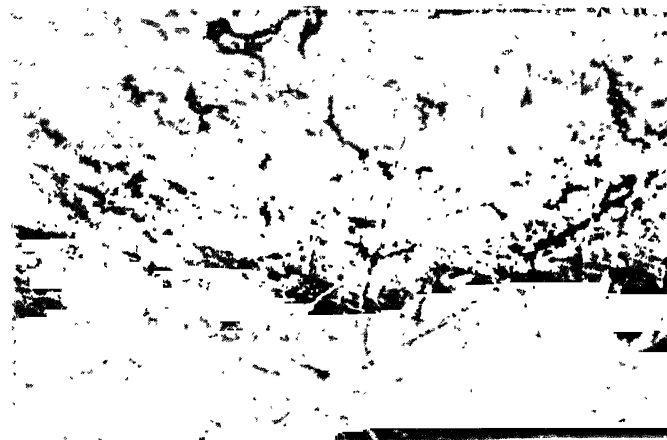
(c)   (d)

Figure 4.18   EPMA micrographs showing the oxide layer on the surfaces of the hydrogen treated samples at (a), (b) at 700°C for 10 h, and (c), (d) 700°C for 48 h
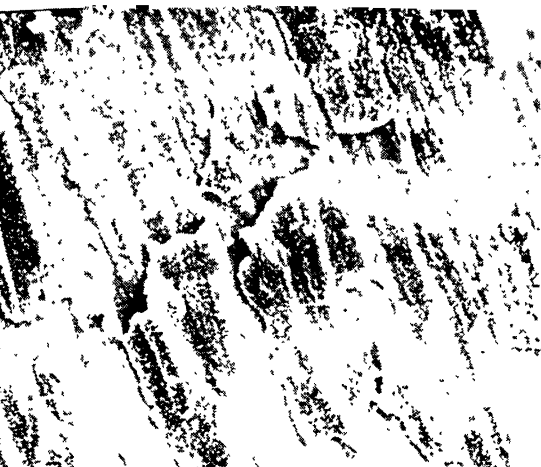
(a)
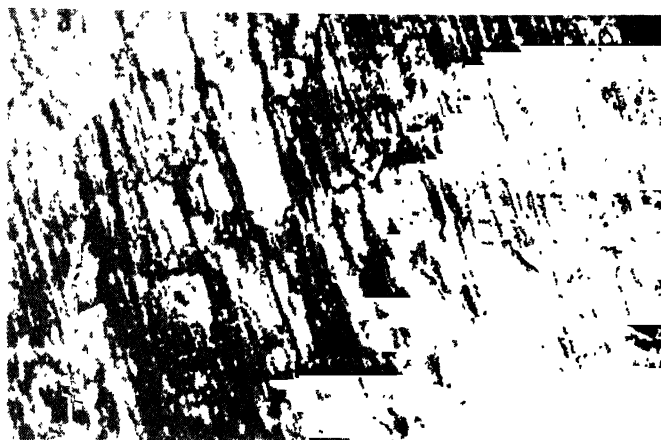
(b)
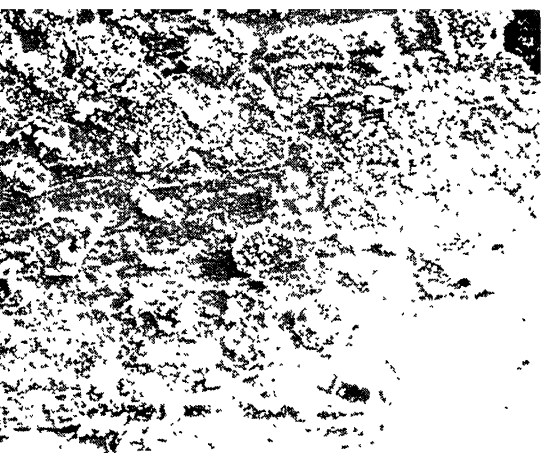
(c)
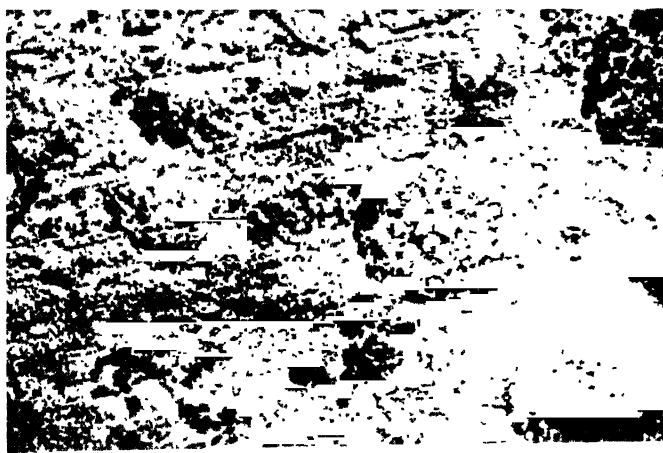
(d)

Figure 4.19   EPMA micrographs showing the oxide layer on the surfaces of the
hydrogen treated samples at (a), (b) at 900°C for 144 h, and (c), (d) 900°C
for 144 h (duplicate experiment)
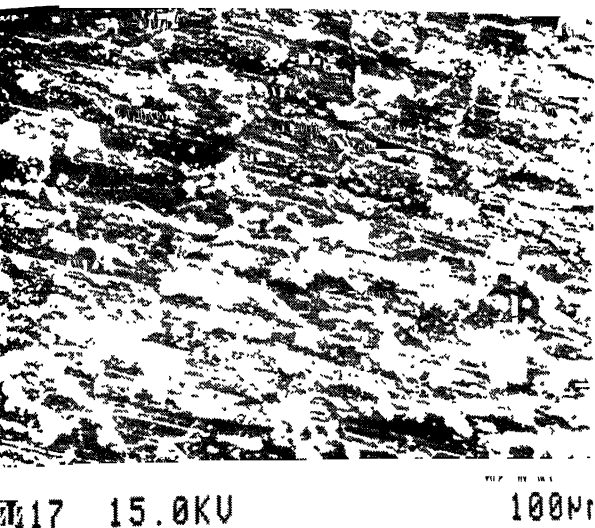
(a)
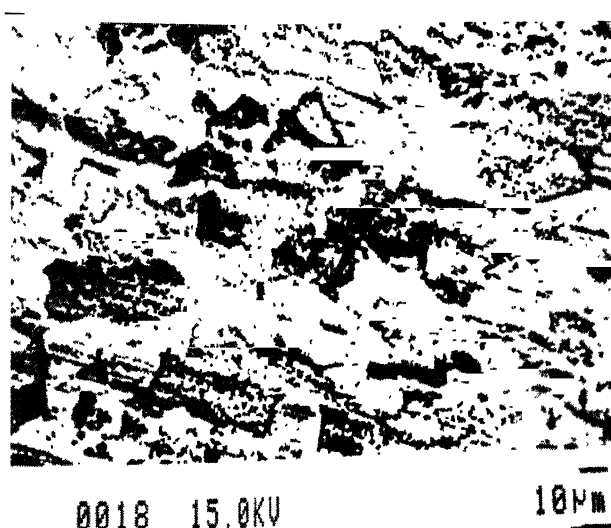
(b)
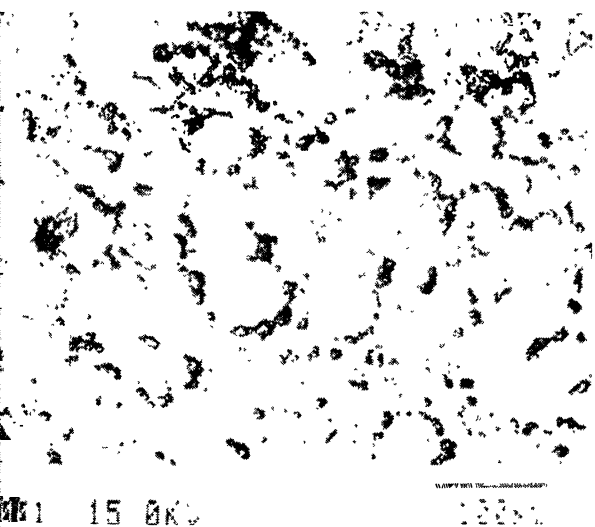
(c)
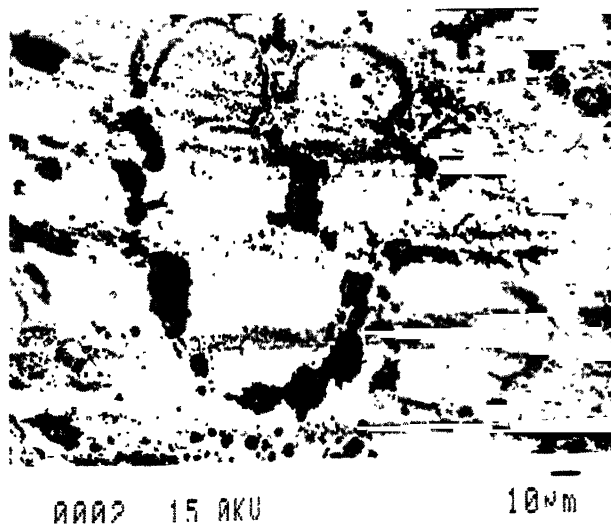
(d)

Figure 4.20   EPMA micrographs showing the oxide layer on the surfaces of the
hydrogen treated samples at (a), (b) at 900°C for 336 h, and (c), (d) 900°C
for 720 h

4.3. Electrochemical behavior

The electrochemical behavior of the as-received Fe-16.2Al-0.54C alloy was studied using different normalities of H_2SO_4 solution as electrolyte. In order to understand the effect of dissolved hydrogen on the electrochemical behavior of the alloy, potentiodynamic polarization experiments were carried out on all the hydrogen treated samples. The potentiodynamic polarization behavior of the as-received material as well as that of hydrogen treated samples will be discussed below.

4.3.1. Effect of pH

The following discussion focuses attention on the potentiodynamic polarization behavior of carbon-alloyed iron aluminide in acidic medium. This study was undertaken after it was reported by Rao et al. [52] that oxidation of hydrogen was indicated by by a second anodic peak in the potentiodynamic polarization diagrams in carbon-alloyed iron aluminides.

In order to understand the effect of H^+ ion concentration on the potentiodynamic polarization behavior, experiments were carried out on Fe-16.2Al-0.54C alloy in freely aerated H_2SO_4 solutions with normalities ranging between 0.1 N to 1.0 N. The polarization experiments were conducted at a scan rate of 0.5 mV/sec using Ag/AgCl in saturated KCl as the reference electrode and platinum as the counter electrode. All the experiments were carried out after polishing the samples to a 4/0 finish. Extra care was taken during the metallography of the hydrogen treated samples so that only the surface oxide layer was removed. The free corrosion potential of the samples was allowed to stabilize in the electrolytic solution before conducting the potentiodynamic polarization experiment.

A typical stabilization of free corrosion potential (FCP) versus time for the alloy is shown in Figure 4.21. The nature of free corrosion potential curve (movement from active to noble direction) indicated progressive surface film formation on immersion. However, the nature of the potentiodynamic polarization curves after potential stabilization did not coincide with that determined by *Rao et al.* It was determined that the results matched those of Rao *et al.* when the experiments were conducted immediately on immersion. Therefore all the potentiodynamic polarization experiments

were conducted immediately on immersion of the samples. In order to understand the effect of dissolved hydrogen on the secondary anodic peak, the potentiodynamic polarization experiments were carried out in 0.5 N H_2SO_4 for the hydrogen treated samples.

Figure 4.22 shows the potentiodynamic polarization behavior of the alloy at different normalities of H_2SO_4. The corrosion rate (i_{corr}) and Tafel slopes (β_c and β_a) at different normalities of H_2SO_4 solution were determined from the potentiodynamic polarization curves (Figure 4.22) of Fe-16.2Al-0.54C alloy and are tabulated in Table 4.11. The β_c and β_a values were almost similar for the polarization experiments carried out in different normalities of H_2SO_4. The β_c values varied in the range of –0.242 to -0.264 V/decade, whereas the β_a values were in the range of 0.174 to 0.196 V/decade. However, the corrosion rate (i_{corr}) increased continuously and systematically (from 0.41 mAcm^{-2} for 0.1 N to 6.31 mAcm^{-2} for 1.0 N) as the normality of the H_2SO_4 was increased from 0.1 N to 1.0 N. The concentration of H^+ ion increased with increasing normality. The rate of cathodic reaction (hydrogen evolution reaction) must be higher with higher H^+ ion concentration. The anodic reaction rate (dissolution of matrix) was increased due to the greater concentration of H^+ available with increasing normality. Thus, the corrosion rate i.e. the corrosion current density, increased with normality.

The potentiodynamic polarization curves, obtained as a function of solution normality (Figure 4.22) showed active-passive behavior. Notably, the anodic polarization curves of the alloy exhibited a secondary anodic peak in the range of –45 mV to –92 mV, with respect to Ag-AgCl standard electrode, before reaching the broad passive zone of constant passive current density. It is important to note that the secondary anodic peak was observed for all the normalities of the solution used. The first anodic peak was observed in the range between –238 mV to –393 mV for different normalities of H_2SO_4 solution. In the passive region, the passive current density was constant in solutions of different normalities, thereby proving the similar nature of the passive film on the surface of the alloy as a function of potential.

The values of zero current potential (ZCP), complete passivation potential (E_{cp}), breakdown potential (E_{bp}) and passive current density (i_{pass}) were obtained from the potentiodynamic polarization curves (Figure 4.22) and these are also summarized in

Table 4.11. The ZCP, E_{cp} and E_{bp} were almost constant for the experiments in different normalities. However, i_{pass} generally increased with increasing normality of H_2SO_4. The value of i_{pass} in case of 0.2 N H_2SO_4 was slightly more than that in case of 0.3 N H_2SO_4, the reason for which could not be understood. The increasing passive current density with decreasing pH has been well recognized [25]. The value of $E_{rev(H^+/H_2)}$ increases with the decrease in pH of the solution. As the current density is exponentially proportional to the value of $E_{rev(H^+/H_2)}$, therefore, the current density increases with increase in H^+ concentration.

In order to obtain some insights on the reduction reaction in the polarization diagram, the ZCP can be compared with the reversible potential for hydrogen evolution reaction. Table 4.11 indicates that the ZCP values of the alloy were in the order of –540 mV vs SSC. The reversible electrode potential E_{rev} for hydrogen evolution reaction (equation 4.1) is given by the Nernst equation as in Equation 4.2.

$$2H^+ + 2e^- \Leftrightarrow H_2 \qquad \text{Eqn. 4.13}$$

$$E_{rev} = E^o_{H^+/H_2} - 0.059\,pH \qquad \text{Eqn. 4.14}$$

where $E^0_{H^+/H_2}$ denotes the standard potential of hydrogen evolution. The pH of 0.1 N to 1.0 N sulfuric acid solution varied in the range of 1.68 to 1.24. The potential of the Ag/AgCl standard electrode is 0.197 mV with respect to the SHE. The equilibrium reversible potential for the hydrogen evolution reaction was calculated as –296 mV and –270 mV vs SSC for pH of 1.68 and 1.24, respectively. As the ZCP values were moderately active compared to this value, hydrogen evolution can be considered to be the dominating cathodic reaction.

Analysis of the transpassive region can also be undertaken. The transpassive potential (E_{tp}) for the samples were compared with the equilibrium potential for the oxygen evolution reaction. The equilibrium reaction for oxygen evolution and the corresponding E_{rev} for the reaction are given below.

$$\tfrac{1}{2}O_2 + 2H^+ + 2e \Leftrightarrow H_2O \qquad \text{Eqn. 4.15}$$

$$E_{rev} = E^o_{O_2/H_2O} - 2 \times 0.059\, pH\, (SHE) \qquad \text{Eqn. 4.16}$$

Utilizing the value of pH and $E^0_{O_2/H_2O}$ (1229 mV at 0 pH Vs. SHE), the E_{rev} was calculated

for the above reaction as +1030 mV (pH=1.68) and 1082 mV (pH=1.24) vs SSC. As these reversible potentials were clearly active compared to the transpassive potential (E_{tp}) the gas evolved in the transpassive region on the sample was oxygen.

It was reported earlier by Rao $et\ al.$ [52] that the potentiodynamic polarization curves for iron aluminide alloys (Fe-15.6Al-0.05C, Fe-15.6 Al-0.14C, Fe-15.6Al-0.5C-Fe-15.6Al-1C in wt %) showed an extra anodic peak in addition to the critical passivation peak. The same nature of the potentiodynamic polarization curves was also observed for as-received Fe-16.2Al-0.54C as well as for hydrogen treated samples of same composition in the present study. The primary passivation potentials and critical current densities were calculated for both the peaks as E_{pp1}, E_{pp2} and i_{crit1} and i_{crit2}, respectively and tabulated in Table 4.11. The subscript 1 denotes the most active peak and the subscript 2 denotes the nobler peak (i.e. the extra anodic peak). The values of E_{pp1} and E_{pp2} were almost similar for different normalities. Although the values of i_{crit1} exhibited an increase with normalities for some cases (i.e. when 0.4 N H_2SO_4 was used as the electrolyte instead of 0.3 N H_2SO_4), it did not display a general trend of increase with increase in normality of H_2SO_4. On the other hand, the i_{crit2} values increased with increase in normality of H_2SO_4. As can be noticed in the polarization diagram, a larger amount of hydrogen was reduced when the specimen was polarized in the cathodic region with increasing H^+ concentration in electrolyte. Therefore, the increasing i_{crit2} for the second anodic peak can be understood by the larger amount of hydrogen available for oxidation in solutions of lower pH.

The exchange current density for hydrogen equilibrium ($i_{0_{H^+/H_2}}$) was calculated by

extending the cathodic Tafel slope and intersecting it with the parallel line to log (i) axis at the $E^{rev}_{H^+/H_2}$ potential. These have been also tabulated in Table 4.11. It is evident from

Table 4.11 that the $i_{0_{H^+/H_2}}$ values increased with increasing normality of H_2SO_4.

Therefore, one reason for the increased corrosion rate with H^+ concentration, is the

increasing $i_{0_{H^+/H_2}}$ with H^+ concentration while not affecting the β_c slope. The exchange current density on the iron aluminide (Fe-16.2Al-0.54C) studied in the present case is comparable to that on the other iron aluminides studied by Rao *et al.* [52]. However, it was an order of magnitude more than that on iron and by several order of magnitudes higher than Al. The increased hydrogen reaction kinetics must be related to the presence of carbides in the microstructure of the iron aluminides. An indirect indication for the same is the highest exchange current density noted for the iron aluminide with highest carbon content.

4.3.2. Effect of hydrogen treatment

Potentiodynamic polarization experiments were carried out on hydrogen treated samples in 0.5 N H_2SO_4 solution in order to study whether hydrogen treatment had any effect on the secondary anodic peak. The normality of the electrolyte was chosen as 0.5 N H_2SO_4 for these studies. The β_c, β_a and i_{corr} values, determined from the potentiodynamic polarization curves (Figure 4.23), were almost similar for all the samples (Table 4.12). Therefore dissolved hydrogen did not have any effect on corrosion rate. This is reasonable because corrosion rate is determined by the normality of the electrolyte, as seen earlier during the potentiodynamic polarization study of as-received Fe-16.2Al-0.54C alloy using H_2SO_4 solution of different normalities.

The parameters from the potentiodynamic polarization study (ZCP, E_{pp1}, E_{pp2}, E_{cp}, E_b, E_b- E_{cp}, i_{crit1}, i_{crit2}, i_{pass} and $i_{0_{H^+/H_2}}$) are tabulated in Table 4.13. The i_{crit1} values did not exhibit any change with the change in kinetic parameters (i.e. with increase in hydrogen treatment temperature and time). Although there was no significant change in the values of i_{crit2}, the values apparently appeared to be increased with treatment temperature and time.

Although Frangini *et al.* [53] did not report the existence of secondary anodic peak in iron aluminide alloys (hot rolled commercial Fe-Al containing 24.4 wt % Al), Hermas *et al.* [54] agreed with the existence of secondary anodic peak in AISI 304 austenitic stainless steel. According to them re-oxidation of absorbed hydrogen atoms on stainless steel surface was considered a strong reason for the appearance of secondary

anodic peak in acid solution. Rao et al. [52] also exhibited the similar behavior of iron aluminide alloys (Fe-15.6Al-0.05C, Fe-15.6 Al-0.14C, Fe-15.6Al-0.5C-Fe-15.6Al-1C in wt %) in 0.5 N H_2SO_4 (Figure 4.24) solution where the i_{crit2} values were increased with increase in the hydrogen charging time.

It can be seen from the Figure 4.23 that with increase in hydrogen treatment temperature and time (from 700°C, 10 hours to 900°C, 720 hours) the secondary anodic peak of Fe-16.2Al-0.54c was shifted to higher anodic current density (from 4.36 mA/cm^2 to 6.98 mA/cm^2, Table 4.12). This secondary anodic peak may be attributed to the oxidation of hydrogen atom formed due to the cathodic reaction on the surface of the sample under potentiodynamic polarization study. It can be observed from the cathodic part of the potentiodynamic polarization (Figure 4.23) that the evolution of hydrogen on the surface of the samples increased with increase in treatment temperature and time, thereby, the secondary anodic peak also showed an increase with increase in treatment temperature and time. The hydrogen dissolved during the treatment did not play any role on the secondary anodic peak.

The ZCP, E_{pp1}, and E_{pp2} values of the hydrogen treated samples polarized in 0.5 N H_2SO_4 were similar to the values of as-received samples polarized in 0.1 N to 1.0 N H_2SO_4. However, the E_{cp} values decreases with treatment temperature and time, whereas E_b values showed a gradual increase with increase in kinetic parameters during the hydrogen treatment. Therefore, the passivation ranges of the hydrogen treated Fe-16.2Al-0.54C samples were increased with increase in treatment temperature and time. The i_{pass} values were also increased with increasing treatment temperature and time allowed for hydrogen diffusion. This increase in the passivation ranges and i_{pass} values are manifestation of the passive film that forms on the surface during polarization. It appeared that the surface cerated after high temperature hydrogen treatment for longer time increased the passivation range i.e. the surface layer provided resistance to pitting or transpassivity. However, the film is not very protective because higher i_{pass} values of the samples hydrogen treated at higher temperature and for longer time indicates more defective film possibly due to the surface created. The increase in the passivation ranges and i_{pass} values attributed to some changes in the surface property of the samples due to

the different hydrogen treatments. The change in surface property was confirmed by the change in hardness of the carbides and matrix, which is discussed below in detail.

4.3.3. Surface roughness

One possible reason for the change in passive film nature could be the surface finish of the hydrogen treated Fe-16.2al-0.54C samples. It is well known that passive films formed on smooth polished surfaces are superior compared to those on rough surfaces [25, 63]. Microstructural study of the hydrogen treated samples indicated surface roughening with increasing treatment time and temperature. This roughening was due to the modifications in surface created due to hydrogen treatment and high temperature treatment (oxidation at higher temperature).

In order to understand the effect of surface roughness, potentiodynamic polarization experiments were carried out on the as-received samples for a mirror polished surface (after cloth polishing using 1 μm alumina powder) and for a rough surface (after wheel grinding). Figure 4.24 shows the potentiodynamic polarization curves for both these surface finishes in 0.5 N H_2SO_4 solution. The corrosion rates (i_{corr}), Tafel slopes (β_c and β_a) and the passivation parameters (ZCP, E_{pp1}, E_{pp2}, E_{cp}, E_b, E_b- E_{cp}, i_{crit1}, i_{crit2}, i_{pass} and $i_{0_{H^+/H_2}}$) were determined from the potentiodynamic polarization curves and are tabulated in Table 4.15 and 4.16, respectively. Interestingly, the passivation ranges of the samples with different degree of surface roughness did not differ much. There appeared to be an apparent decrease in i_{pass} with increasing roughness, although the decrease was not significant. Therefore, the increase in the passivation ranges and i_{pass} values of hydrogen treated samples with increasing treatment temperature and time can not be attributed to the surface roughness induced by the high temperature hydrogen treatment.

4.3.4. Microhardness characterization

As surface finish was discounted as the reason for the observation differences in the polarization behaviour of the alloy, it was decided to explore the possibility of change in surface compositions causing these observed differences. In view of lack of precise

compositional profiling facilities, it was decided to understand compositional change by an indirect method. Compositional changes result in change in mechanical behavior and this must show up by microhardness testing. Moreover, a sample area could be sampled so as to obtain statistically meaningful results for comparison purposes.

The microhardness of the blocky carbides and grains were measured for as-received Fe-16.2Al-0.54C alloy as well as for the hydrogen treated samples in order to establish the effect of surface property on passivation range and i_{pass} value. Hardness measurements of needle-shaped carbides were not possible because proper indentations could not be made due to the small size of these carbides and moreover, they dissolved rather quickly upon high temperature hydrogen treatment. A 50-gram load was applied during the measurement of hardness as this provided optimum size of the indentation. If the size of the indentation is too small, then the measurement error of the diagonal will be high. On the other hand, if a higher load is applied in order to make the indentation, the indentation mark could overlap some nearby phase. Table 4.15 reports hardness for the bulky carbides while Table 4.16 reports that for the matrix as a function of hydrogen treatment. It is observed from Table 4.15 that the carbides of the sample, which was treated at 900°C for 720 hours, exhibited the lowest hardness. Two duplicate samples treated at 900°C for 144 h exhibited almost similar hardness. The carbides in the sample treated at 700°C were not significantly affected by the hydrogen treatment. The hardness of the carbides decreased with increasing temperature and time of hydrogen treatment. The hardness of the carbide could probably have decreased due to interaction with hydrogen and with oxygen at high temperature. Hydrogen interaction with carbide results in depletion of carbon from the carbides while oxygen interaction with carbide depleted the carbide of Al. this has been discussed earlier. Therefore, the change in carbide composition with hydrogen treatment is indirectly confirmed.

The hardness data of matrix (Table 4.16) also exhibited a similar behaviour like that of the carbides, i.e. decreasing hardness with increasing time and temperature. However, the rate of decrease of hardness with increasing treatment temperature and time was lower compared to the carbides. The decrease in hardness of the matrix could probably be due to the decurburization from matrix. The carbon could have either

diffused to the bulky carbide precipitates or reacted with the ambient environment. The lower matrix hardness also indicates compositional changes.
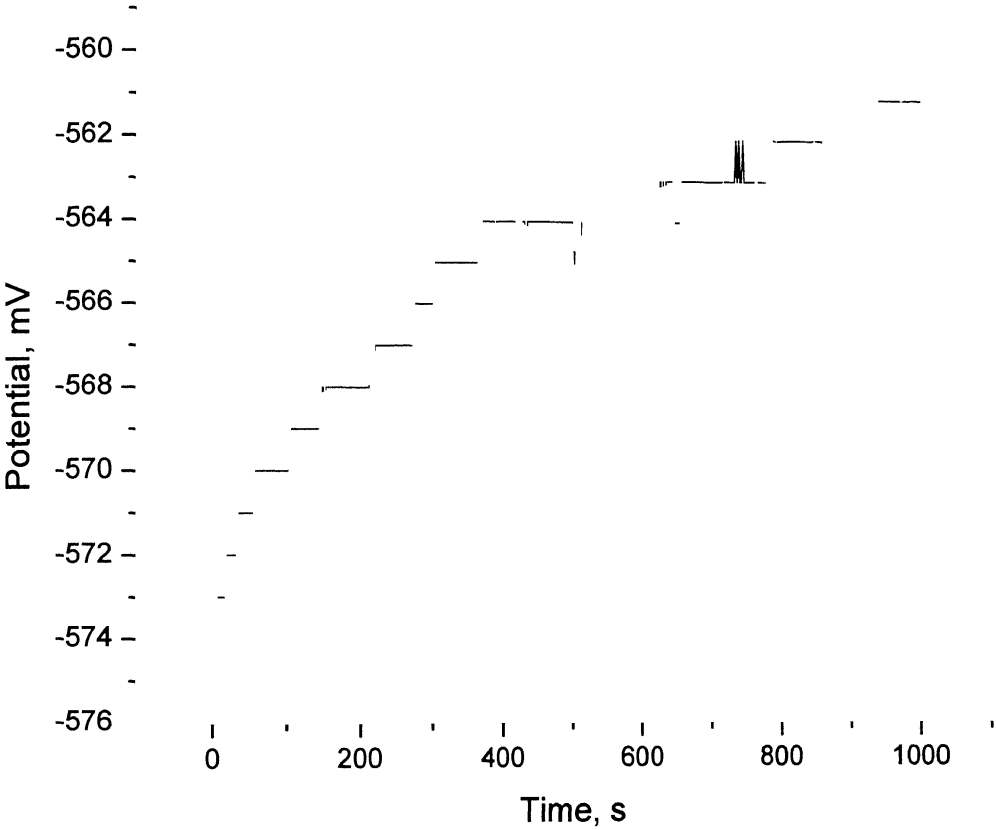
Figure 4.21   Free current potential Stabilization curve for as-received Fe-16.2Al-0.54C alloy
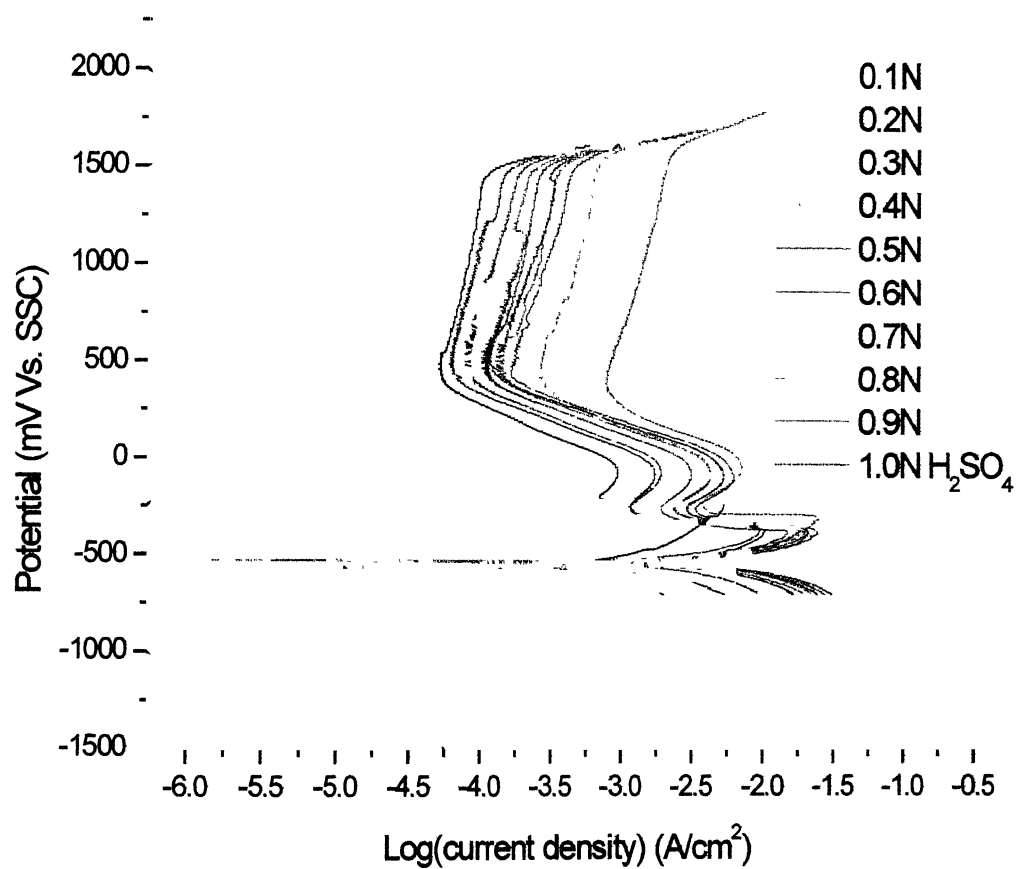
Figure 4.22   Potentiodynamic polarization behavior of as-received Fe-16.2Al-0.54C
(wt%) samples in 0.1 N to 1.0 N H_2SO_4 solution

Table 4.10　　Values of β_a, β_c and i_{corr} obtained from the potentiodynamic polarization curves of Fe-16.2Al-0.54C alloy studied in increasing normality of H_2SO_4

Normality of H_2SO_4 (N)	β_c (V/decade)	β_a (V/decade)	i_{corr} (mA/cm^2)
0.1	-0.254	0.182	0.41
0.2	-0.245	0.190	2.24
0.3	-0.316	0.188	1.90
0.4	-0.242	0.187	3.42
0.5	-0.247	0.190	4.13
0.6	-0.248	0.174	5.12
0.7	-0.252	0.190	5.29
0.8	-0.251	0.189	6.17
0.9	-0.262	0.160	6.31
1.0	-0.264	0.196	6.31

Table 4.11　　Values of the passivation parameters obtained from the potentiodynamic polarization curves of Fe-16.2Al-0.54C alloy studied in increasing normality of H_2SO_4

H_2SO_4 N	ZCP	E_{pp1}	E_{pp2}	E_{cp}	E_b	E_b-E_{cp}	i_{crit1}	i_{crit2}	i_{pass}	$i_{0_{H^+/H_2}}$
			mV					mA/cm^2		
1 N	-554	-238	-65.6	439	1420	981	5.25	0.98	0.051	0.09 X 10^{-2}
2 N	-543	-362	-63.7	493	1460	967	9.55	1.86	0.080	1.61 X 10^{-2}
3 N	-560	-357	-56.7	478	1430	952	7.94	1.35	0.060	3.31 X 10^{-2}
4 N	-544	-364	-59.3	497	1470	973	14.79	3.09	0.100	2.50 X 10^{-2}
5 N	-535	-370	-65.6	501	1480	979	18.20	4.36	0.132	2.95 X 10^{-2}
6 N	-535	-385	-78.9	517	1470	953	21.88	5.37	0.110	4.68 X 10^{-2}
7 N	-544	-393	-66.5	482	1490	1008	21.38	5.25	0.134	4.68 X 10^{-2}
8 N	-522	-385	-92.3	437	1490	1053	22.51	6.03	0.162	5.50 X 10^{-2}
9 N	-537	-375	-59.3	439	1520	1081	19.50	4.47	0.250	5.62 X 10^{-2}
0 N	-546	-320	-45.4	431	1550	1119	22.13	7.08	0.776	6.16 X 10^{-2}
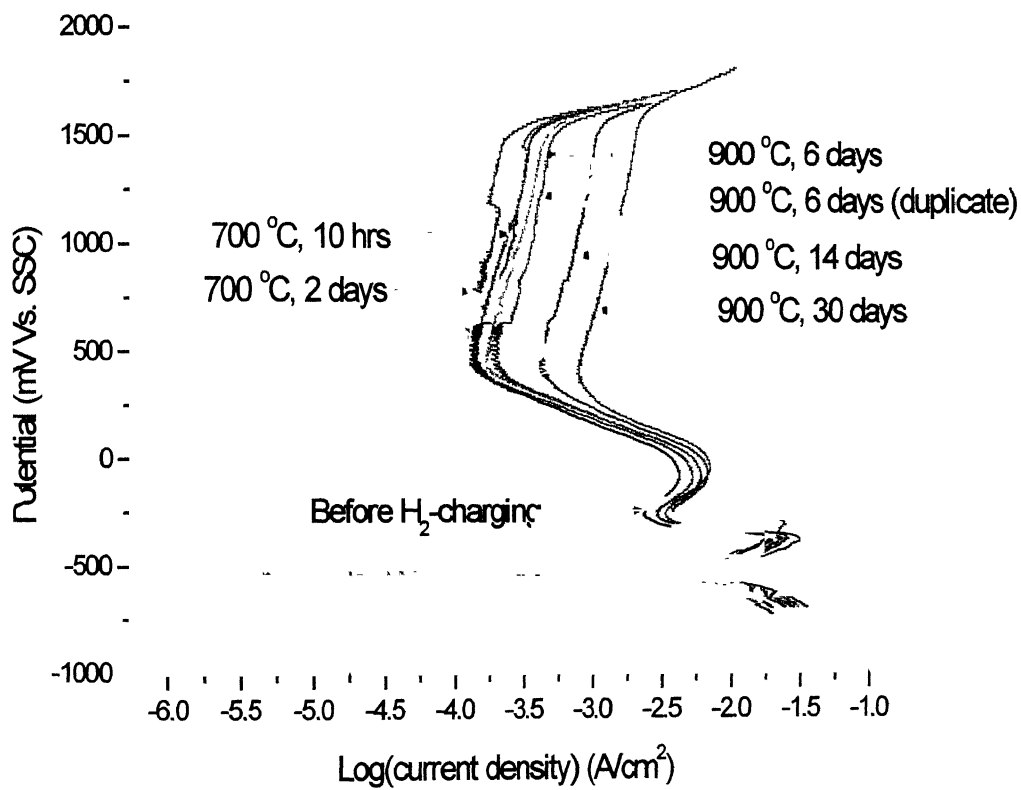
Figure 4.23 Potentiodynamic polarization behavior of hydrogen treated Fe-16.2Al-0.54C (wt%) samples in 0.5 N H$_2$SO$_4$ solution

Table 4.12   Values of β_a, β_c and i_{corr} obtained from the potentiodynamic polarization curves of hydrogen treated Fe-16.2Al-0.54C samples studied in 0.5 N H_2SO_4

Sample		β_c	β_a	i_{corr}
Temp. (°C)	Time (h)	(V/decade)	(V/decade)	(mA/cm²)
Without treatment		-0.247	0.190	4.13
700	10	-0.248	0.172	5.15
700	48	-0.250	0.187	5.25
900	144	-0.249	0.190	5.99
900	144	-0.246	0.184	5.76
900	336	-0.251	0.189	6.21
900	720	-0.255	0.193	6.29

Table 4.13   Values of the passivation parameters obtained from the potentiodynamic polarization curves of hydrogen treated Fe-16.2Al-0.54C samples studied in 0.5 N H_2SO_4

Sample		ZCP	E_{pp1}	E_{pp2}	E_{cp}	E_b	E_b-E_{cp}	i_{crit1}	i_{crit2}	i_{pass}	$i_{0_{H^+/H_2}}$
Temp. (°C)	Time (h)				mV					mA/cm²	
Without treatment		-535	-370	-65.6	501	1480	979	18.20	4.36	0.132	2.95×10^{-2}
700	10	-535	-382	-75.9	516	1470	954	21.85	5.37	0.108	3.09×10^{-2}
700	48	-542	-391	-66.6	485	1480	995	21.37	5.24	0.137	3.55×10^{-2}
900	144	-535	-385	-92.2	435	1490	1055	23.89	5.99	0.162	4.98×10^{-2}
900	144	-542	-385	-92.5	436	1490	1054	23.91	5.81	0.191	5.11×10^{-2}
900	336	-535	-390	-72.3	441	1520	1079	26.12	6.34	0.434	5.75×10^{-2}
900	720	-546	-321	-43.4	432	1550	1118	20.87	6.98	0.767	6.15×10^{-2}
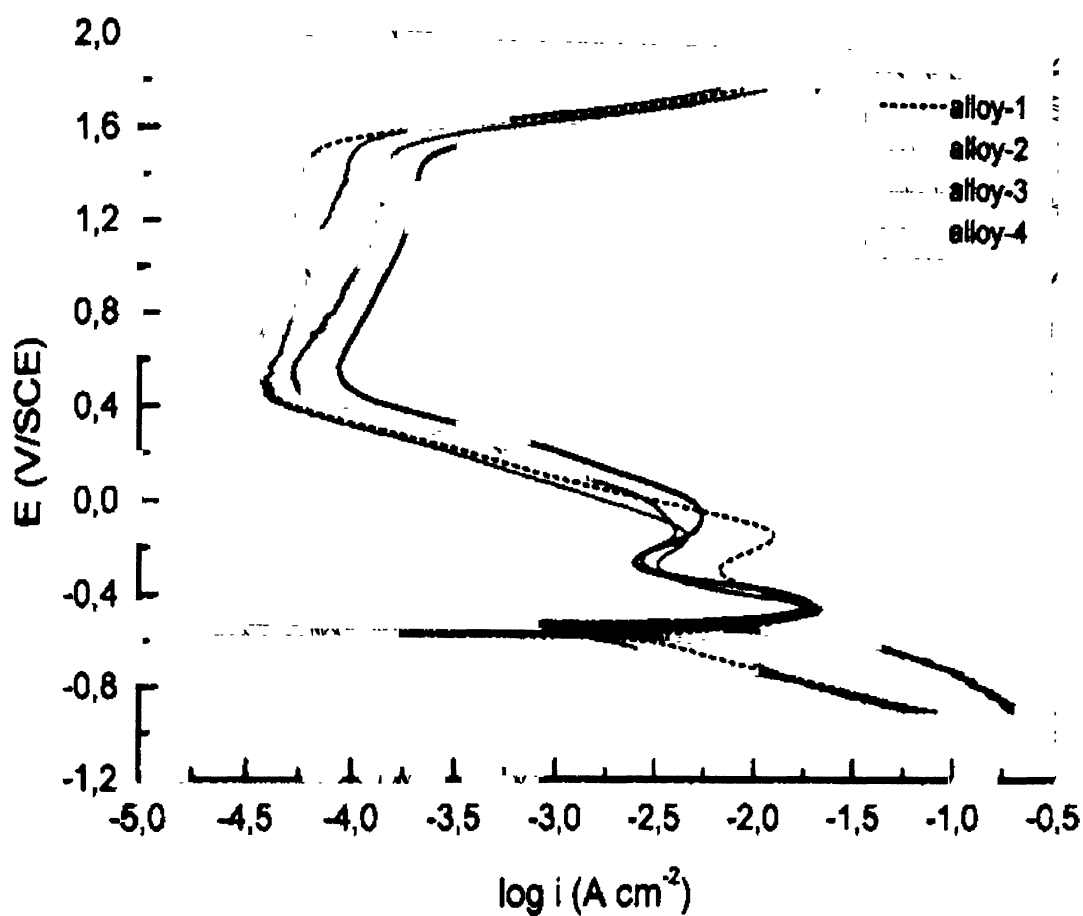
Figure4.24   Potentiodynamic polarization curves of iron aluminide alloys in 0.5 N
          H_2SO_4 showing both the first (active) and the second (nobler) anodic
          peaks [52]
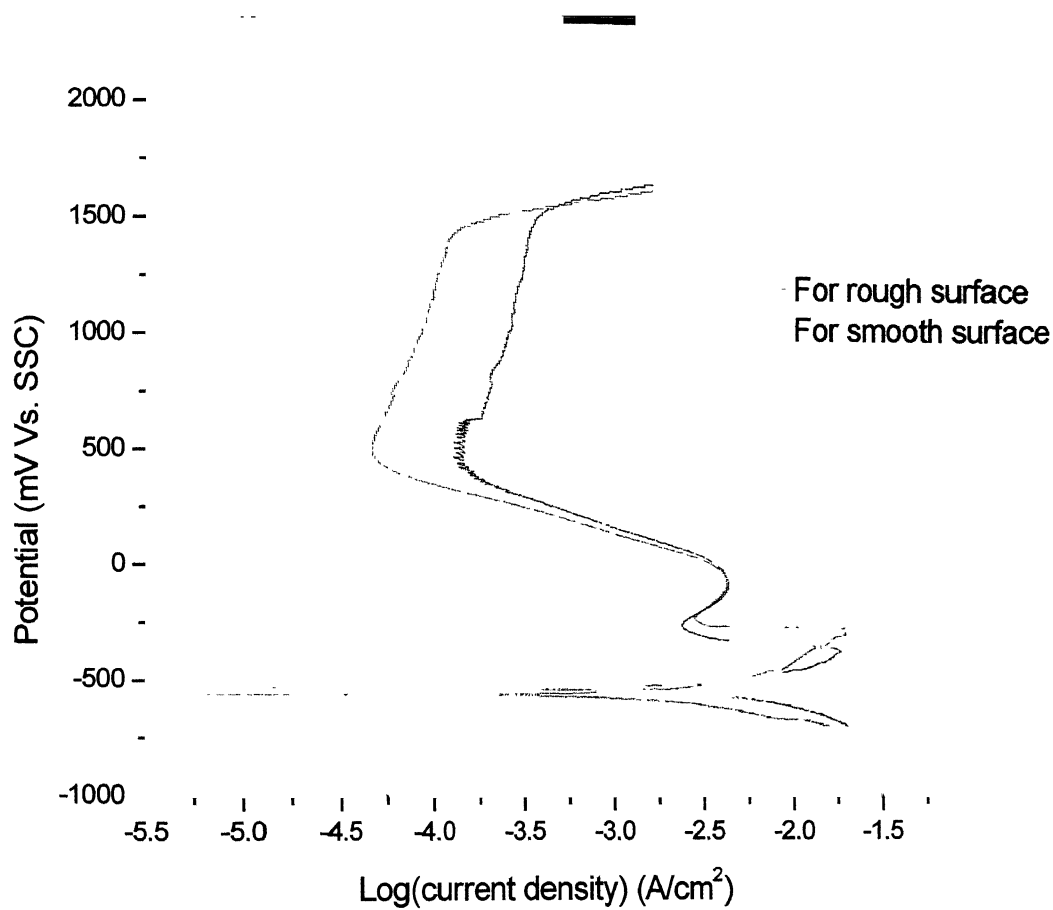
Figure 4.25   Comparison in potentiodynamic polarization behavior between smooth and rough surface of Fe-16.2Al-0.54C (wt%) samples in 0.5 N H_2SO_4 solution

Table 4.14   The β_a, β_c and i_{corr} values obtained from the potentiodynamic polarization in 0.5 N H_2SO_4 for Fe-16.2Al-0.54C alloy of different surface finish

Type of surfaces	β_c (V/decade)	β_a (V/decade)	i_{corr} (mA/cm^2)
Rough	-0.242	295	4.01
smooth	-0.252	288	4.19

Table 4.15   Passivation parameters obtained from the potentiodynamic polarization in 0.5 N H_2SO_4 for Fe-16.2Al-0.54C alloy of different surface finish

$_2SO_4$ N	ZCP	E_{pp1}	E_{pp2}	E_{cp}	E_b	E_b-E_{cp}	i_{crit1}	i_{crit2}	i_{pass}	$i_{0_{H^+/H_2}}$
				mV					mA/cm^2	
ough	-569	-285	-72.3	491	1420	929	19.05	4.17	0.05	3.03×10^{-2}
mooth	-514	-373	-67.6	501	1470	969	18.41	4.23	0.13	2.81×10^{-2}

Table 4.16   Hardness of bulky carbides for Fe-16.2Al-0.54C (wt %) alloy

Treatment Temp (°C)	Time (h)	Diagonal (mm)	SD	FOV	%Error, +-	Hardness kg/mm²
Without treatment		13.230	0.586	30	1.618	529.73
700	10	13.241	0.413	30	1.144	528.85
700	48	13.501	0.389	30	1.101	508.68
900	144	13.629	0.547	30	1.568	499.17
900	144	13.593	0.453	30	1.301	501.81
900	336	13.823	0.631	30	1.721	485.25
900	720	13.937	0.336	30	0.978	474.89

Table 4.17   Hardness of matrix for Fe-16.2Al-0.54C (wt %) alloy

Treatment Temp (°C)	Time (h)	Diagonal (mm)	SD	FOV	%Error, +-	Hardness kg/mm²
Without treatment		17.127	0.556	30	1.185	316.10
700	10	17.231	0.491	30	1.045	312.29
700	48	17.397	0.608	30	1.306	306.36
900	144	17.503	0.544	30	1.396	302.66
900	144	17.487	0.631	30	1.982	303.21
900	336	17.763	0.313	30	0.783	293.86
900	720	17.891	0.365	30	0.820	289.67

Table 4.18   Values of exchange current densities ($i_{0_{H^+/H_2}}$) of different materials for different normalities of H_2SO_4 at 25°C

Electrode	Normality	$i_{0_{H^+/H_2}}$ (mA/cm^2)	Reference
Fe-16.2Al-0.54C (wt %)	0.5	2.95×10^{-2}	Present study
Fe-15.6Al-0.05C (wt %)	0.5	2.5×10^{-2}	52
Fe-15.6Al-0.50C (wt %)	0.5	4.3×10^{-2}	52
Fe-15.6Al-1.00C (wt %)	0.5	50.1×10^{-2}	52
	2.0	1.0×10^{-3}	63
Fe	0.52	2.0×10^{-6}	43
	0.5	2.0×10^{-3}	52
	2	1.0×10^{-7}	63
Al	2	1.0×10^{-9}	43
	0.5	7.9×10^{-7}	52

CHAPTER 5

CONCLUSIONS

Different aspects of high temperature hydrogen attack in carbon-alloyed iron aluminide alloy (Fe-28.1Al-2.1C, in at %) has been addressed in this thesis. The salient conclusions of the present study are presented in the first half of this chapter and the suggested work for future in the later half.

5.1. Conclusions

The following were the salient conclusions of the present study.

1. Microstructural observation indicated that the Fe-28.1Al-2.1C (at %) alloy exhibited a two-phase structure. The matrix contained recrystallized grains. The presence of carbide precipitates was also evident. The carbides were distributed uniformly throughout the matrix of iron aluminide. Two different types of morphology of the carbides were observed. The first type appeared as circular on the two-dimensional micrograph and the other as needle-shaped.

2. Stereological analyses were carried out on the rolling plane of the alloy. It has been demonstrated that statistical reliable and robust quantitative microstructural data can be obtained by performing very simple manual measurements. The needle-shaped carbides contribute to a large exploded surface area per unit volume in spite of having a very low volume fraction. Contiguity data suggest that the bulky carbides avoid sharing surface with each other. It may be also similarly concluded for needle shaped carbide. The edge length between bulky carbides and matrix is approximately two times more than that between three grains of matrix or between needle-shaped carbides and matrix. Therefore, it is predicted that hydrogen (and carbon) would diffuse much more easily through the interfaces between the bulky carbides and matrix. Moreover, the bulky carbide is 3.5 times more likely to occur on a grain triple point and two times more likely to occur between two grains as compared to inside a

grain. This must be related to the sympathetic nucleation of the carbides at heterogeneities and also to the easy diffusion of carbon through grain boundaries, during the formation of these carbides.

3. The composition of the bulky carbides and needle-shaped carbides were determined by EPMA. The compositions approximates to 64.17Fe-19.81Al-18.35C and 62.40Fe-19.87Al-17.73C, respectively. The stoichiometric formula of the matrix phase and bulky carbide was determined as Fe_3Al and $Fe_{4-y}Al_yC_x$, where y varies from 0.91 to 1.19 and x varies from 0.90 to 1.02. Similarly the formula of the needle-shaped carbides was estimated as $Fe_{4-y}Al_yC_x$, where y varies from 0.99 to 1.12 and x varies from 0.82 to 0.96.

4. The thermodynamic feasibility of methane formation in Fe-16.2Al-0.54C was theoretically proved at 700°C and at 900°C. Moreover, the kinetics of hydrogen diffusion into the material was evaluated theoretically to obtain insights into the anticipated depth of attack. It is observed that the methane fugacities decrease rapidly with increasing distance into the material. Maximum hydrogen attack is therefore anticipated in the region near the surface.

5. The microstructures were studied after high temperature treatments (i.e. at 700°C for 10h and 48 h, and at 900°C for 144h, 336h and 720 h). The optical characterization justified that the interface between blocky carbides and grains were mainly affected. The carbides are also effected. The degree of attack increased as the kinetic parameters i.e. temperature and the time period were increased. The SEM study of the hydrogen treated samples also validates the optical observations. Interestingly, the planes along which hydrogen attack proceeded in the carbides are {111} and {110}. As in the Fe_3AlC structure, the {111} and {110} planes contain both carbon and aluminum atom, the attack may have been preferred on these planes as both carbon (reacting with hydrogen) and aluminium (reacting with oxygen) are removed during the high temperature hydrogen treatment. However, at the higher temperature the attack of the bulky carbides was not evident for longer time (336 hours and 720

hours) as to the surface coverage of oxide formed at higher temperature for longer time hindered the hydrogen diffusion, thereby, restricting the formation of methane.

6. Electrochemical polarization studies indicated that the as-received alloy as well as the hydrogen treated samples exhibited active-passive behavior in acidic solution (0.1 N to 1.0 N H_2SO_4). Notably, the anodic polarization curves of the alloy exhibited a secondary anodic peak in the range of –45 mV to –92 mV, with respect to Ag-AgCl standard electrode, before reaching the broad passive zone of constant passive current density. The corrosion rate (i_{corr}) increased continuously and systematically (from 0.41 $mAcm^{-2}$ for 0.1 N to 6.31 $mAcm^{-2}$ for 1.0 N) as the normality of the H_2SO_4 was increased from 0.1 N to 1.0 N. The critical current density for the second anodic peak did not display a general trend of increase with increase in normality of H_2SO_4. Whereas, the increasing critical current density for the second anodic peak can be understood by the larger amount of hydrogen available for oxidation in solutions of lower pH. In the passive region, the passive current density was constant in solutions of different normalities, thereby proving the similar nature of the passive film on the surface of the alloy as a function of potential.

7. Evolution of hydrogen on the surface of the hydrogen treated samples increased with increase in treatment temperature and time, thereby, the secondary anodic peak also showed an increase with increase in treatment temperature and time. The hydrogen dissolved during the treatment did not play any role on the secondary anodic peak. The increase in the passivation ranges and i_{pass} values of hydrogen treated samples with increasing treatment temperature and time could not be attributed to the surface roughness induced by the high temperature hydrogen treatment. The change in surface property was confirmed by the change in hardness of the carbides and matrix. The decrease in hardness of the matrix could probably be due to the decurburization from matrix. The carbon could have either diffused to the bulky carbide precipitates or reacted with the ambient environment. The lower matrix hardness also indicates compositional changes.

5.2. Suggestions for future work

Some of the additional work, which are needed to be undertaken in order to resolve some of the issue raised in this thesis, are:

1. Stereological analysis, optical and SEM characterization should also be done for the short and long traverse sections of the as-received Fe-28.1Al-2.1C alloy as well as of the hydrogen treated samples. This would help to understand the effect of processing heat treatment of the alloy.

2. The effect of hydrogen treatment should be studied for iron aluminide alloys other than the Fe-28.1Al-2.1C alloy to better understand the phenomenon. Iron aluminides containing lower amount of aluminum should be studied, as complete alumina coverage will not be there on the surface of the alloy.

3. The hydrogen attack can be better understood by conducting the hydrogen treatment at different temperatures for different time of exposure, preferably at different hydrogen pressure.

4. The electrochemical polarization behavior of the alloy can be using different electrolyte other than H_2SO_4, for example borate buffered solution of pH 7.6 for better understanding of passivity of the alloy.

BIBLIOGRAPHY

1. N.S. stoloff, "Ordered alloys – physical metallurgy and structural applications", *International Metal Review*, v. 29, 1984, pp 123-135.

2. C.T. Liu, J.O. Stiegler and F.H. Froes, "Ordered Intermetallics", *Metal Handbook 10th ed., ASM, Materials Park, USA,* v. 2, 1990, pp. 913-942.

3. C.T. Liu and K.S. Kumar, "Ordered Intermetallic alloys, Part 1, nickel and Iron aluminides", *J. Metals*, v. 45, 1993, pp. 38-44

4. W.R. Kerr, Met. Trans., v. A17, 1986, pp. 2298-2300

5. R.G. Baligidad, U. Prakash and A. Radhakrishna, *Mater. Sci. Engg. A*, v. 249, 1998, pp. 97-102

6. R.G. Baligidad, U. Prakash, V.R. Rao and P.K. Rao, ISIJ International, v. 36, n. 12, 1996, pp. 1453-1458.

7. R.G. Baligidad, U. Prakash and A. Radhakrishna, *Mater. Sci. Engg. A*, v. 230, 1996, pp. 188-193

8. M. Sen, R. Balasubramaniam and A.V. Ramesh Kumar, Bull. Mater. Sci., v. 23, n. 5, 2000, pp. 399-403

9. R.G. Baligidad, U. Prakash and A. Radhakrishna, *Mater. Sci. Engg. A*, v. 265, 1999, pp. 301-305

10. M. Palm and G. Inden, *Intermetallics*, v. 3, n. 6, 1995, pp. 443-454

11. V. Raghavan, Phase diagram of ternary iron alloys, Part 1, Indian Institute of Metals, 1991, pp. 89-97

12. L.F. Mondolfo and B. Wurths, Aluminium alloys: Structure and properties, pp. 237-287

13. C. Sykes and J. Bampyfylde, *J. Iron Steel Inst.*, n. 130, 1932, pp. 389-394

14. C.T. Liu, C.G. McKamey and E. H. Lee, *Scripta Metall. Mater.,* 24, 1990, pp. 385-390

15. Y.F. Zhu, C.T. Liu and C.H. Chen, *Scripta Mater.*, 35, 1996, pp. 1435-1439

16. T.J. Carter and L.A. Cornish, *Engineering Failure Analysis*, 2001, v. 8, pp. 113-121

17. R. Gibala and A.J. Kumnick, "Hydrogen Trapping in Iron and Steels", Hydrogen Embrittlement and Stress Corrosion Cracking, ed. by R Gibala and R.F. Hehemann, ASM, Ohio, 1984, pp. 61-76

18. J. Woodtli and R. Kieselbach, *Engg. Fail. Analysis*, 2000, v. 7, n. 6, pp. 427-450

19. P. Banerjee, "Hydrogen behavior in Chromium and Titanium Alloyed iron aluminides", M. Tech. Thesis, I.I.T., Kanpur, 1997

20. P. Banerjee and R. Balasubramaniam, *Bull. Mater. Sci.,* 20, 1997, pp. 713-717,

21. J. Volkl and G. Alefeld, *Topics in Applied Physics*, 28, 1978, pp. 321-344

22. J. Volkl and G. Alefeld, "Diffusion in Solids", ed. by A.S. Nowick and J.J. Burton, Academic Press, New York, USA, 1975, p. 231

23. K. Kiuchi and R.B. McLellan, "The solubility and diffusivity of hydrogen in well-annealed and deformed iron", *Acta Metall.,* 31, 1938, pp. 961-984

24. H. Chiu, L. Qiao and X. Mao, "Environmental assisted cracking of iron aluminide in 3.5% NaCl solution", *Scripta Mater.*, 34, 1996, pp. 963-969

25. D.A. Jones, "Principles and prevention of corrosion", Maxell Macmillan International editions, 1992.

26. R. Balasubramaniam, *Bull. Mater. Sci.,* 22, 1999, pp.571-579

27. R.G. Baligidad, U. Prakash, A. Radhakrishna and V. Ramakrishna Rao, *Scripta Mater.,* 36, 1997, pp. 667-671

28. R.G. Baligidad and A. Radhakrishna, *Mater. Sci. Engg. A*, v. 281, 1999, pp. 97-102

29. P.F. Timmins, Solutions to Hydrogen Attack on Steels, ASM Internationals, 1997

30. D.A. Westphal and F.J. Worzala, "Hydrogen Attack on Steel", Hydrogen in Metals, ed. by I.M. Bernstein and W. Thompson, American Society of Metals, 1973, v. 2, pp. 79-89

31. D. Eliezer, "High Temperature Hydrogen attack Studies", Hydrogen Effects in Metals, ed. by I.M. Bernstein and W. Thompson, The Metallurgical society of AIME, 1980, pp. 913-921

32. A.S. Tetelman, "Recent Development in Classical (Internal) Hydrogen Embrittlement", Hydrogen in Metals, ed. by I.M. Bernstein and W. Thompson, American Society of Metals, 1973, v. 2, pp. 17-34

33. M.R. Louthan, Jr., "Effect of Hydrogen on The Mechanical Properties of Low Carbon and Austenitic steel", Hydrogen in Metals, ed. by I.M. Bernstein and W. Thompson, American Society of Metals, 1973, v. 2,

34. A. Nelson, Hydrogenation Plant Steel Proceeding, American Petro. Inst., 1949, v. 29M, pp. 163-174

35. T. Sakai and H. Kaji, "Effect of Impurity Elements on The Formation of Bubbles by Hydrogen Attack in 2.25Cr-1Mo Steel", Hydrogen Effects in Metals, ed. by I.M. Bernstein and W. Thompson, The Metallurgical society of AIME, 1980, pp. 903-911

36. M. Ransick and P. Shewmon, "The Roll of Gas Venting in Hydrogen Attack of Steel", Hydrogen Effects in Metals, ed. by I.M. Bernstein and W. Thompson, The Metallurgical society of AIME, 1980, pp. 895-902

37. E.R. Weibel, Stereological Methods, v. 2, Academic Press, 1980, pp. 1-18

38. E.E. Underwood, Quantitative Stereology, Addition-Wesley Publishing Company, 1970, p. 25-103

39. H. Fischmeister, Computers in Material Technology, edited by T. Ericsson, Pergamon Press, 1980, pp. 109-129

40. J.E. Hilliard, Quantitative Microscopy, Edited by R.T. Dehoff and Fredrick N. Rhines, McGraw-Hill Book Company, 1968, pp. 45-289

41. P. Ciavarella, H. Moueddeb, S. Miachon, K. Fiaty and J.A. Dalmon, Catalysis Today, v. 56, n. 1-3, 2000, pp. 253-264

42. K. R. Trethwey and J. Chamberlin, Corrosion For Students of Science and Engineering, John Wiley & Sons, Inc., New York, 1988

43. D.A. Jones, Principles and Prevention of Corrosion, Maxwell Macmillan International Editions, NY, 1992

44. S.J. Suess, " Corrosion in Stainless Steel," Advanced Materials Processes, 1997, v.151, n.4, pp. 27-30

45. M.G. Fontana and N.D. Greene, Corrosion Engineering, McGraw-Hill International Book Company, Japan, 2nd edition, 1983

46. W.S. Tait, "An Introduction to Electrochemical Corrosion Testing For Practicing Engineers and Scientists," Pair O Does Publications, Racine, WI, USA, 1994

47. Metals Test Methods and Analytical Procedures, Annual Book of ASTM Standards, v. 3.02, section 3, Philadelphia, PA, USA, 1987

48. M. Sen, Environmental degradation of carbon-alloyed Fe_3Al-based intermetallics, M. Tech. Thesis, 2000, p. 34

49. D. Das, High temperature oxidation and hot corrosion behavior of carbon-alloyed Fe_3Al-based intermetallic alloys, M. Tech. thesis, 2001, p.

50. R.G. Baligidad, U. Prakash and A. Radhakrishna, *Mater. Sci. Engg. A*, v. 255, 1998, p. 162

51. R.G. Baligidad, U. Prakash and A. Radhakrishna, *Mater. Sci. Engg. A*, v. 257, 1998, pp. 235-239

52. V.S. Rao, R.G. Baligidad and V.S. Raja, *Corrosion Sci.*, v. 44, 2002, pp. 521-523

53. S. Frangini, N.B. De Cristofaro, A. Mignose, Corrosion science, v. 39, 1997, pp 1431-1442

54. A.A. Hermas, M.S. Morad, K. Ogura, Corrosoin sci., V. 41, 1999, pp2251-2266

55. W.B. Pearson, "Handbook of lattice spacing and structures of metals"

56. F. Gehrmann, H.J. Grabke, E. Riecke, The effects of the nitrides and carbides of V, Nb and Ti on the diffusion and dissolution of hydrogen in iron, Hydrogen transport and cracking in metals, Institute of Materials Proceedings, A. Turnbull (Ed.), London, 1995, pp. 216-226

57. M. Smialowski, Hydrogen in steel, Addison-Wesley Publishing Company, Inc., Pergamon Press, 1962, pp. 25-130

58. D.R. Gaskell, Introduction to Metallurgical Thermodynamics, Taylor & Francis, 2nd Ed., 1981

59. D.R. Gaskell, Introduction to Metallurgical Thermodynamics, Taylor & Francis, 3nd Ed., 1995

60. T.V. Rajan, C.P. Sharma and A. Sharma, Heat Treatment: Principles and Techniques, Eastern Economy Edition, 1996, pp. 120-152

61. V. Raghavan, Phase diagram of ternary iron alloys, Part 3, Indian Institute of Metals, year, pp. 80

62. S.H. Avner, Introduction to Physical Metallurgy, McGraw-Hill Int. Ed., 2nd Ed., pp. 130-145

63. S.A. Bradford, Corrosion Control, Van Nostrand Reinhold, New York, pp. 6-44

64. S.M. Schlogl and E.V.D. Giessen, Computational model for carbon diffusion and methane formation in a ferritic steel during hydrogen attack, *Scripta Materialia*, n. 46, 2002, pp. 431-436

65. V. Raghavan, Material Science and Engineering, 3rd Ed., Prentice Hall of Pvt. Ltd., 1996, pp. 170-190